

UNIVERSITY OF OKLAHOMA
GRADUATE COLLEGE

MESOVORTEX-INDUCED TORNADOES: A CASE STUDY OF THE 13 APRIL 2018
NORTHWEST LOUISIANA QUASI-LINEAR CONVECTIVE SYSTEM

A THESIS
SUBMITTED TO THE GRADUATE FACULTY
in partial fulfillment of the requirements for the
Degree of
MASTER OF SCIENCE IN METEOROLOGY

By
ALEC J. PROSSER
Norman, Oklahoma
2022

MESOVORTEX-INDUCED TORNADOES: A CASE STUDY OF THE 13 APRIL 2018
NORTHWEST LOUISIANA QUASI-LINEAR CONVECTIVE SYSTEM

A THESIS APPROVED FOR THE
SCHOOL OF METEOROLOGY

BY THE COMMITTEE CONSISTING OF

Dr. Michael I. Biggerstaff, Chair

Dr. Cameron Homeyer

Dr. Erik Rasmussen

Dedication

This thesis is dedicated to my mother, sister, and late father, who always inspired me to be curious about the world from a very young age, encouraged me to pursue my ambitions in atmospheric sciences, and always had my back when I faced challenges associated with my chosen path.

Acknowledgments

First and foremost, I would like to offer extensive thanks to my family for all of the encouragement, guidance, and late-night phone calls during my time pursuing this degree. I honestly wouldn't have been able to do this without their support, and I am forever grateful for them. I also have to extend a massive "thank you" to all the friends and members of my research group who have had a part in shaping my graduate student experience thus far. To all of you: I am endlessly grateful for the shared jokes, DnD weekends, the Flapjack Fridays, and the huge amount of support you all are to me. You have all made my time in Oklahoma thoroughly enjoyable and I can't thank you enough. I would be remiss if I didn't extend considerable thanks to my advisor, Mike Biggerstaff, for all of his assistance with developing me as a researcher and for mentoring me through this process; and to Addison Alford for his extensive help with all things Python and/or research, he went above and beyond to assist me in my endeavors and I am extremely grateful to consider him a colleague and friend. Last but certainly not least, I want to thank my girlfriend Laura for her tireless support of me. Laura: thank you for all of the heart-to-heart conversations, your technical edits and suggestions, and for being my rock through this process. You are amazing and I'm endlessly thankful for you. Finally, thank you to NOAA for providing the funding necessary to accomplish this work through Grant NA18OAR4590315.

Table of Contents

Dedication	iv
Acknowledgments	v
List Of Tables	viii
List Of Figures	ix
Abstract	xv
1 Introduction	1
2 Background and Motivation	4
2.1 Quasi-Linear Convective System Background	4
2.2 QLCS Features	7
2.2.1 The Sustaining Role of Wind Shear and the Rear Inflow Jet	7
2.2.2 Mesovortex Formation Mechanisms	9
2.3 Synoptic and Event Background	14
3 Methods	24
3.1 Doppler Radar Configurations	24
3.2 Radar System Description	26
3.2.1 KSHV WSR-88D	26
3.2.2 SMART-Radars	27
3.3 Analysis Methods	29
3.3.1 Radar Data Collection and Processing	29
3.3.2 Dual-Doppler Analysis Technique, Calculations, & Visualization	31
4 Single Doppler Analyses	36
4.1 Mesovortex #1	36
4.2 Mesovortex #2	52
5 Results: Dual Doppler Analyses	70
5.1 Mesovortex #1	70
5.1.1 Data Analysis Limitations	70
5.1.2 Vorticity Evolution Prior to Tornadogenesis	71
5.1.3 Tilting and Stretching Before Tornadogenesis	75

5.1.4	Vorticity Evolution Post-Tornadogenesis	83
5.2	Mesovortex #2	102
5.2.1	Pre-Tornadic Stage	102
5.2.2	Tornadogenesis Stage	113
5.2.3	Tornadic Stage	116
5.2.4	Dissipating Stage	125
6	Conclusions & Future Work	135
	Reference List	140

List Of Tables

3.1	Radar scanning strategies utilized during data collection; PRF: Pulse Repetition Frequency.	29
3.2	A summary of the interpolated Cartesian grids utilized in this case study. X,Y,Z values are relative to dual-Doppler grid center point: KSHV for Mesovortex #1, SMART-R1 for Mesovortex #2.	31
3.3	Measured storm velocities for each mesovortex.	33

List Of Figures

1.1	The percentage of all thunderstorm hazards in 80km x 80km grid cells produced by QLCSs; (a) all severe events, (b) tornadoes, (c) non-tornadic severe winds, (d) severe hail. Adapted from Ashley et al. (2019)	3
2.1	A schematic diagram of a tropical squall line, as presented in <i>Fig. 1</i> of Gamache and Houze (1982).	5
2.2	Conceptual model of a squall line with a trailing stratiform area viewed in a vertical cross section oriented perpendicular to the convective line (i.e., parallel to its motion). Adapted from Houze et al. (1989).	6
2.3	Synoptic-scale analyses at 1200 UTC on 13 April, at the (a) surface, (b) 850 mb, (c) 500 mb, and (d) 300 mb levels. Images taken from the Storm Prediction Center (2018).	16
2.4	As in <i>Figure 2.3</i> , but for 0000 UTC on 14 April.	17
2.5	Skew-T of the environment in NW Louisiana at 0015 UTC on 14 April 2018.	18
2.6	As in <i>Figure 2.5</i> , but for 0503 UTC.	19
2.7	Radar reflectivity composite of convection that would eventually become the QLCS as it initiated in North Texas.	21
2.8	As in <i>Figure 2.7</i> , but for 0522 UTC, and using data from KSHV, SMART-R1, and SMART-R2.	22
2.9	As in <i>Figure 2.7</i> , but for the decaying period of the QLCS, and using data from KPOE and KDGX.	23
3.1	The dual-Doppler domain produced by SMART-R1 and SMART-R2; note that SMART-R2 and CPOLRVP are synonymous.	25
3.2	The dual-Doppler domain produced by SMART-R1 and KSHV.	26
4.1	The squall line as it developed a bow-echo reflectivity pattern in Texas at the listed times, as observed by KSHV at the 0.5 deg tilt. The red box indicated the bow of interest, where mesovortices would become apparent over the next couple of hours.	37
4.2	KSHV radar reflectivity (a) and radial velocity (b) at 0345 UTC. Note the strong flow (white oval) precipitating the bow-echo in the convective line (black oval).	38
4.3	KSHV radar reflectivity (a) and (c), and radial velocity (b) and (d) at 0408 UTC. Note the vertical depth of the first and second mesovortices associated with the QLCS bowing segment. Images (a) and (b) are of the 0.8 deg tilt, and (c) and (d) are of the 2.4 deg tilt. The vortex associated with the Shreveport-Bossier City tornado is circled in black.	39

4.4	KSHV 0.5 deg radar reflectivity (a) and radial velocity (b) at 0420 UTC depicting the intense inbound velocities associated with the QLCS's RIJ. The periphery of the jet is highlighted in white for clarity.	40
4.5	The intensifying mesovortex as viewed from KSHV at the 0.5 deg elevation angle PPI sweep between 0443 and 0447 UTC. Images (a) and (b) depict radar reflectivity and radial velocity, respectively, at 0443 UTC. Images (c) and (d) depict radar reflectivity and radial velocity, respectively at 0446 UTC. Note the increase in inbound velocities on the south side of the vortex between images (c) and (d).	42
4.6	Evolution of SMART-R1 radar reflectivity from 0447 (top row) to 0449 UTC (bottom row). The black circle represents the location of the mesovortex.	43
4.7	The appearance of the RIJ at various heights as viewed by KSHV between 0456 and 0459 UTC. The mesovortex location is circled in white. (a) The circulation at about 450 m altitude; (b) same as in (a) but for 580 m; in (c) same as in (a) but for 900 m; and (d) same as (a) but for 1.7 km. Note the reduction of the RIJ strength with altitude, and the continuing presence of the vortex.	44
4.8	A cross-section of the KSHV radial velocity taken perpendicular to the convective line at 0507 UTC as the circulation moved into the cone of silence region. Note the presence of the intense RIJ (circled in cyan) and its proximity to the mesovortex (given by the white arrow).	45
4.9	Mesovortex region 0.8deg radar reflectivity and radial velocity, as viewed by KSHV at 0508 UTC. The echo appendage and rotation signature in the velocity field is highlighted with white circles.	46
4.10	The mesovortex region (white circles) as the tornadic circulation emerged from the KSHV cone of silence at 0517 UTC. The height of the vortex is 50 m in (a), 300 m in (b), and 2.2 km in (c).	47
4.11	A cross-section of radial velocity taken perpendicular to the convective complex at 0517 UTC, as viewed from KSHV. The mesovortex is highlighted by the black arrow. Note the prevalent $30 m s^{-1}$ velocity returns associated with the RIJ.	48
4.12	Radar reflectivity (a) and radial velocity (b) in the 0.5deg elevation sweep from KSHV at 0541 UTC. The A to A' line is the approximate location of the cross section of radial velocity depicted in (c). In (c) the location of the vortex is highlighted by the white arrow, and the RIJ is circled in cyan. Note the weaker appearance of the mesovortex, and the separation of the RIJ and vortex.	50
4.13	Radial velocity from SMART-R1 showing the weakening of both the rear inflow and mesovortex at (a) 0537 UTC, and (b) 0540 UTC by SMART-R1. The vortex of interest is circled in black.	51
4.14	KSHV 0.5 deg radar reflectivity (a) and radial velocity (b) at 0555 UTC.	51

4.15	Radial velocity from the 1.3 deg elevation angle sweep from SMART-R1 at (a) 0444 UTC, (b) 0452 UTC, (c) 0456 UTC, and (d) 0502 UTC. The rear inflow is circled in white and the mesovortex region is circled in black. . . .	53
4.16	(a) Radar reflectivity and (b) radial velocity at 0504 UTC from the 0.5 deg elevation sweep from SR1. Circled areas denote cyclonic shear regions that formed along the line downwind of the RIJ axis. Note that the northern circle encompasses two shear features.	54
4.17	Radial velocity at (a) 3.1 deg, (b) 4.1 deg, (c) 6.6 deg, and (d) 8.0 deg elevation angles from the 0504 UTC SMART-R1 volume scan. The mesoscale and convective-scale regions of important rear-inflow are enclosed by the black outline.	55
4.18	(a) Radar reflectivity and (b) radial velocity at 0.5 deg elevation from the 0501 volume taken by SMART-R1. (c) Radar reflectivity and (d) radial velocity at 0.5 deg elevation from the 0509 UTC volume scan taken by SMART-R1. Note the increase in radar reflectivity in the enclosed black curve just west of the cyclonic shear zones enclosed in the red circle.	57
4.19	(a) Radar reflectivity and (b) radial velocity from the 0.8 deg elevation sweep taken with SMART-R1 at 0515 UTC. (c) Radar reflectivity and (d) radial velocity from the 4.6 deg elevation sweep taken with SMART-R1 at 0515 UTC. The black lines in (a) and (c) denote the gust front location along the bowed line segment. The black circles in (b) and (d) denote the location of mesovortex #2.	58
4.20	The environmental inflow notch feature at 0515 UTC, as observed by SMART-R1 at the 0.8 deg elevation.	59
4.21	(a) Radar reflectivity and (b) radial velocity from the 10.3 deg elevation angle sweep taken by SMART-R1 at 0518 UTC. (c) Radar reflectivity and (d) radial velocity from the 5.8 deg elevation sweep taken by SMART-R1 at 0525 UTC. Regions of the mesovortex are circled in (a) and (c), while (b) and (d) have the RIJ of interest highlighted by the black outline.	60
4.22	Radial velocity from the 0532 UTC volume scan taken by SMART-R1 at (a) 0.5, (b) 1.3, (c) 3.1, and (d) 6.6 deg elevations. The black circle denotes the mesovortex while the gray outline denotes the RIJ feature of interest.	62
4.23	(a) Radar reflectivity and (b) radial velocity from SMART-R1 taken at 0.5 deg elevation from the 0540 UTC volume scan. (c) Radar reflectivity and (d) radial velocity from SMART-R1 taken at 0.9 deg in elevation from the 0540 UTC volume scan.	64
4.24	Radial velocity from the 0540 UTC volume scan taken with SMART-R1 at (a) 1.8 deg, (b) 2.3 deg, (c) 3.1 deg, and (d) 4.1 deg.	65
4.25	Radial velocity from the 0542 UTC volume scan taken with SMART-R1 at (a) 0.9 deg, (b) 1.8 deg, (c) 3.1 deg, and (d) 5.2 deg in elevation.	66

4.26	(a) Radar reflectivity and (b) radial velocity from the 0545 UTC volume scan at the 1.8 deg elevation taken with SMART-R1. (c) Radar reflectivity and (d) radial velocity from the 0545 UTC volume scan at the 3.1 deg elevation taken with SMART-R1.	67
4.27	Radial velocity from SMART-R1 taken from the 0547 UTC volume scan at elevations of (a) 0.5 and (b) 0.9 deg.	68
4.28	(a) Radar reflectivity and (b) radial velocity from the 0557 UTC SMART-R1 volume scan at 0.5 deg elevation.	69
5.1	The mesovortex region at 0456 UTC from 250 m to 1 km AGL. Vorticity is filled in color, and vertical motion is contoured every $2.5 m s^{-1}$ in black (positive values use solid contours; negative values use dashed contours).	72
5.2	As in <i>Figure 5.1</i> , but for 0504 UTC.	73
5.3	As in <i>Figure 5.2</i> , but for heights between 1.25 and 2 km.	74
5.4	The total tilting term magnitude (in color), storm-relative winds (black arrows), and the horizontal vorticity vector (ω_H ; gray arrows) in the mesovortex region at 0456 UTC. The domain of this figure matches that of <i>Figure 5.1</i>	77
5.5	As in <i>Figure 5.4</i> , but for the stretching term magnitude.	78
5.6	As in <i>Figure 5.5</i> , but for stretching at 0504 UTC.	79
5.7	The magnitude of the crosswise component of the tilting term at 0456 UTC. Tilting magnitude filled in color, vertical motion is contoured in black every $2.5 m s^{-1}$ (solid contours represent upward motion, dashed contours represent downward motion), horizontal vorticity vectors are in gray, and storm-relative wind vectors are in black.	80
5.8	As in <i>Figure 5.7</i> , but for 0504 UTC.	81
5.9	As in <i>Figure 5.1</i> , but for 0517 UTC as the vortex emerges from the baseline of the dual-Doppler domain.	84
5.10	As in <i>Figure 5.9</i> , but for the 1.25 to 2 km layer.	85
5.11	As in <i>Figure 5.4</i> , but for 0517 UTC.	86
5.12	As in <i>Figure 5.8</i> , but for 0517 UTC, analyzed just after tornadogenesis.	87
5.13	As in <i>Figure 5.12</i> , but for streamwise vorticity tilting term magnitude.	88
5.14	The stretching of vorticity term magnitude (color fill) and vorticity contours (positive values are solid; negative values are dashed) at 0517 UTC between 250 m and 1 km AGL.	90
5.15	The vorticity field (color fill) and vertical motion (black contours with up-draft denoted by solid lines, and downdrafts indicated by dashed lines) at 0524 UTC, between 250 m and 1 km.	91
5.16	As in <i>Figure 5.14</i> , but for 0524 UTC.	92
5.17	As in <i>Figure 5.11</i> , but for 0524 UTC.	93
5.18	As in <i>Figure 5.13</i> , but for 0524 UTC.	95
5.19	As in <i>Figure 5.15</i> , but for 0531 UTC.	96
5.20	As in <i>Figure 5.19</i> , but for 0537 UTC.	97

5.21	As in <i>Figure 5.17</i> , but for 0537 UTC, when the mesovortex was in its weakening stages.	99
5.22	As in <i>Figure 5.20</i> , but for the decaying period of the vortex at 0544 UTC.	100
5.23	Vorticity (color fill) and black vertical motion contours every 2.5 m s^{-1} (solid contours represent updrafts; dashed contours represent downdrafts) in the vortex region at 0536 UTC. Heights in this layer range from 250 m to 1 km AGL.	103
5.24	As in <i>Figure 5.23</i> , but for 1.25 to 2 km layer.	104
5.25	As in <i>Figure 5.23</i> , but for 0538 UTC.	106
5.26	As in <i>Figure 5.25</i> , but for the 1.25 to 2 km layer.	107
5.27	The 250 m to 1 km altitude 0538 UTC total vorticity tilting term magnitude (color fill) with storm-relative wind vectors (black arrows), and horizontal vorticity (ω_H) vectors (gray arrows) overlaid.	108
5.28	The 250 m to 1 km altitude streamwise vorticity tilting component (color fill) with vertical velocity contours in black (solid contours represent upward motion; dashed contours represent downward motion), storm-relative wind vectors (black arrows), and horizontal vorticity (ω_H) vectors (gray arrows) overlaid.	109
5.29	Mesovortex region reflectivity (a, b), convergence (color fill) and vertical vorticity (line contours) (c, d), change in zonal wind between 0538 and 0541 UTC (e), and change in meridional wind between 0538 and 0541 UTC (f) at 500 m. In (c) and (d), red colors indicate convergence magnitude and blue colors indicate divergence magnitude.	111
5.30	As in <i>Figure 5.25</i> , but for 0541 UTC.	114
5.31	As in <i>Figure 5.26</i> , but for 0541 UTC.	115
5.32	As in 5.27, but for 0541 UTC.	117
5.33	As in <i>Figure 5.16</i> , but for the second mesovortex at 0541 UTC.	118
5.34	As in <i>Figure 5.28</i> , except for the crosswise vorticity component at 0541 UTC.	119
5.35	As in <i>Figure 5.30</i> , but for 0543 UTC.	120
5.36	As in <i>Figure 5.35</i> , but for 0546 UTC.	121
5.37	The stretching of vorticity term magnitude (color fill) and vorticity contours (in black) at 0543 UTC between 250 m and 1 km AGL. The green triangle indicates the approximate location of the tornado at analysis time.	123
5.38	The 250 m to 1 km altitude 0543 UTC total vorticity tilting term magnitude (color fill) with storm-relative wind vectors (black arrows), and horizontal vorticity (ω_H) vectors (gray arrows) overlaid. The approximate location of the tornado at 0543 UTC is given by the green triangle.	124
5.39	As in <i>Figure 5.34</i> , but for 0543 UTC.	126
5.40	As in <i>Figure 5.39</i> , but for the streamwise component of vorticity tilting.	127
5.41	As in <i>Figure 5.37</i> , but for 0546 UTC.	128
5.42	As in <i>Figure 5.38</i> , but for 0546 UTC.	129
5.43	As in <i>Figure 5.36</i> , but for 0548 UTC.	130
5.44	As in <i>Figure 5.41</i> , but for 0548 UTC.	131

5.45	As in <i>Figure 5.42</i> , but for 0548 UTC.	132
5.46	As in <i>Figure 5.43</i> , but for 0551 UTC.	134

Abstract

Mesoscale- γ circulations occurring along the leading edge of Quasi-Linear Convective Systems (QLCS), and their propensity to produce tornadoes and straight-line wind damage has long been noted in literature. Furthermore, this association and the discovery of related features has been reinforced by recent numerical modeling studies of QLCS tornadoes. However, observational data sets of processes sustaining these vortices, genesis mechanisms, specific details of their evolution, and observational confirmation of these modeled features has been elusive.

Just after midnight on 14 April 2018, a tornadic QLCS moved across northwest Louisiana, producing numerous reports of tornadoes. One notable mesovortex-associated tornado caused EF-1 damage along its 22.5 mile path in Shreveport and Bossier City, LA. A second QLCS mesovortex would later produce a brief EF-0 tornado near Sarepta, LA. Both University of Oklahoma C-band, Shared Mobile Atmospheric Research and Teaching Radars (OU SMART-R) were operating in the area at the time the tornadoes occurred as part of the ongoing VORTEX-SE field campaign, allowing for the unique opportunity to investigate QLCS mesovortex intensification and tornadogenesis processes. The resulting datasets from SMART-R1 and SMART-R2 allowed for the construction of an observational domain with dual-Doppler coverage having 2-3 minute temporal resolution.

Analysis of the dual-Doppler dataset allows for a detailed interrogation of vertical structure and mesovortex processes, particularly at low-levels within the storm. Results from these analyses suggest that tornadogenesis occurs in a two-part process. First, momentum surges associated with both the system rear inflow jet (RIJ) and convective downdrafts enhance rear-to-front flow within the developing bow-echo line pattern. Convergence in the region of a developing mesovortex is enhanced by these surges, forcing subsequent low-level updraft formation. This updraft stretches vertical vorticity, increasing rotation considerably. Next, the increasing vorticity at low levels induces an occlusion downdraft, which tilts vortex-region horizontal vorticity into the vertical and allows for further updraft-supported

vertical vorticity stretching. These two processes working in conjunction with one another increase the intensity of the mesovortex, eventually leading to tornadogenesis. Mesovortex strength is maintained via a combination of streamwise and crosswise horizontal vorticity tilting within the vortex region.

Chapter 1

Introduction

The United States is arguably one of the most tornado-prone regions in the world, experiencing damage to property and loss of life every year as a result of this class of severe storms. Though most of these tornadic events occur in association with discrete, supercellular thunderstorms, a proportion of them also occur in conjunction with Quasi-Linear Convective Systems (QLCSs). 3,828 tornado events were recorded between 1998 and 2000; 79% of these tornadoes were spawned from supercells, and an additional 18% spawned from QLCSs (Trapp et al. 2005). This study also highlighted the tendency for more QLCS-induced tornadoes to form during the cool season when compared to supercell-induced ones, illustrating that this particular variety of storms and their associated tornadoes posed a threat beyond the traditional “tornado season.” A later study from Ashley et al. (2019) reached similar conclusions, finding that with a large proportion of all tornadic QLCS events in a 22-year climatology occurred during the cool season. Over 40 % of the cool season tornadic events were the product of QLCS-induced circulations. Additionally, Ashley et al. (2019) highlighted that QLCS tornadoes occurred over a broad geographic region of the United States, with observed tornadoes occurring in essentially all of the eastern half of the country. *Figure 1.1* details the proportion and geographic extent of QLCS-produced hazards in the US. The Midwest, Great Plains states, Southeastern states, and portions of the Northeast US were impacted by at least one tornado during the climatological period of record (Trapp et al. 2005; Ashley et al. 2019). Finally, Trapp et al. (2005) found that QLCS tornadoes tend to occur later at night than their supercell-generated counterparts, peaking in

activity between 2300-0300 LST. Ashley et al. (2019) reached similar conclusions, noting a peak in QLCS-associated tornado activity between 00:00 and 06:00 LST. The propensity of QLCSs to produce severe winds and tornadoes, their ability to occur over a large portion of the country, their aptitude for produce damaging weather events during the cool season when they may be less anticipated, and their tendency to occur during the late evening, overnight, and early morning hours underscores the importance of understanding the processes behind tornadogenesis of these QLCSs.

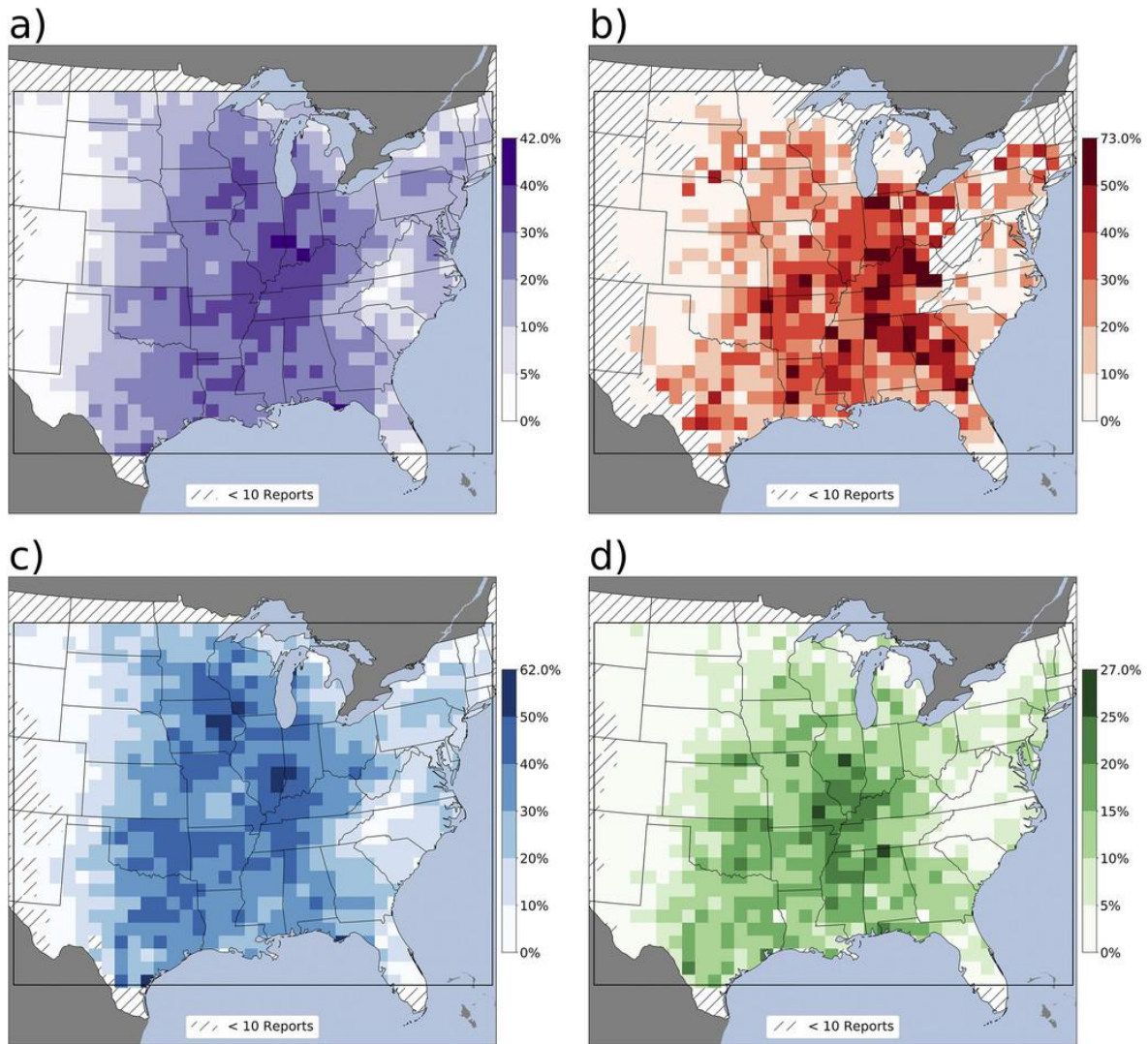


Figure 1.1: The percentage of all thunderstorm hazards in 80km x 80km grid cells produced by QLCSs; (a) all severe events, (b) tornadoes, (c) non-tornadic severe winds, (d) severe hail.

Adapted from Ashley et al. (2019)

Chapter 2

Background and Motivation

2.1 Quasi-Linear Convective System Background

During the early part of the 1970's and 80's, a multitude of studies focusing on the structure, mechanisms, and behavior associated with convective phenomena in the United States were undertaken. Although the inclination of individual thunderstorms to congeal together into organized complexes was well-recognized at the time, and was often observed in-situ (Fujita 1955; Newton 1960), the understanding of how convective organization occurred was lacking. Similarly, the structural details of thunderstorms remained largely unknown, as most studies completed in this time were focused on synoptic-scale analyses, or ground/aircraft based damage surveys (i.e. Fujita 1955). A great number of theories to classify and explain the occurrence of tornadoes, severe winds, convective system organization, as well as numerous other thunderstorm-associated phenomena were introduced during this period of research.

Later, R. Houze began the classification of linear mesoscale convective systems (MCSs) in the 1980's, postulating that both "hot towers" and the cirrus surrounding them were thermodynamically active in tropical MCSs, and have organizational effects upon the systems associated with them (1981). Gamache and Houze (1982) expanded upon this classification using radar, identifying two distinct regions of the system: the leading squall line, and the post-squall anvil region. The leading squall line was characterized by rapidly fluctuating radar reflectivity echoes in excess of 38 dBZ, strong radar reflectivity gradients, and heavy

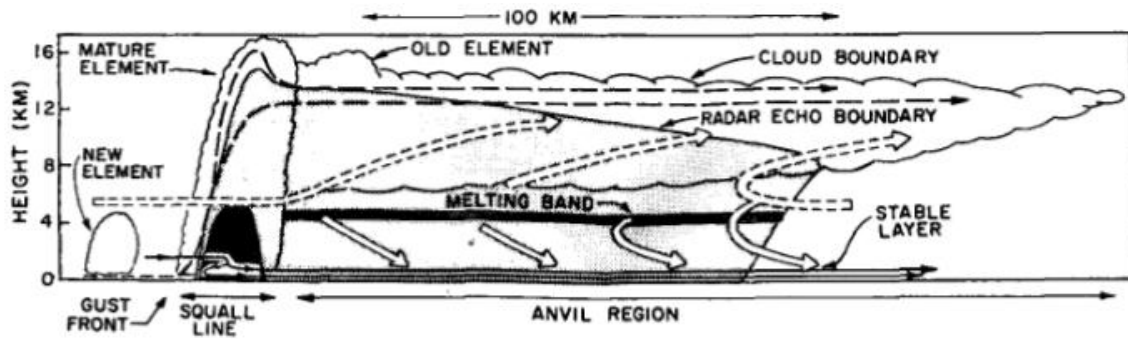


Figure 2.1: A schematic diagram of a tropical squall line, as presented in *Fig. 1* of Gamache and Houze (1982).

rainfall production (exceeding 14 mm hr^{-1}). Furthermore, Gamache and Houze described the post-squall anvil region as a region characterized by reflectivities below 38 dBZ, and having highly uniform, weak reflectivity gradients (*Figure 2.1*). Studies from other researchers (i.e. Ogura and Chen 1977, Ogura and Liou 1980) corroborated these findings, confirming that few, if any, structural differences existed between tropical and mid-latitude MCSs.

The propensity of these types of systems to produce impactful severe weather was also documented in literature at this time, as the association between MCSs and straight-line wind events, and/or tornadoes was highlighted via the use of damage analyses, radar analysis, and eyewitness accounts (Fujita 1981; Houze and Hobbs 1982; Forbes and Wakimoto 1983; Wakimoto 1983; Kessinger et al. 1987). Additionally, a clearer picture of midlatitude MCS structure was presented by Houze et al. (1989), elucidating a detailed conceptual model of a mature, well organized squall line (c.f. *Figure 2.2*).

Another name for MCSs (employed by the author of this thesis) is “Quasi-Linear Convective Systems (QLCSs).” Once again referring to the definition from Houze et al. (1989), QLCSs are a type of MCS possessing the following traits: having one length dimension of 100-500 km, featuring vigorous convection, and producing instances of severe weather during some part of its lifetime. The convective complex can often be divided into three main

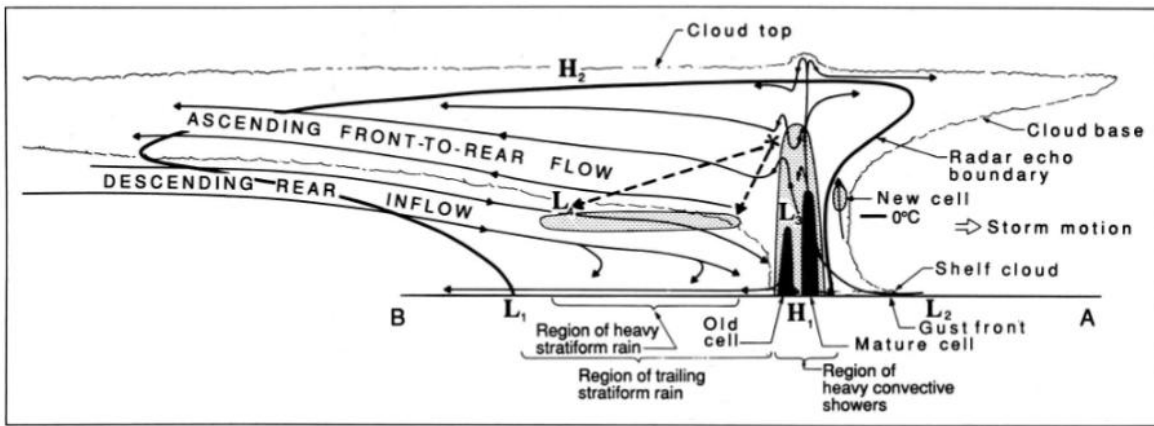


Figure 2.2: Conceptual model of a squall line with a trailing stratiform area viewed in a vertical cross section oriented perpendicular to the convective line (i.e., parallel to its motion). Adapted from Houze et al. (1989).

regions: the Leading Convective Zone, which features vigorously convecting thunderstorms, the Transition Zone, having numerous decaying thunderstorms, and the Trailing Stratiform Region, characterized by a widespread area of significantly less convective stratiform-type precipitation. The author of this thesis creates a distinction between the two types of systems in order to differentiate QLCSs, which have an affinity for producing severe weather, to non-severe MCSs with varying organizational modes.

With the appearance of vast amounts of new data from both higher-resolution, increasingly complex computer models, from the nationwide Next-Generation Radar (NEXRAD) network, and from QLCS-focused field experiments (such as the Bow-Echo and Mesoscale Convective Vortex Experiment, BAMEX; Atkins et al. 2005), studies of specific QLCS features accelerated. Bookend/mesoscale convective vortices (MCVs) (Biggerstaff and Houze 1991; Skamarock et al. 1994; Davis and Weisman 1994; Weisman and Davis 1998), patterns contributing to the maintenance of the convective system (Rotunno et al. 1988; Weisman 1992; Skamarock et al. 1994), and various other features producing severe winds and tornadoes (Fujita 1981; Jorgensen and Smull 1993; Przybylinski 1995; Weisman and Davis 1998;

Funk et al. 1999) were more thoroughly investigated. Research focused upon these topics continue to this day, and have supported the investigation of QLCS produced tornadoes, made way for the discovery of new features (such as leading line mesovortices), and have allowed meteorologists to deepen their understanding of MCSs as a whole.

2.2 QLCS Features

2.2.1 The Sustaining Role of Wind Shear and the Rear Inflow Jet

QLCSs maintain their longevity via numerous features and processes, most notably by a process outlined by Rotunno et al. (1988). Storms within a developing QLCS are influenced by the ambient environmental vertical wind shear, as horizontally-oriented vorticity is generated along the leading edge of the developing system. This vorticity drives the appearance of a rotor-like feature which enhances lifting along the edge of the storms' gust front. This vertical wind shear also works to restrain outflow at low levels, preventing updraft undercutting from rain cooled air. As the original convection decays and new storms are initiated along the boundary, cold pools from individual convective elements grow in size, eventually congealing into a system-scale cold pool as the system acquires linear organization. The cold pool deepens as storms continually produce evaporatively-cooled air and precipitation. The juxtaposition of the cold pool's leading edge with relatively warm, positively buoyant inflow air generates horizontally-oriented baroclinic vorticity of opposite sign to the environmental wind shear-generated horizontal vorticity. The interaction of these two horizontal vorticity features further prolongs the life of the system by intensifying upward lifting and convergence along the gust front boundary of the complex. Finally, the development of this vorticity configuration ensures that minimal updraft entrainment of cool, less buoyant air occurs, which ensures the longevity of the convective complex. At this time, the now mature MCS acquires near vertical (or slight upshear) tilt, maximizing the updraft vertical velocities.

The favorable configuration of vorticity, enhanced convergence, and upright/nearly upright updraft vertical alignment maintains the system's updraft and ensures it remains intense with time.

The balance between the environmental wind shear-generated vorticity and cold pool generated vorticity is of paramount importance to sustaining the QLCS for long periods of time. If the strength of the cold pool increases, the system moves into an area of reduced surface buoyancy, or environmental shear increases substantially, this balance will be disrupted, and the QLCS structure will begin to decay. If shear is decreased, instability is decreased, or the cold pool strength is enhanced, updraft formation will be inhibited and the system will tilt further upshear. This upshear tilting will decrease the strength of the updraft, marking the decaying stage of the complex.

Another feature that supports the lifecycle and severe-weather potential of a QLCS is the rear-inflow jet (RIJ): a narrow current of air that feeds into both the stratiform precipitation region and rear of the vigorous convective region at mid-levels (Biggerstaff and Houze 1991; Weisman 1992). The rear inflow jet forms due to a combination of thermodynamic (i.e. mesolow formation within the convective portion of the complex, or within the bright banding region in the stratiform region, see Biggerstaff and Houze (1991)) and kinematic factors (balance of vorticity between the cold pool and ambient environment, as outlined in Weisman (1992), or the existence of mesoscale convective vortices along the northern and southern flanks of a convective line see Wakimoto et al. (2015)). As these processes act upon the system (or in concert with one another) a midlevel, rear-to-front (storm relative) jet of air is formed. During the lifecycle of the QLCS, this jet can interact with the complex in constructive or destructive manners. If the RIJ remains elevated at the rear of the system, it can induce a large degree of upshear updraft tilt. If this RIJ remains elevated, it can inhibit the intensification of the complex and may eventually lead to the dissipation of the QLCS entirely. Conversely, the RIJ can also descend as it travels towards the front of the complex,

approaching the edge of the cold pool and effectively weakening the cold pool-induced vorticity along the leading edge of the complex. If this descending RIJ appears in systems where cold pool-induced horizontal vorticity has overwhelmed the ambient environmental horizontal vorticity, introduction of this jet along the upper portion of the cold pool circulation can allow the aforementioned horizontal vorticity arrangement to re-attain a balanced state. Reestablishing this balance allows the convective updrafts to become vertically-aligned once again, which again enhances QLCS convection once again (Weisman 1992). This process has been documented in both QLCSs and non-severe MCSs, and is often significantly more intense in severe QLCSs. The RIJ has also been identified as the source of dry, cool air that can bolster downdrafts within the complex via evaporational cooling/diabatic effects. These effects enhance the strength of the cold pool, and can also induce severe wind gusts along the leading edge of the system (Smull and Houze (1987); Wakimoto et al. (2006)).

2.2.2 Mesovortex Formation Mechanisms

QLCSs also contain embedded circulations within the leading convective line. These features are often 2-5 km in diameter (smaller than other storm-scale circulations such as mesoscale convective vortices, MCVs), and typically appear near the leading edge of the parent QLCS. The vortices are therefore classified as mesoscale- γ scale vortices (mesovortices), following the classification criteria as defined by Orlanski (1975). Jorgensen and Smull (1993); Przybylinski (1995); Weisman and Davis (1998); and Funk et al. (1999) confirmed that mesovortices can be associated with severe winds and tornadoes produced by a severe squall line. QLCS mesovortices are typically shallow in their vertical extent, presenting primarily in the lowest 2-3 km of the atmosphere (Atkins et al. 2005). Tornadic mesovortices generally exhibit higher rotational velocities than non-tornadic ones, have greater vertical extent than non-tornadic vortices, and last longer than non-tornadic circulations (Atkins et al. 2004, 2005).

Hypotheses of mesovortex formation range widely, from release of horizontal shearing instability (HSI) (Forbes and Wakimoto 1983; Przybylinski 1995) to the tilting of storm-induced horizontal vorticity by storm scale vertical drafts (Trapp and Weisman 2003; Atkins and St. Laurent 2009b). It is likely that many hypotheses partially explain how mesovortex formation occurs and how mesovortices maintain rotation thereafter. Two initial, widely-accepted theories to explain mesovortex formation involve the tilting of originally horizontal, baroclinically-generated vorticity by a storm scale updraft or downdraft. This tilting results in the creation of vertically-oriented vorticity along the leading edge of the system, which then undergoes stretching in the storm-scale local updraft. This conceptual model proposes a mechanism for the development of initial mesovortex rotation, sharing similarities with other types of mesoscale circulations (i.e. supercell mesocyclones, Markowski and Richardson (2010)) that go on to produce tornadoes.

Within this conceptual model, downdraft-induced tilting was implicated as the primary contributor to vortex formation. Trapp and Weisman (2003) confirmed the importance of the “balanced” or slightly cold pool dominant vorticity structure outlined in Rotunno et al. (1988) and Weisman (1992) to QLCS tornadogenesis. The juxtaposition of nearly vertically aligned updrafts in the presence of a vortex favors the intensification of rotation, as efficient stretching of vertical vorticity occurs when updrafts intensify quickly with respect to height (vertically-aligned updrafts resist entrainment-induced weakening efficiently, Markowski and Richardson 2010). Furthermore, Trapp and Weisman (2003) found that including Coriolis forcing strengthened cyclonic vortices and weakened anticyclonic vortices, explaining how cyclonically-rotating vortices predominate in observed QLCS cases.

A second theory of mesovortex generation was proposed by Atkins and St. Laurent (2009a), citing the updraft induced horizontal baroclinically-generated vorticity tilting that occurs along the leading convective line as the process giving rise to mesovortices. The RIJ-induced surge in the QLCS’s outflow is also highlighted in this study, as it would enhance

convergence along the leading edge of the QLCS. This enhanced convergence forces the formation of new updrafts along the recently formed a bow-echo reflectivity pattern (Nolen 1959), and induces tilting of southward-pointing vortex lines, creating contra-rotating vortex pairs along the leading edge of the bow echo. The cyclonic (anticyclonic) couplet would be located along the northernmost (southernmost) apex of the bow, intensified (weakened) by Coriolis forcing acting upon parcels entering each mesovortex (Atkins and St. Laurent 2009b).

Additional high resolution data-assimilation based studies, such as Schenkman et al. (2012) have attempted to integrate observational data into high-resolution convection allowing models, yielding detailed observations of mesovortices and associated tornadogenesis processes. From the aforementioned study, rapidly intensifying low-level updrafts and rotor-like features were identified in the 8-9 May 2007 Central Oklahoma tornadic MCS. These rapidly intensifying updrafts and rotor features occurred along, or just behind the storm's gust front. The kinematically-enhanced updraft that formed to the northwest of the bowing segment acted to greatly increase the intensity of the vortex; enhanced upward motion within the updraft augmented vorticity tilting and vertical vorticity stretching, yielding a vigorous mesovortex intensification. The juxtaposed horizontal rotor was also identified as a source of horizontal vorticity that interacted with circulation/circulation associated updraft, likely intensifying it as it did so.

High-temporal resolution observations obtained during the PECAN field campaign in 2016 show that mergers of vorticity maxima in the vortex region could indeed act to strengthen subtornadic mesovortices into tornadic ones(Flournoy and Coniglio 2019). Furthermore, trajectory analyses of parcels within the mesovortex region at the time of tornadogenesis have highlighted numerous source regions for circulation-bound parcels. Flournoy and Coniglio (2019) found that parcels within the mesovortex and parcels just to the north of the mesovortex-associated updraft at the time of tornadogenesis originated near the surface, and

that the source region of these parcels was likely the pre-squall line environmental air. Environmental parcels gradually acquired more and more vertical vorticity as they approached the mesovortex, encountering the coincident updraft and undergoing rapid vorticity intensification as a result. Flournoy and Coniglio (2019) also discovered that parcels within the vortex region possessed large values of primarily crosswise-oriented horizontal vorticity, requiring modification via updraft-induced tilting processes to accrue vertical vorticity.

Mesovortex behavior has also been postulated to be at least loosely modulated by the RIJ/rear inflow surges, as enhanced rear inflow has been observed just before the intensification of the squall line and/or tornadic mesovortices (Jorgensen and Smull 1993; Atkins et al. 2004, 2005; Atkins and St. Laurent 2009a; Xu et al. 2015). Additionally, as discussed in *Section 2.2.1*, the RIJ exerts considerable control over the intensity of the leading convective cells, updraft vertical orientation, and the propensity for the complex to produce impactful severe weather (either as a direct result of a descending RIJ, or from the creation of additional strong convection along the leading line of the QLCS). Moreover, Flournoy and Coniglio (2019) found that RIJ-originating parcels have considerable magnitudes of vertical vorticity that can bolster mesovortex circulation upon reaching the surface or being stretched in a thunderstorm updraft. The RIJ can also expand QLCS cold pools, bolstering their depth and increasing their propagation speed, which will strengthen convergence along the storm scale gust front. This allows for a local acceleration of the gust front and associated convective motions, creating a localized bulge in the convective line (Atkins et al. 2005; Schaumann and Przybylinski 2012).

Additional frictional effects at the Earth's surface have been postulated to contribute to mesovortex intensification and nascent tornadogenesis processes. Xu et al. (2015) found in numerical simulations that the formation of an eastward-tilted vortex tube results when RIJ induced rear-to-front flow interacts with the surface. This frictionally-generated vortex tube

tilted into the vertical along the gust front by an enhanced updraft and subsequently stretched, intensifying vertical vorticity to tornadic levels and augmenting the tornadogenesis process.

2.3 Synoptic and Event Background

On the evening of 13 April 2018, a severe, long-lived squall line advanced across portions of eastern Texas and northern Louisiana, resulting in reports of damage and fatalities. This quasi-linear convective system (QLCS) moved through the region just following a supercell-driven severe weather outbreak earlier in the afternoon. In the county warning area of the Shreveport, LA National Weather Service, 17 tornadoes were confirmed, with many ranking at EF-1 on the Enhanced Fujita (EF) damage scale (NWS Shreveport, LA 2018). One tornado produced by the QLCS was of particular interest, exhibiting unusual behavior and persisting for over 30 minutes before finally dissipating. Reports of tornadoes and severe winds continued to accompany the QLCS until the early morning of 14 April, when the system weakened to sub-severe limits and became disorganized. The system once again re-intensified over the Southeastern United States (SE US) on the following day.

Synoptic conditions that precluded the formation of the system are typical to that observed in the SE US during the spring season. At 1200 UTC on 13 April 2018, a deep longwave trough moved over the western half of the United States, with its axis centered upon the four corners region. A seasonably-strong jet streak was emerging from the base of the trough, contributing to a maximization of both cyclonic shear and cyclonic curvature vorticity advection in the Texas and Oklahoma Panhandles (images c. & d. in *Figures 2.3* and *2.4*). Additionally, the left exit region of the associated jet streak was emerging from the base of the Rockies, maximizing divergence aloft in this region. At lower levels, warm air advection was fostered by the presence of a strong, southerly 50-60 knot jet at 850 hPa. Quasi-Geostrophic ω (QG- ω) analysis in this region yields strong upward motions, encouraging the formation of a low-pressure system. At the surface, an open wave was present as a new low pressure center was developing in Kansas. *Figure 2.3* details the synoptic scale features associated with this system at 1200 UTC on 13 April. By 0000 UTC on 14 April,

this trough and attendant jet streak had emerged into the Southern Great Plains, with strong upper-level divergence occurring in the region. A closed circulation had developed in the upper levels, indicating that the low pressure system had further deepened. These combined conditions allowed for the development of discrete supercells by the evening in north Texas. A 40-55 knot, 850 hPa jet streak gradually intensified, promoting greater low-level wind shear, increasing warm-air advection, and magnifying northward moisture transport over time. *Figure 2.4* illustrates the synoptic setup at 0000 UTC on 14 April. These conditions maintained convective storms after sunset, and led to the formation of a QLCS as the supercells in the region congealed together, moving into east Texas by 0200 - 0300 UTC. *Figure 2.5* and *Figure 2.6* illustrate the effects of this jet on the environment, as ample amounts of warm, moist air were present under very strong 0-1 km bulk wind shear and storm-relative helicity values on both skew- t /log- p diagrams. Appreciable convective instability was maintained into the overnight hours of 13-14 April, with soundings showing around $1,300 \text{ J kg}^{-1}$ mixed-layer CAPE at 0503 UTC. This environment intensified the QLCS as it moved into the area, leading to robust convection and the formation of multiple tornadic QLCS mesovortices.

Figure 2.7 details the appearance of the initial storms as they began to undergo upscale growth into the QLCS in a composited radar image from KFWS and KGRK. Storm coverage continued to expand, growing upscale into the complex that would reach Louisiana by 0000 - 0100 UTC. As it continued to push eastward into the warm, unstable airmass, storm reports began to occur at 0215 UTC, including wind damage and sporadic tornado reports in eastern Texas. By 0300 - 0400 UTC, the complex had begun to exhibit a distinct bow echo shape, with the apex centered over I-20 near Longview, TX. *Figure 2.8* details the QLCS appearance from the KSHV and OU Shared Mobile Atmospheric Research and Teaching Radars (SMART-R) as the Shreveport-Bossier City EF-1 tornado occurred. As the squall line moved across the region overnight, other mesovortices intensified and contributed to the

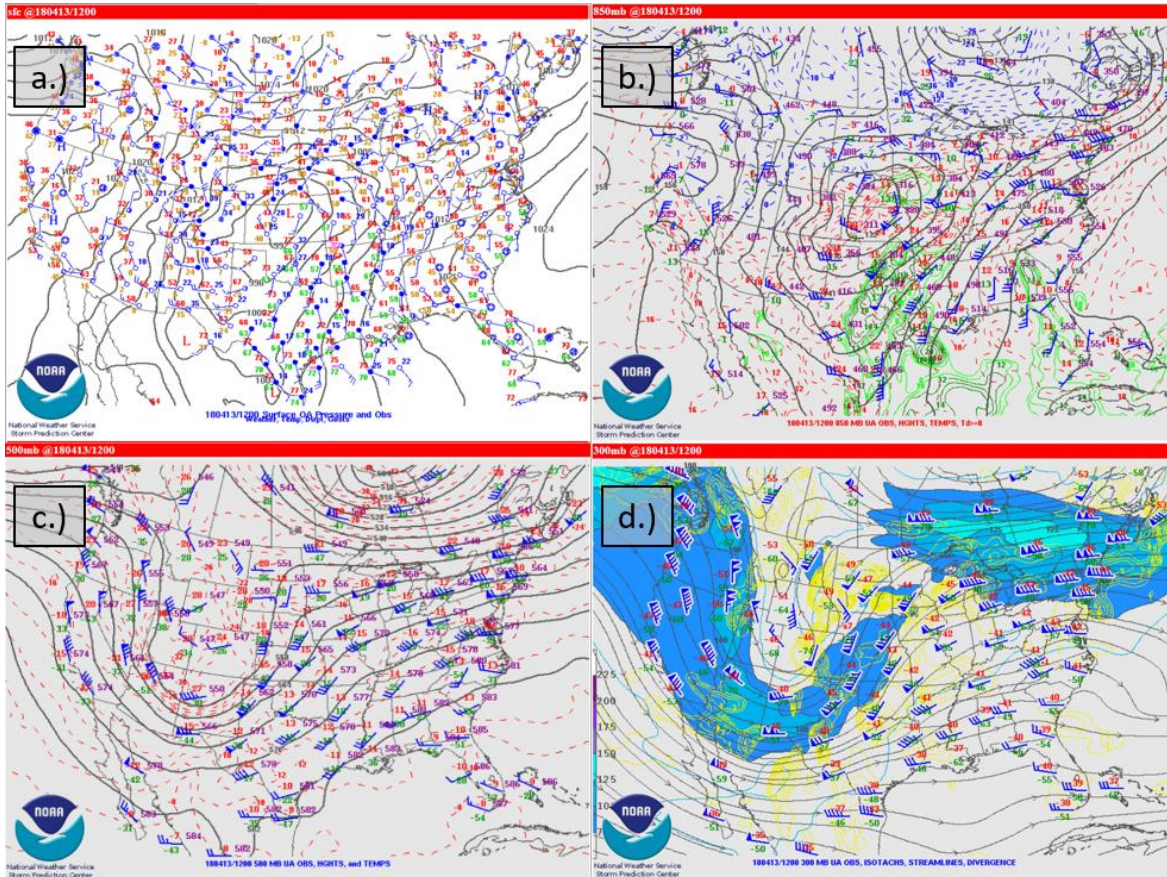


Figure 2.3: Synoptic-scale analyses at 1200 UTC on 13 April, at the (a) surface, (b) 850 mb, (c) 500 mb, and (d) 300 mb levels. Images taken from the Storm Prediction Center (2018).

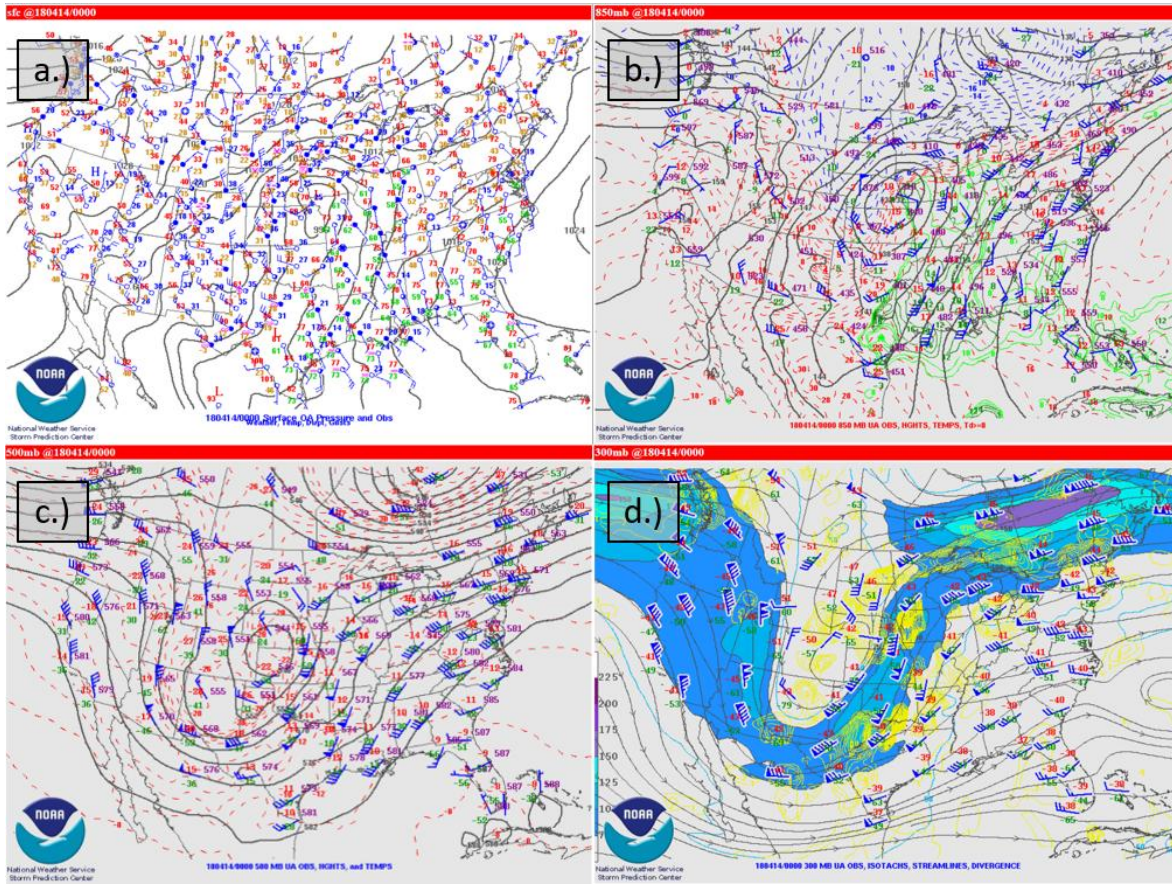


Figure 2.4: As in *Figure 2.3*, but for 0000 UTC on 14 April.

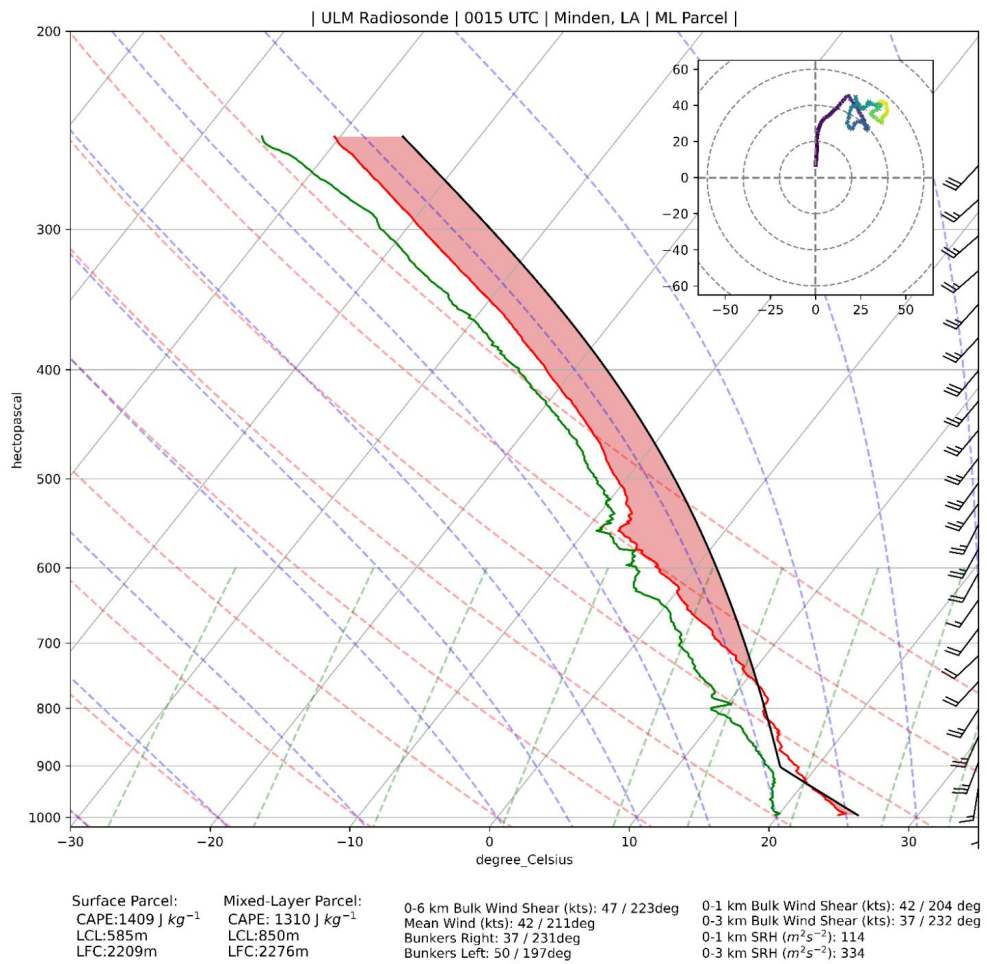


Figure 2.5: Skew-T of the environment in NW Louisiana at 0015 UTC on 14 April 2018.

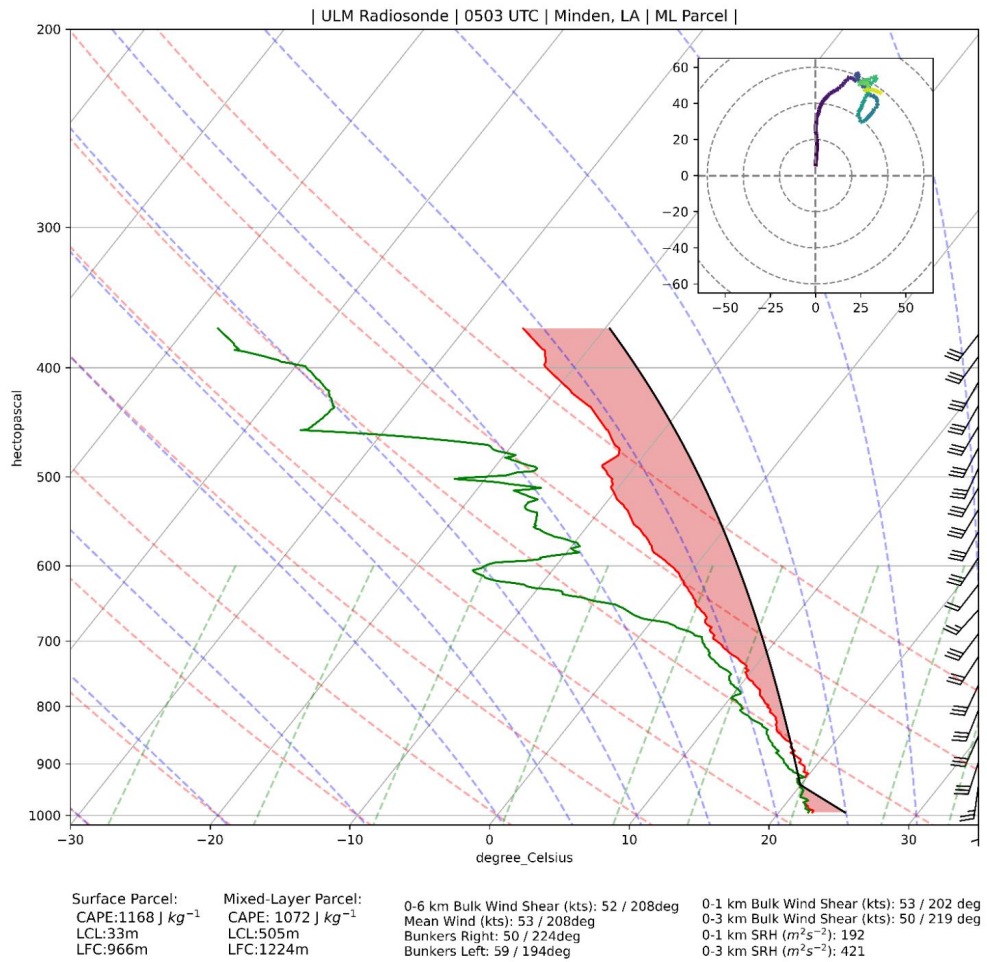


Figure 2.6: As in Figure 2.5, but for 0503 UTC.

generation of multiple tornadoes and many wind reports. The complex weakened and became disorganized as it reached the far eastern edge of Louisiana at 0900 UTC (see *Figure 2.9*).

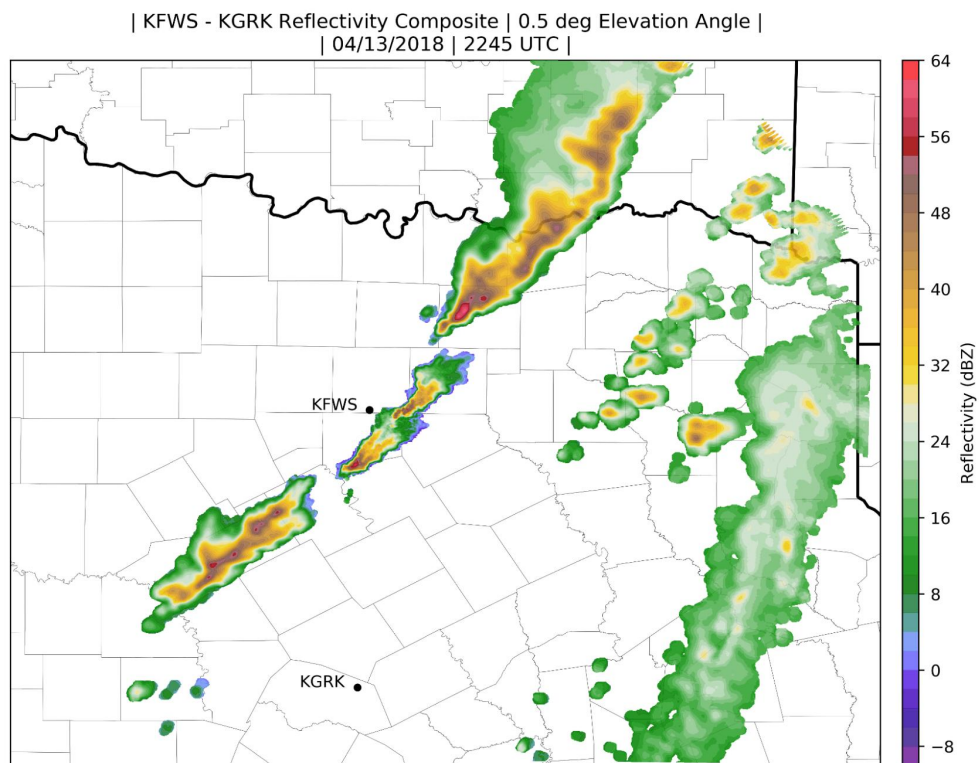


Figure 2.7: Radar reflectivity composite of convection that would eventually become the QLCS as it initiated in North Texas.

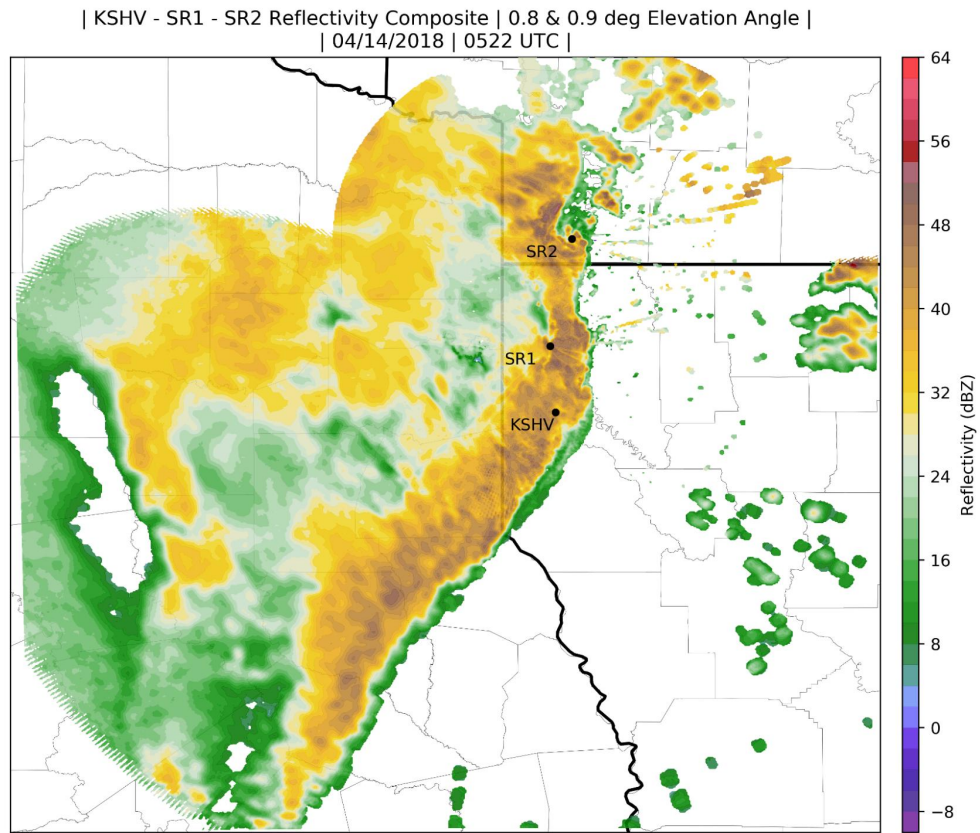


Figure 2.8: As in *Figure 2.7*, but for 0522 UTC, and using data from KSHV, SMART-R1, and SMART-R2.

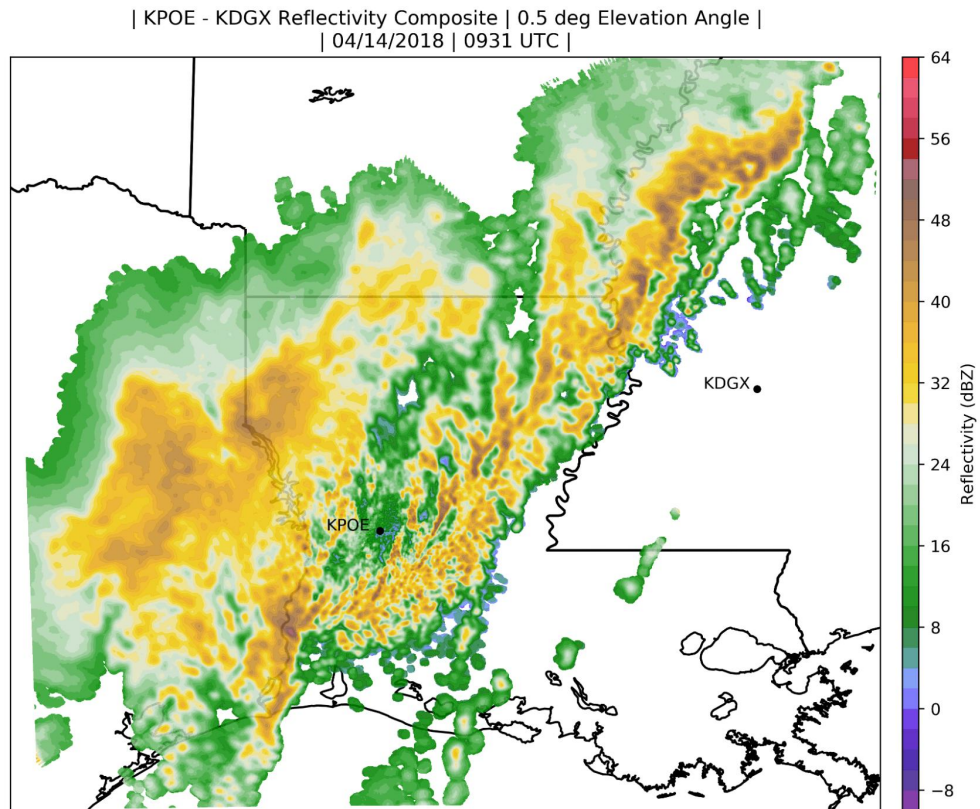


Figure 2.9: As in *Figure 2.7*, but for the decaying period of the QLCS, and using data from KPOE and KDGX.

Chapter 3

Methods

3.1 Doppler Radar Configurations

Multiple radars were deployed to investigate the QLCS from this case, allowing for the construction of two separate analysis domains with dual-Doppler coverage. The first of these domains contained data from both SMART-Radars (SMART-R1 and SMART-R2). Aligned in a south-southwest/north-northeast orientation, the two radars were deployed along a 45.8 km baseline with one another, creating a broad area where the cross-beam angle was large enough to produce useful wind retrievals (see *Figure 3.1* for the dual-Doppler domain formed by SMART-R1 and SMART-R2). This large domain covers both circulations of interest within the period, allowing for analysis of wind fields to be conducted on each vortex through an extensive period of their lifecycles. An additional domain between SMART-R1 and the KSHV WSR-88D was also created; SMART-R one was deployed north-northwest of KSHV, creating a north-northwest/south-southeast oriented, 28 km baseline between the two radars. The shorter baseline decreased the total area of the analysis domain, but still allowed for high spatial resolution scans of the mesovortex at low-levels. As mesovortex maintenance processes predominate at these low-levels, the analysis benefited from this domain configuration (see *Figure 3.2* for the dual-Doppler domain created between KSHV and SMART-R1). However, temporal resolution was significantly lower than it was in the SMART-R1/SMART-R2 domain, due in part to the WSR-88D's relatively slow volumetric update times of around seven minutes. This reduced the number of analysis times that could be generated, and

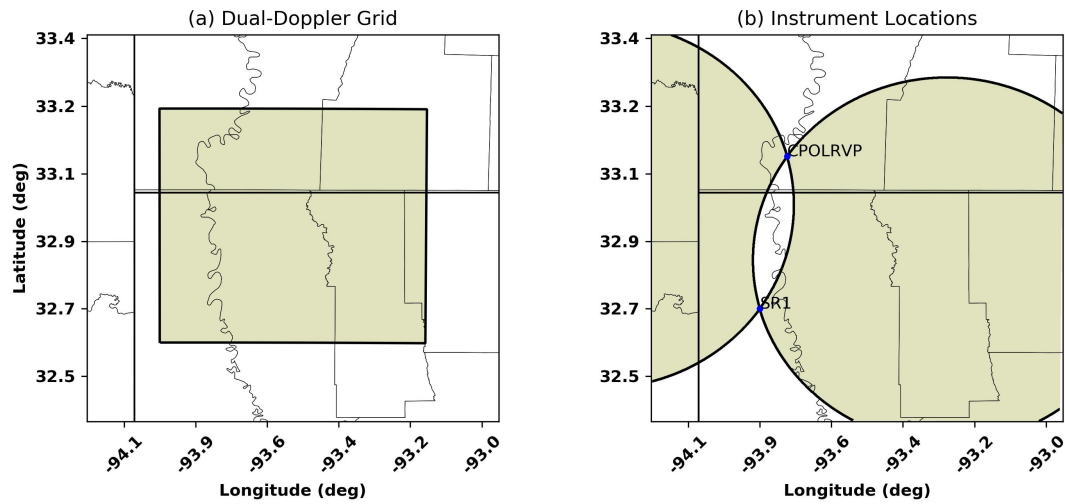


Figure 3.1: The dual-Doppler domain produced by SMART-R1 and SMART-R2; note that SMART-R2 and CPOLRVP are synonymous.

led to greater time periods between subsequent analysis steps. Additionally, mesovortex #1 (Shreveport-Bossier City, LA) crossed both of the analyses' baselines at tornadogenesis time, reducing the time that wind retrievals could be synthesized for this particular circulation and limiting the number of observations of the intensification process of mesovortex #1. This was not an issue for mesovortex #2, however, as it remained within the SMART-R1/SMART-R2 domain over the course of its lifecycle. Radar scanning strategies for the SMART-Radars were optimized to observe low-level mesovortices, prioritizing rapid temporal updates at low levels and high nyquist velocities over long range data acquisition. This led to volumetric updates on the order of two to three minutes, allowing for higher temporal resolution during the times in which mesovortices intensified, became tornadic, and dissipated.

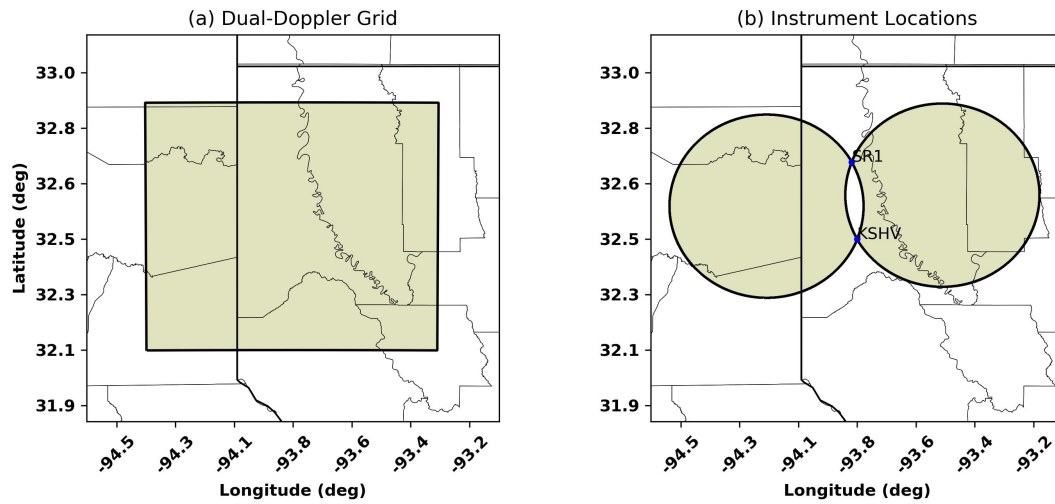


Figure 3.2: The dual-Doppler domain produced by SMART-R1 and KSHV.

3.2 Radar System Description

3.2.1 KSHV WSR-88D

The Weather Surveillance Radar 1988-D (WSR-88D) is an S-band ($\lambda \approx 10$ cm), Doppler radar used by the National Weather Service, broadcasting at a peak power of 750 kW, and providing a continuous feed of radar data to forecasters and the general public alike (Crum and Alberty 1993). The WSR-88D system was a joint development between three federal agencies in the United States to address common needs fulfilled by pulsed Doppler radar systems: the Department of Commerce (DoC), the Department of Defense (DoD), and the Department of Transportation (DoT). The development of the system benefited from numerous novel and cutting edge innovations made in the 1980's in countless fields (i.e. mesoscale meteorology, signal processing, radar engineering, etc...). Each radar installation consists of multiple systems operating in tandem with one another: the Radar Data Acquisition Unit (RDA), Radar Products Generator (RPG), and the Principal User Processor (PUP). The RDA

consists of the radar itself; an S-band klystron transmitter, pedestal, reflector dish, receiver, and signal processor are principal components of this sub-system. Parameters such as the pulse repetition frequency (PRF), pulse width (τ), and elevation/azimuthal scanning speeds can be customized based on what type of observations are desired by the user. The RPG receives data from the RDA, passing it through algorithms and various calculations before returning end user-accessible products for the PUP (i.e. hail detection algorithms, Velocity Azimuth Displays (VADs), storm tracks, tornadic vortex signatures (TVSs)). Radial resolution of the system is approximately 250 m, and the data resolution is approximately 0.5 m s^{-1} . The particular radar utilized in this study is installed on the property of the National Weather Service in Shreveport, LA, (lat/lon: $32.450795^\circ \text{ N}$, $93.841267^\circ \text{ W}$), and covers northwest Louisiana. KSHV was barely missed by the circulation associated with Mesovortex # 1, allowing for a rare, close range dataset of a tornadic mesovortex to be collected by the radar. Eight volumes of interest were collected by KSHV over the lifecycle of the tornadic circulation.

3.2.2 SMART-Radars

The Shared Mobile Atmospheric Research and Teaching Radars (SMART-Rs) are a pair of mobile, C-band, research Doppler radars, currently owned by the University of Oklahoma. Operating at 250 kw peak power output and having radial resolutions of 37 meters, the SMART-Radars can provide high-resolution, attenuation-resistant, rapidly-updating scans of mesoscale features of interest (Biggerstaff et al. 2005). As the platform is intended to be utilized primarily as a research radar, scanning strategies are highly modifiable, and any number of different patterns may be used over the course of data collection, depending on user preference. Additionally, the SMART-Radars have the ability to perform scans on a schedule, allotting them the unique ability to collect data in a synchronized manner with one another or with another radar system (such as the WSR-88D). Upgrades made to both

SMART-Radars have created dual-polarization capability, allowing for microphysical characteristics of hydrometeors in a scanning volume to be ascertained. This dual-pol capability facilitates the interrogation of processes not only related to thunderstorms and tornadoes, but to electrification, hydrometeor classification, and numerous other mesoscale phenomena. Due to the SMART-Radars' mobile nature, they can deploy in a wide variety of locations, expanding meteorologists' ability to interrogate meteorological phenomena, especially when they are deployed together and scanning strategies are synchronized, or when operating in conjunction with other radar systems.

3.3 Analysis Methods

3.3.1 Radar Data Collection and Processing

Both SMART-Radars were deployed in the Northwest Louisiana/Southwest Arkansas region on 13 April 2018 in anticipation of severe weather. As the first rounds of supercell thunderstorm-associated severe weather exited the region, SMART-Radars remained on location in anticipation of the building QLCS in East Texas; this QLCS moved into the SMART-R1/SMART-R2 and SMART-R1/KSHV dual Doppler domains by midnight on 14 April. Both SMART-Radars utilized scanning strategies optimized for low-level data collection at high temporal resolution, with SMART-R1 utilizing two separate scanning strategies (a full 360 deg PPI scan, and a sector scan) and SMART-R2 utilizing a single sector scans. Details of these scanning strategies are listed in *Table 3.1*. Elevations in SMART-Radar PPI (sector) mode ranged from 0.8 to 19.6 deg (0.5 to 18.2 deg). The KSHV WSR-88D operated in volume coverage pattern 212 (VCP 212) for the duration of the event.

Radar	τ (μs)	PRF (Hz)	R. Max (km)	# Elevations	Nyquist ($m s^{-1}$)
SMART-R1 (PPI)	0.5	1,800	83.275	14	24.12
SMART-R1 (Sector)	0.5	1,500	99.930	17	20.10
SMART-R2	0.25	1,800	83.276	17	23.99

Table 3.1: Radar scanning strategies utilized during data collection; PRF: Pulse Repetition Frequency.

After radar data was consolidated, a single volume from each of the three radars was post-processed using the manual radar data editor Solo 3 (Oye et al. 1995). Collected radar data was first thresholded in the reflectivity and velocity fields based on the signal quality index (SQI), a measure of the quality of a radar return based on the noise of the sampled data. Radar

gates possessing less than 0.15 SQI (SMART-R1) or 0.175 SQI (SMART-R2) were removed from volumes, ensuring only high-quality data with relatively low noise was included in the analysis. Care was employed to select an SQI value that did not distort mesovortex signatures or remove other features of interest in the radar data. Next, data was despeckled and excessive remaining ground clutter or anomalous data was manually removed from the volume, rendering the radar data ready for the next step of processing. Radar velocity data was then dealiased based on the nyquist velocity of the observed data. After all radar data was despeckled, thresholded, ground clutter was removed, and velocities dealiased, the data was imported into an automated algorithm to process the large number of data volumes. The path to an edited volume was given to an objective velocity dealiaser included in the Python ARM Radar Toolkit package (PyART; see Helmus and Collis (2016) for details), providing a “truth” volume for the region-based editor to utilize in its automated algorithm and therefore increasing accuracy of the scheme. In addition, the same thresholding and despeckling was performed by the automated algorithm in subsequent radar volumes, removing erroneous or irrelevant radar data from the files, quality controlling the data utilized later in the analysis. After the automated algorithm edited the volumes of data from all radars, manual editing was once again undertaken in Solo 3, both to provide a final quality control pass on the data, and to correct any erroneous edits made by the PyART algorithm. After this, data edits were considered finished, with the resultant data being passed into the next step of the analysis.

The next step in the analysis process was to intake the edited radar volumes into the RADDISON dual-Doppler Analysis program, which interpolates the radar files (polar coordinates) to a Cartesian grid (x,y,z coordinates). The interpolation scheme is discussed in Betten et al. (2018), and yields grid point values by utilizing a natural neighbor technique (Sibson 1981). Grid parameters are user-selected, and differed between the two analyses. A table of these grid parameters can be found in *Table 3.2*.

	Vortex #1	Vortex #2
Time (UTC)	0456 ⇒ 0543	0536 ⇒ 0558
X-Domain	-50 km ⇒ 50 km	-10 km ⇒ 65 km
Y-Domain	-40 km ⇒ 50 km	-10 km ⇒ 60 km
Z-Domain	250 m ⇒ 10 km	250 m ⇒ 10 km
ΔT	6 to 7 min	2 to 3 min
ΔX	250 m	250 m
ΔY	250 m	250 m
ΔZ	250 m	250 m

Table 3.2: A summary of the interpolated Cartesian grids utilized in this case study. X,Y,Z values are relative to dual-Doppler grid center point: KSHV for Mesovortex #1, SMART-R1 for Mesovortex #2.

3.3.2 Dual-Doppler Analysis Technique, Calculations, & Visualization

Dual-Doppler wind retrievals follow the process outlined in Shapiro et al. (2009), Potvin et al. (2012b), and Potvin et al. (2012a), utilizing a 3d-Variational Data Assimilation analysis scheme.

After the dual-Doppler wind retrievals were synthesized, first order derivatives of the flow were calculated for utilization in the analysis step. Variables calculated at this time were convergence,

$$convergence = - \left(\frac{\partial u}{\partial x} + \frac{\partial v}{\partial y} \right) \quad (3.1)$$

3-dimensional vorticity,

$$\vec{\omega} = \nabla \times \vec{V} = \left(\frac{\partial w}{\partial y} - \frac{\partial v}{\partial z} \right) \hat{i} + \left(\frac{\partial u}{\partial z} - \frac{\partial w}{\partial x} \right) \hat{j} + \left(\frac{\partial v}{\partial x} - \frac{\partial u}{\partial y} \right) \hat{k}, \quad (3.2)$$

horizontal vorticity,

$$\vec{\omega} \cdot \hat{i} = \xi = \left(\frac{\partial w}{\partial y} - \frac{\partial v}{\partial z} \right) \quad (3.3)$$

$$\vec{\omega} \cdot \hat{j} = \eta = \left(\frac{\partial u}{\partial z} - \frac{\partial w}{\partial x} \right) \quad (3.4)$$

and finally vertical vorticity,

$$\vec{\omega} \cdot \hat{k} = \zeta = \left(\frac{\partial v}{\partial x} - \frac{\partial u}{\partial y} \right). \quad (3.5)$$

From these equations, terms in the Lagrangian vorticity tendency equation could be calculated as follows,

$$\frac{d\zeta}{dt} = \underbrace{\left[\left(\xi \frac{\partial w}{\partial x} \right) + \left(\eta \frac{\partial w}{\partial y} \right) \right]}_{\text{Tilting}} + \underbrace{\left[\left(\zeta \frac{\partial w}{\partial z} \right) \right]}_{\text{Stretching}}. \quad (3.6)$$

Storm relative winds were calculated by subtracting the measured storm motion from the u, v wind fields as follows (see *Table 3.3* for storm motions associated with each mesovortex).

$$U_{SR} = U_{DDA} - U_{Storm} \quad (3.7)$$

$$V_{SR} = V_{DDA} - V_{Storm} \quad (3.8)$$

Finally, the streamwise and crosswise components of vorticity tilting were of interest to

Wind Component	Vortex #1	Vortex #2
U component ($m s^{-1}$)	18.9	17.8
V component ($m s^{-1}$)	7.5	10.3

Table 3.3: Measured storm velocities for each mesovortex.

the goals of this study, and were calculated in a six-part process. First, the storm relative wind and horizontal vorticity magnitudes and directions were calculated at each point in the dual-Doppler domain, yielding vector fields of each variable:

$$|\tilde{\mathbf{V}}| = \sqrt{u^2 + v^2} \quad (3.9)$$

$$\theta_{\vec{V}_{SR}} = \tan^{-1} \left(\frac{v}{u} \right) \quad (3.10)$$

$$|\vec{\omega}_H| = \sqrt{\xi^2 + \eta^2} \quad (3.11)$$

$$\theta_{\vec{\omega}_H} = \tan^{-1} \left(\frac{\eta}{\xi} \right). \quad (3.12)$$

Second, the difference in the angle of the wind vector and the angle of the horizontal vorticity vector was calculated at each point in the analysis domain, allowing for the use of trigonometry to calculate the desired components.

$$\theta_{\Delta} = \left| \theta_{\vec{V}_{SR}} - \theta_{\vec{\omega}_H} \right|$$

After finding the difference between the wind direction and horizontal vorticity direction, the streamwise and crosswise component magnitudes of the vorticity vector, relative to the storm-relative wind flow could be calculated. The streamwise vorticity component magnitude was computed first, as this component is parallel (or anti-parallel) to the storm-relative wind direction and can be calculated using the cos relationship:

$$|\vec{\omega}_{H,sw}| = |\vec{\omega}_H| \cos(\theta_{\Delta}) \quad (3.13)$$

$$\theta_{\omega_{H,sw}} = \theta_{\vec{V}_{SR}}. \quad (3.14)$$

The direction of the crosswise vorticity vector was determined via its orientation with the vector \vec{V}_{SR} . If $\theta_{\Delta} > 0$, then $\frac{\pi}{2}$ radians were added to $\theta_{\omega_{H,sw}}$.

$$\theta_{\omega_{H,cw}} = \theta_{\omega_{H,sw}} + \frac{\pi}{2}$$

If $\theta_{\Delta} < 0$, $\frac{\pi}{2}$ radians were subtracted from $\theta_{\omega_{H,sw}}$.

$$\theta_{\omega_{H,cw}} = \theta_{\omega_{H,sw}} - \frac{\pi}{2}$$

After calculating the streamwise component of the horizontal vorticity, the crosswise vorticity component magnitude was computed, using the sin relationship:

$$|\overrightarrow{\omega_{H,cw}}| = |\overrightarrow{\omega_H}| \sin(\theta_{\Delta}). \quad (3.15)$$

In order to prepare these component magnitudes for further calculations, they were broken down further into their (x,y) components via the following equations:

$$\omega_x^{sw} = |\overrightarrow{\omega_{H,sw}}| \cos(\theta_{\omega_{H,sw}}) \quad (3.16)$$

$$\omega_y^{sw} = |\overrightarrow{\omega_{H,sw}}| \sin(\theta_{\omega_{H,sw}}) \quad (3.17)$$

$$\omega_x^{cw} = |\overrightarrow{\omega_{H,cw}}| \cos(\theta_{\omega_{H,cw}}) \quad (3.18)$$

$$\omega_y^{cw} = |\overrightarrow{\omega_{H,cw}}| \sin(\theta_{\omega_{H,cw}}) \quad (3.19)$$

Finally, the streamwise and crosswise (x,y) components were multiplied with their respective gradients in vertical motion, yielding streamwise and crosswise tilting magnitudes in the (x,y) directions:

$$\omega_{SW,x}^{Tilting} = \frac{\partial w}{\partial x} \omega_x^{sw} \quad (3.20)$$

$$\omega_{SW,y}^{Tilting} = \frac{\partial w}{\partial y} \omega_y^{sw} \quad (3.21)$$

$$\omega_{CW,x}^{Tilting} = \frac{\partial w}{\partial x} \omega_x^{cw} \quad (3.22)$$

$$\omega_{CW,y}^{Tilting} = \frac{\partial w}{\partial y} \omega_y^{cw}. \quad (3.23)$$

The components were added to yield the total magnitude of each respective vorticity component's tilting:

$$\left| \omega_{Streamwise}^{Tilting} \right| = \omega_{SW,x}^{Tilting} + \omega_{SW,y}^{Tilting} \quad (3.24)$$

$$\left| \omega_{Crosswise}^{Tilting} \right| = \omega_{CW,x}^{Tilting} + \omega_{CW,y}^{Tilting}. \quad (3.25)$$

Chapter 4

Single Doppler Analyses

4.1 Mesovortex #1

The first mesovortex traversed Shreveport and Bossier City, LA, and was associated with at least two tornadoes over the course of its lifecycle. A range of storm-scale features within the parent QLCS interacted with the vortex, influencing its behavior and tornado-producing processes. The lineage of this circulation can be traced to a bowing reflectivity field feature that occurred when broad cyclonic (anticyclonic) circulations developed along the northern (southern) fringes of this bow, akin to those described in Wakimoto et al. (2015). This bow echo reflectivity pattern and earlier, non-tornadic mesovortices became evident as early as 0315 UTC while the QLCS was still in Texas (*Figure 4.1*). The mesovortex associated with the tornado formed much later, after the bow echo matured for approximately thirty minutes. The couplet pair of cyclonic/anticyclonic circulations induced a surge of eastward-directed wind at the intersection of Anderson, Cherokee, and Smith Counties in Texas, leading to the development of the long-lived, intense, QLCS bowing segment by 0345 UTC (*Figure 4.2*).

As this well-defined bow echo reflectivity pattern surged eastward over east Texas, the bow echo continued to race ahead of the QLCS's north-south horizontal axis. As this acceleration occurred, mesovortices and attendant hook echoes were observed along the leading edge of the segment by the KSHV WSR-88D (*Figure 4.3*). Damaging winds were reported in association with this bow echo and attendant mesovortex circulations during this period, likely as the result of rear inflow enhancing the cold pool and accelerating the system's local

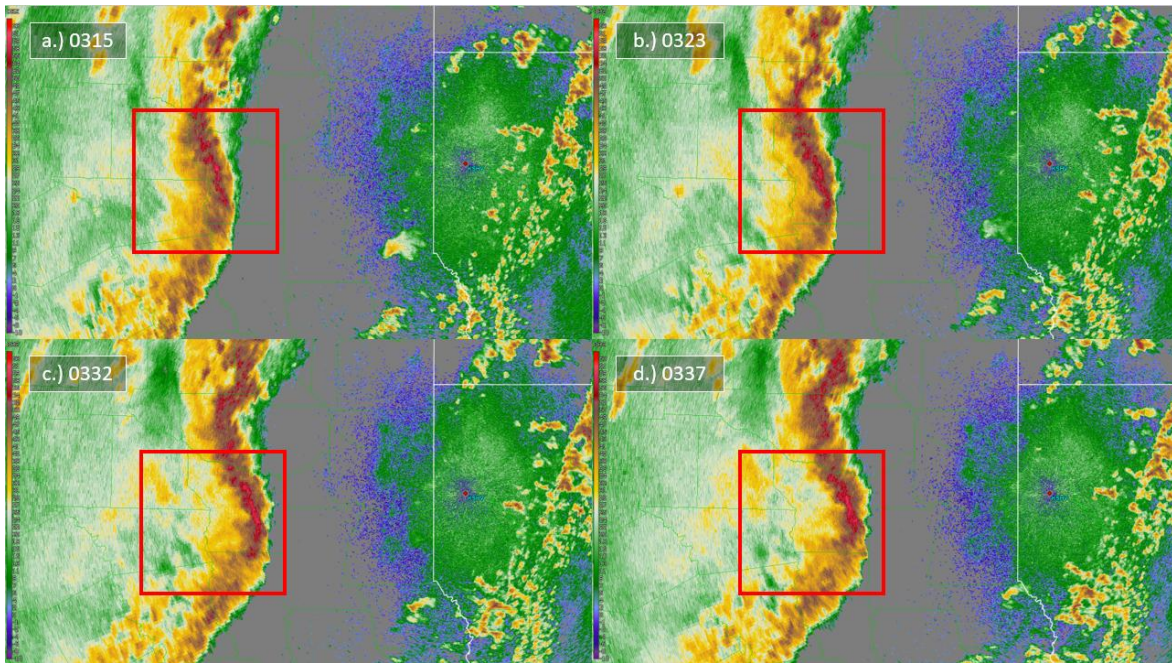


Figure 4.1: The squall line as it developed a bow-echo reflectivity pattern in Texas at the listed times, as observed by KSHV at the 0.5 deg tilt. The red box indicated the bow of interest, where mesovortices would become apparent over the next couple of hours.

gust front. Numerous trees were snapped and shingles were blown off of a church in Smith County, TX by this segment of the QLCS (National Centers for Environmental Information 2018). As the system continued to propagate across East Texas between 0400 and 0430 UTC, the initial mesovortices associated with the bow-echo reflectivity pattern depicted in *Figure 4.3* began to decay. Between 0430 and 0440 UTC, a new mesovortex became apparent on the northern periphery of the decaying vortex. This new vortex (the southern circulation in *Figure 4.3*) intensified rapidly to tornadic strength, becoming tornado warned by 0450 UTC. As this mesovortex moved through the VORTEX-SE observational domain, it produced two tornadoes, the latter of which was the fatal, long-lasting EF-1, Shreveport-Bossier City, LA tornado.

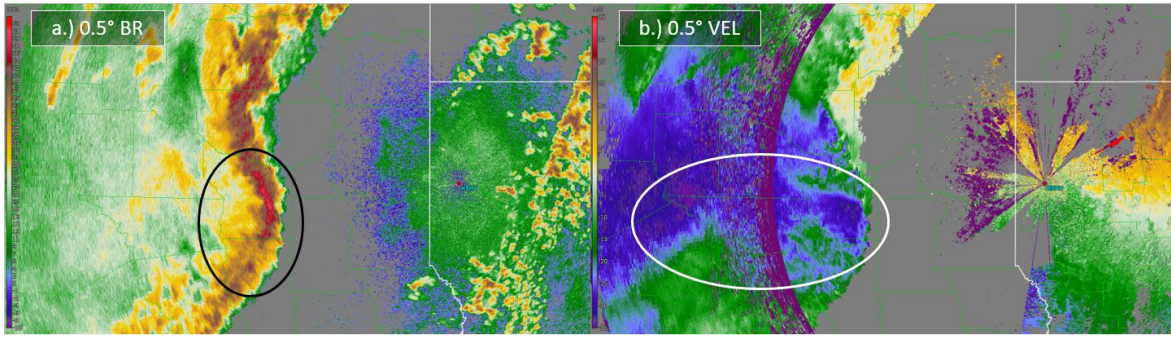


Figure 4.2: KSHV radar reflectivity (a) and radial velocity (b) at 0345 UTC. Note the strong flow (white oval) precipitating the bow-echo in the convective line (black oval).

This first tornado produced by this mesovortex began at 0450 UTC in rural Harrison County, TX (Lat/Lon: 32.3869° N/ 94.1053° W; National Centers for Environmental Information 2018), at the conclusion of an extensive development and intensification process. This process commenced thirty minutes (0420 UTC) before tornadogenesis occurred, as an intense rear-inflow jet (RIJ; Smull and Houze (1985, 1987); Weisman (1992); Skamarock et al. (1994)) became apparent to the west and southwest of the reflectivity bow (*Figure 4.4*). This RIJ intensification occurred as the initial set of mesovortices associated with the bow echo decayed. A new mesoscale-gamma circulation had formed along the velocity surge at the low-to-middle levels of the complex, coincident with the tip of this inflow jet. Rotation was maximized at elevations between 1.3 and 1.8 deg, coupled to the RIJ feature and presenting just to the north of the decaying circulation.

As the jet continued to become established through a deep vertical layer at 0441 UTC, gate-to-gate shear intensified further to 21 m s^{-1} at 1000 m AGL (1.8 deg elevation). By 0443 UTC, intense rotation had begun to make its way to the surface, with 30 m s^{-1} inbound velocities appearing at the lowest elevation scan (0.5 deg, 300 - 375 m AGL). An elongated appendage perpendicular to the main convective line was apparent in the reflectivity field,

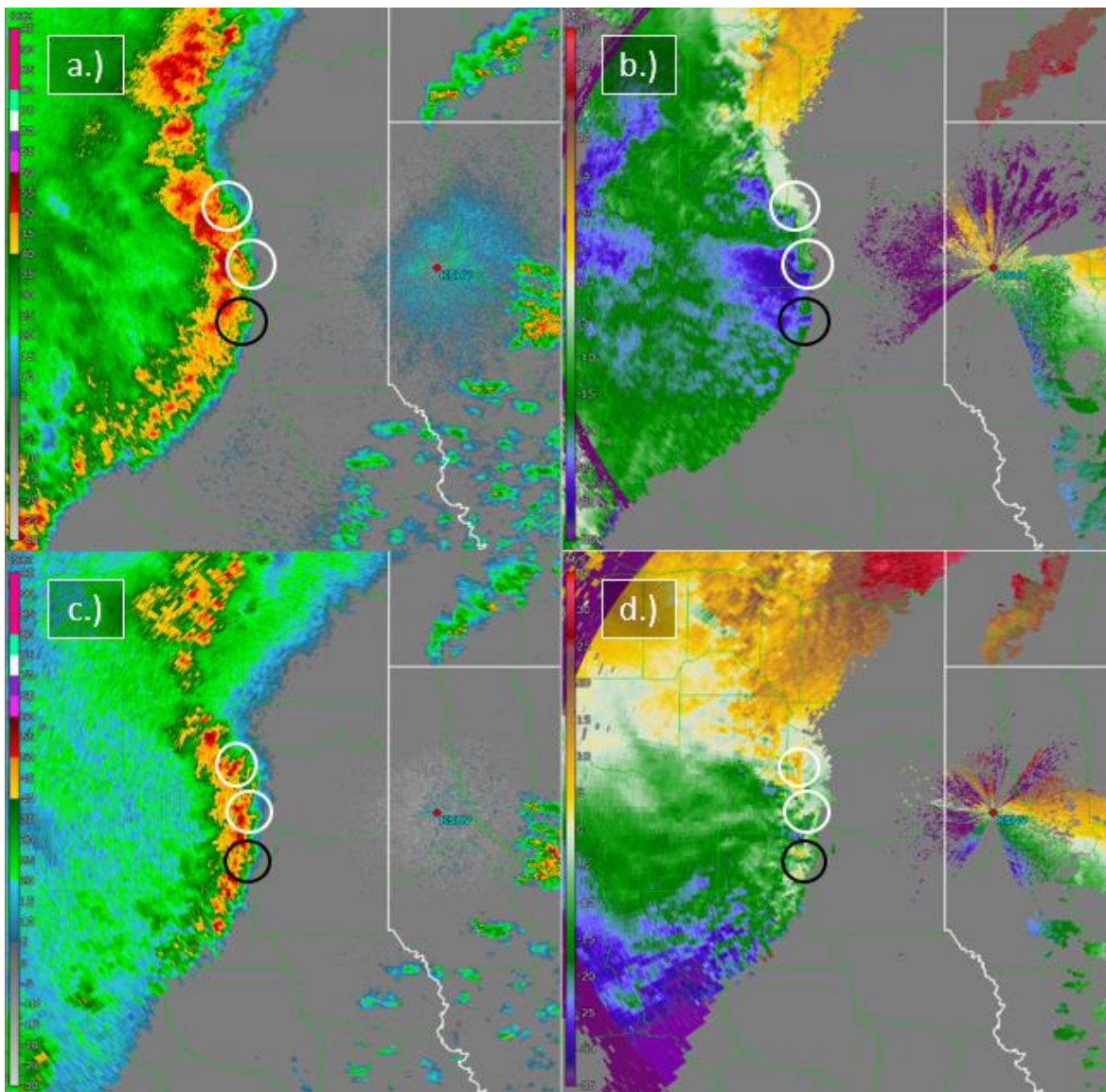


Figure 4.3: KSHV radar reflectivity (a) and (c), and radial velocity (b) and (d) at 0408 UTC. Note the vertical depth of the first and second mesovortices associated with the QLCS bowing segment. Images (a) and (b) are of the 0.8 deg tilt, and (c) and (d) are of the 2.4 deg tilt. The vortex associated with the Shreveport-Bossier City tornado is circled in black.

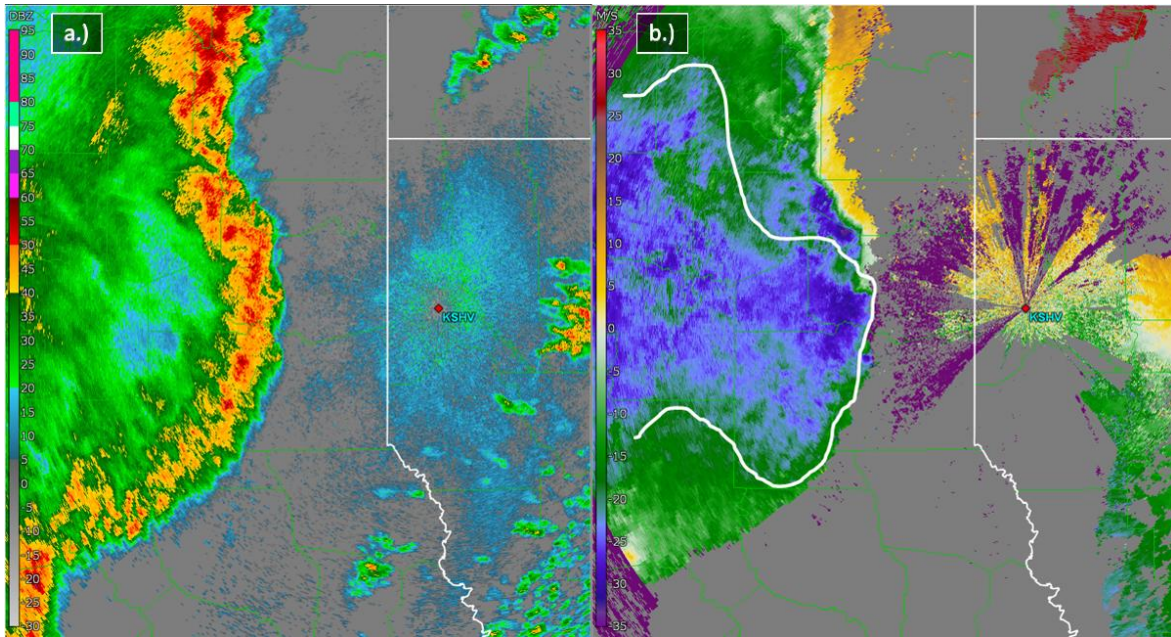


Figure 4.4: KSHV 0.5 deg radar reflectivity (a) and radial velocity (b) at 0420 UTC depicting the intense inbound velocities associated with the QLCS's RIJ. The periphery of the jet is highlighted in white for clarity.

indicating that a localized updraft likely had formed near the main updraft zone of the convective band.

By 0447 UTC, the circulation attained yet higher intensity at low-levels and began to tighten considerably, leading to the issuance of a tornado warning approximately seven minutes later. *Figure 4.5* depicts this intensification at the lowest elevation just prior to tornadogenesis. Additionally, SMART-R1 data (*Figure 4.6*) shows a burst of enhanced reflectivity to the west of the vortex between 0447 and 0449 UTC. Reflectivity values increased from 50 dBZ to more than 55 dBZ during this two-minute period. By 0454 UTC, the reflectivity burst observed at low elevations had subsided, as values fell below 50 dBZ near the circulation and the enhanced reflectivity was displaced northward in the storm-relative flow (not shown). Rapid increases in radar reflectivity at successively lower levels are typically associated with downdrafts (Isaminger 1988; Wakimoto and Bringi 1988; Newman and Heinselman 2012; Kuster et al. 2016); this type of enhancement occurred within the vortex region at this time. Divergence from this downburst likely contributed to a small-scale local enhancement of rear inflow that acted as a focus for low-level convergence in the vortex region at the time of tornadogenesis.

At tornadogenesis (0450 UTC) the RIJ was still strong at low-levels (600 m - 1200 m AGL), but had become less discernible above two kilometers. Prior to tornadogenesis, there was a distinct separation between the mesovortex and the RIJ axis (*Figure 4.5*). At later times, the circulation was aligned more downwind of the axis of the RIJ (*Figure 4.7*). The juxtaposition of these two features suggests that the RIJ was important to the maintenance of the mesovortex, especially at low levels. Indeed, as the RIJ decreased in magnitude between 0456 and 0501 UTC, the tornado also weakened and dissipated.

As the complex advanced further east, the RIJ feature strengthened significantly once again, with inbound velocities between 700 and 1800 m exceeding speeds of 30 m s^{-1} and impinging along the leading edge of the convective line (*Figure 4.8*). The reflectivity field

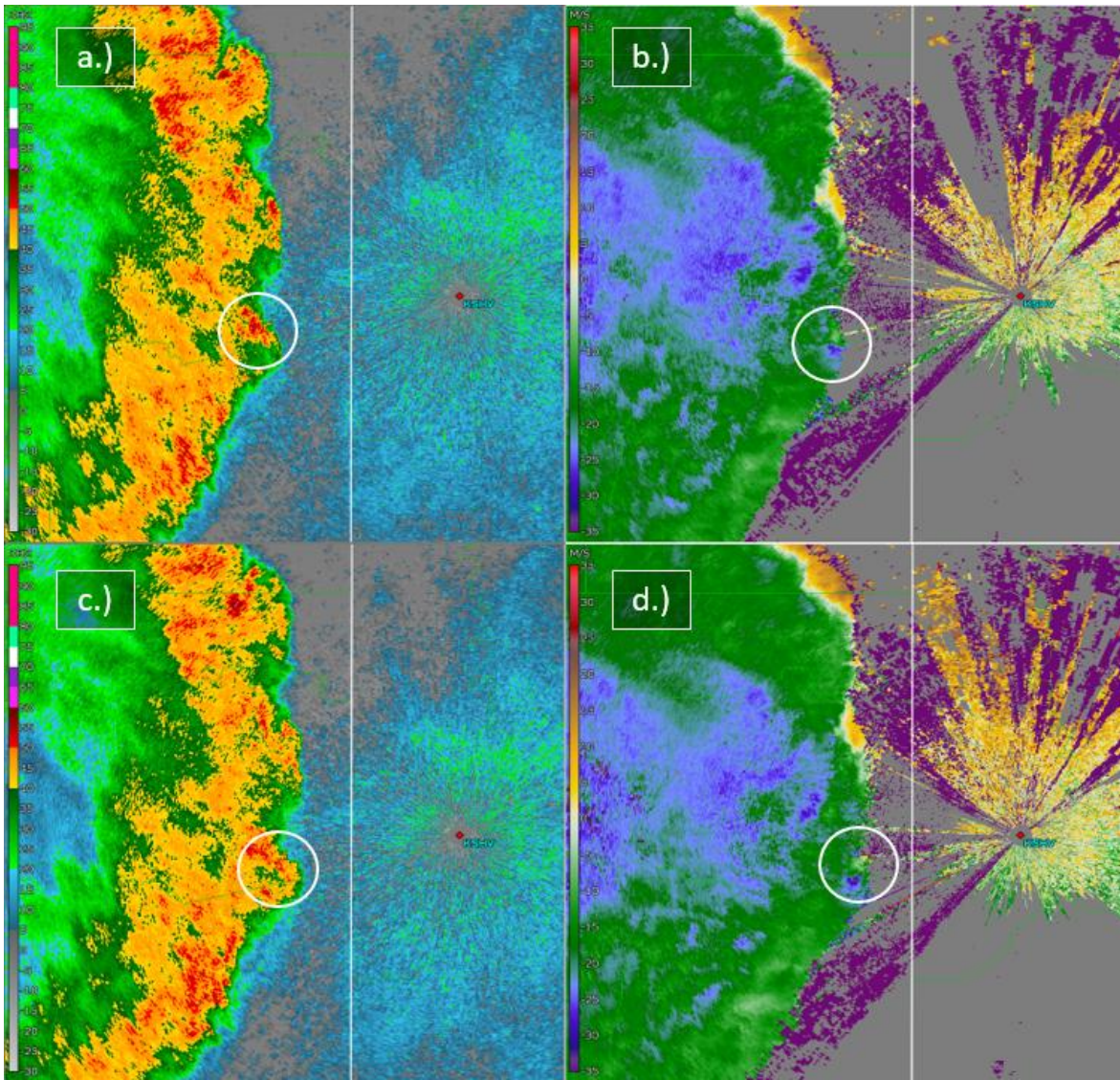


Figure 4.5: The intensifying mesovortex as viewed from KSHV at the 0.5 deg elevation angle PPI sweep between 0443 and 0447 UTC. Images (a) and (b) depict radar reflectivity and radial velocity, respectively, at 0443 UTC. Images (c) and (d) depict radar reflectivity and radial velocity, respectively at 0446 UTC. Note the increase in inbound velocities on the south side of the vortex between images (c) and (d).

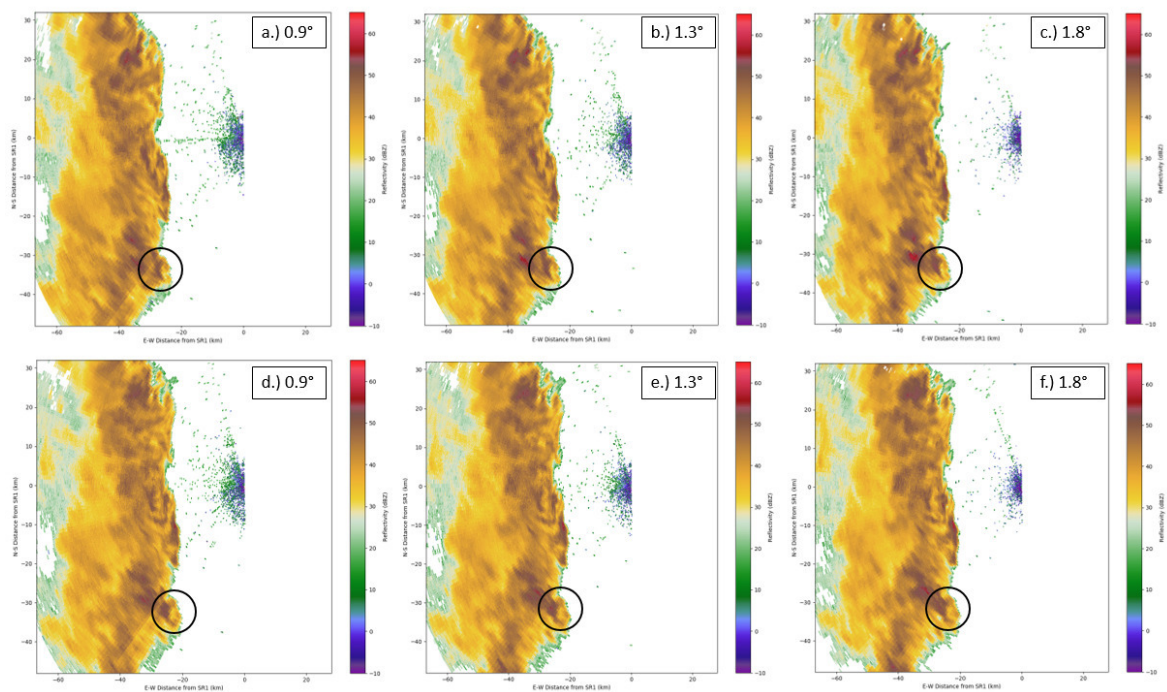


Figure 4.6: Evolution of SMART-R1 radar reflectivity from 0447 (top row) to 0449 UTC (bottom row). The black circle represents the location of the mesovortex.

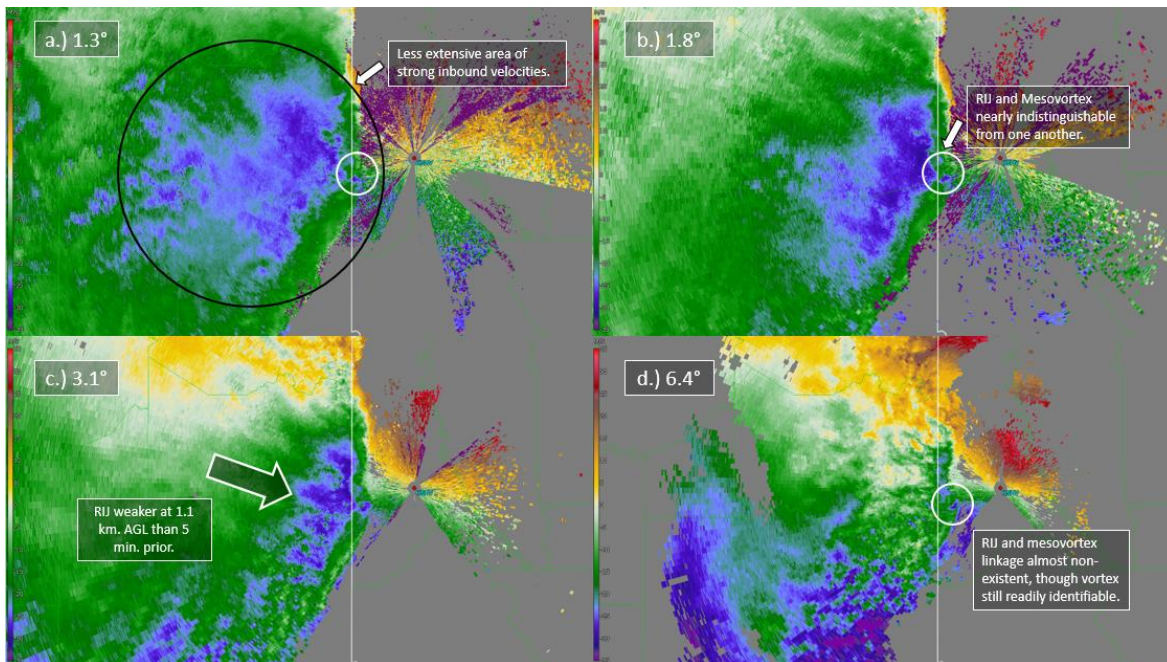


Figure 4.7: The appearance of the RIJ at various heights as viewed by KSHV between 0456 and 0459 UTC. The mesovortex location is circled in white. (a) The circulation at about 450 m altitude; (b) same as in (a) but for 580 m; in (c) same as in (a) but for 900 m; and (d) same as (a) but for 1.7 km. Note the reduction of the RIJ strength with altitude, and the continuing presence of the vortex.

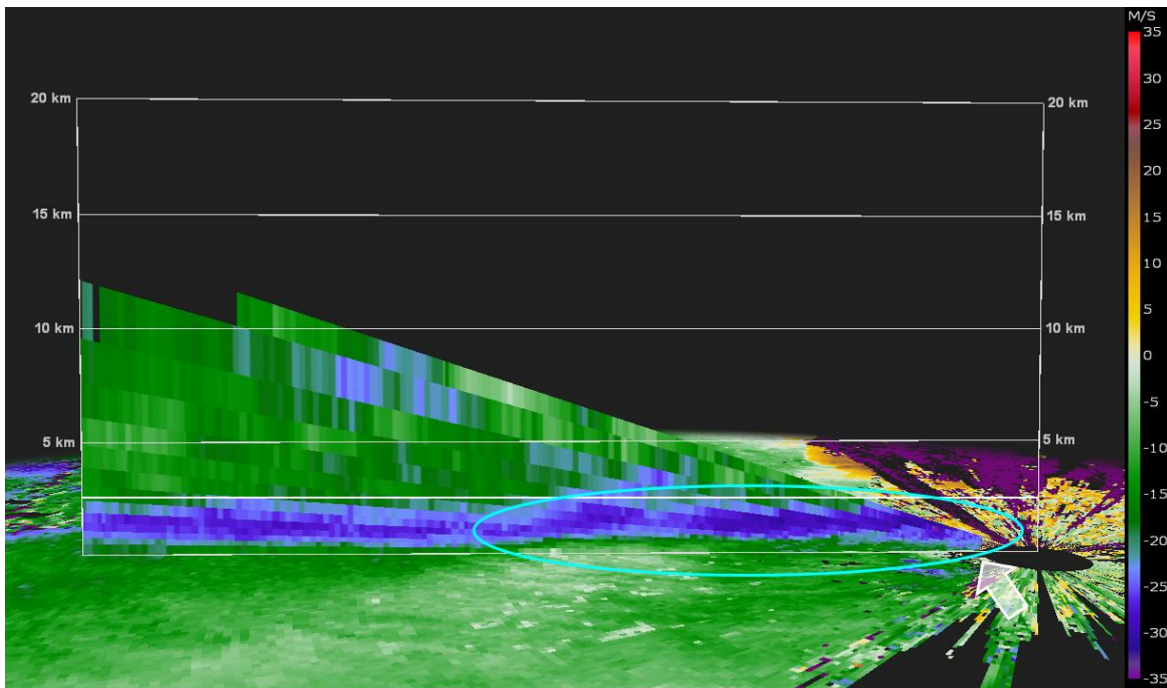


Figure 4.8: A cross-section of the KSHV radial velocity taken perpendicular to the convective line at 0507 UTC as the circulation moved into the cone of silence region. Note the presence of the intense RIJ (circled in cyan) and its proximity to the mesovortex (given by the white arrow).

began to protrude in the lowest levels once again (*Figure 4.9*). A new, near-surface level circulation associated with the previously noted mesovortex developed just to the north of the surface circulation associated with the previous tornado. Gate-to-gate shear continued to increase as the newly-formed circulation moved into the cone of silence for KSHV.

By the time the vortex emerged from the cone of silence of KSHV at 0514 UTC, it had intensified greatly and had been producing a second, more intense tornado for roughly three minutes (National Centers for Environmental Information 2018). Observed velocities from KSHV were at least 40 m s^{-1} at 50 m AGL in the southern branch of the circulation, indicated by the receding radial velocity in *Figure 4.10*. Intense, cyclonic winds were occurring at nearly ground level. Additionally, 43.5 m s^{-1} gate-to-gate shear (39.5 m s^{-1} outbounds,

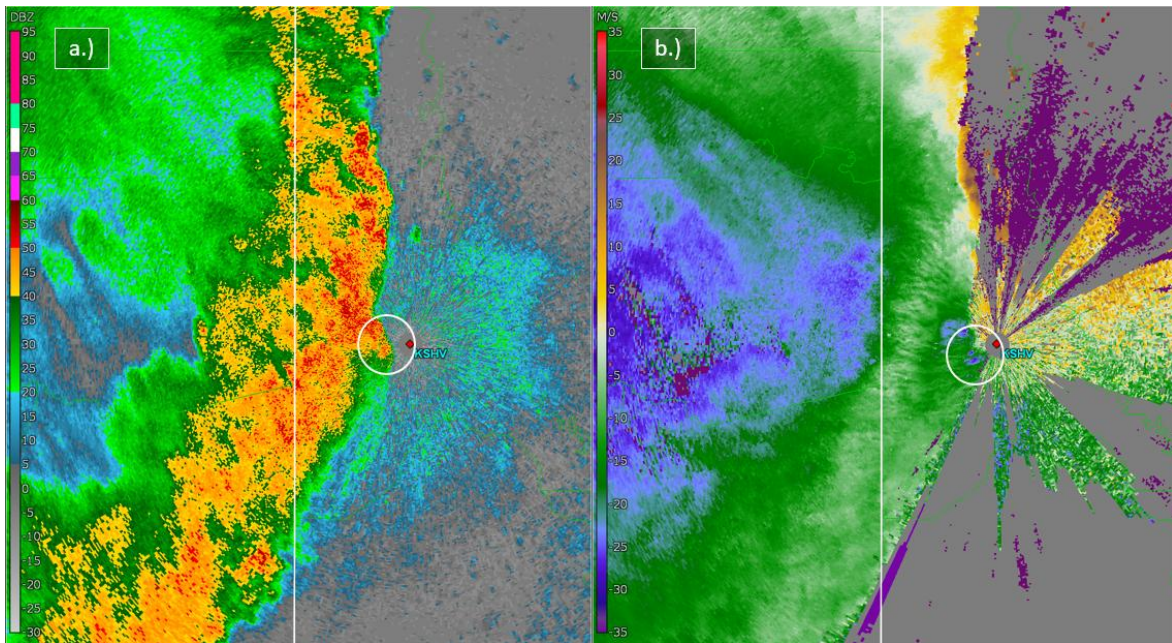


Figure 4.9: Mesovortex region 0.8deg radar reflectivity and radial velocity, as viewed by KSHV at 0508 UTC. The echo appendage and rotation signature in the velocity field is highlighted with white circles.

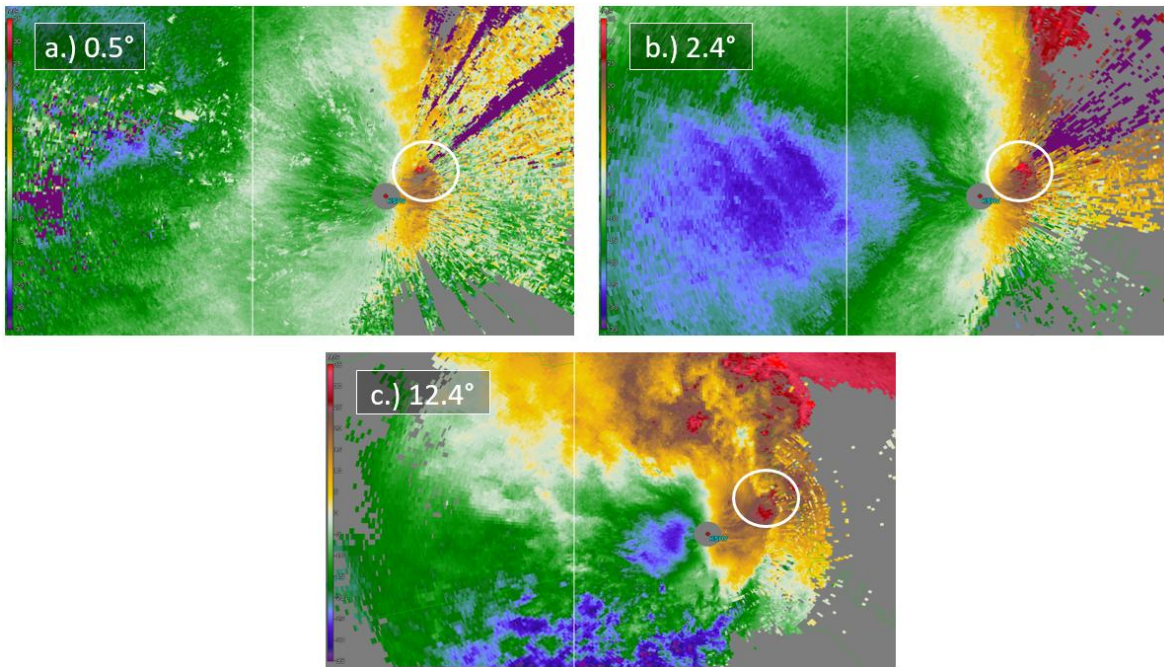


Figure 4.10: The mesovortex region (white circles) as the tornadic circulation emerged from the KSHV cone of silence at 0517 UTC. The height of the vortex is 50 m in (a), 300 m in (b), and 2.2 km in (c).

-4 m s^{-1} inbounds) was observed at 300 m, illustrating that there was vertical continuity between rotation observed near the surface and rotation observed further aloft. Though the circulation weakened with height, cyclonic rotation was still discernible until just above 3 km AGL. The RIJ was still notable as well, as a broad region of greater than 25 m s^{-1} inbound velocities streamed into the region just behind the main convective line, between 700 m and 2.5 km altitude (*Figure 4.11*).

In contrast to the large degree of interaction between the RIJ and mesovortices that was observed earlier, the RIJ and now tornadic second main mesovortex had become decoupled from one another. Previously, as the intense bound velocities associated with the RIJ approached the main convective line and induced the formation of the bow echo they also interacted with the initial mesovortex circulation, wrapping around the mesovortex from the

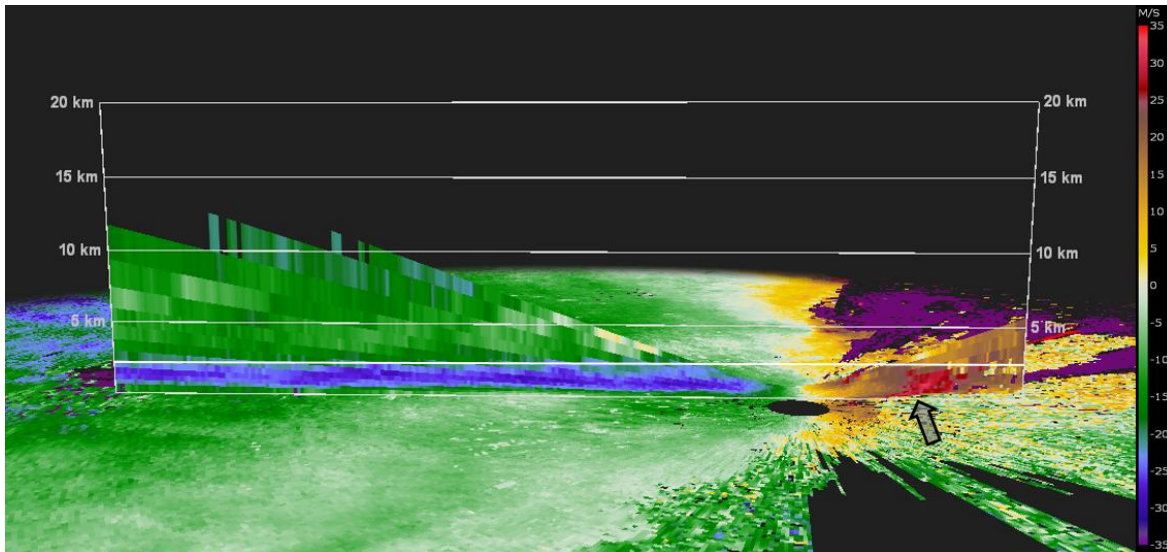


Figure 4.11: A cross-section of radial velocity taken perpendicular to the convective complex at 0517 UTC, as viewed from KSHV. The mesovortex is highlighted by the black arrow. Note the prevalent 30 m s^{-1} velocity returns associated with the RIJ.

south and southeast between 450 m and 1.5 km AGL. Moreover, the convergence along the leading edge of the RIJ likely aided in concentrating vertical vorticity to tornadic levels in the first tornado. However, as the bow matured, separation between the outbound velocities associated with the vortex circulation and the RIJ became apparent at these levels. A large, vertically continuous area of greater than 30 m s^{-1} velocities was noted within the vortex at this time, as intensity continued to peak. But this rear-to-front flow was ahead of the RIJ leading edge by approximately 6 kilometers. The severance of this mesovortex/RIJ linkage is also corroborated in the SMART-R1 data, as an area of intense outbound velocity was present on the southeast and eastern portions of the vortex around 1.4 km AGL, but was disconnected from the rear inflow (not shown).

As the vortex and associated tornado traveled northeastward, both SMART-R1 and KSHV radial velocity data continued to observe an intense, compact circulation at low levels. Gate-to-gate shear was estimated to be 49.5 m s^{-1} at 100 m at 0521 UTC. This rotational signature

remained intense with increasing height, with the strongest velocity values observed at 500 m. The vortex also had considerable vertical extent at this time, as cyclonic shear was detectable through 4 km AGL in both radars' velocity fields. This pattern of intense rotation near the surface and downwind from the RIJ axis continued through the next ten minutes.

At 0535 UTC, the circulation was weaker, especially above 1.5 km AGL. Velocity returns at these heights decreased from greater than 30 m s^{-1} at 0520 UTC to $20\text{-}25 \text{ m s}^{-1}$. As was the case with the first tornadic circulation, the magnitude of the RIJ at low levels weakened as the tornado dissipated (*Figure 4.12*). The once prevalent $25\text{-}30 \text{ m s}^{-1}$ outbound velocities wrapping around the southern portion of the mesovortex retreated well over the cold pool of the QLCS (*Figure 4.13*). Rotation at the lowest elevation angle (0.5 deg, 200 - 400 m AGL) weakened rapidly as the storm-relative RIJ retreated; the circulation aloft weakened more slowly.

By 0541 UTC, the circulation near the surface had broadened considerably and the tornado dissipated (*Figure 4.12*). Rotation above the surface (400 m - 2.0 km; 0.5 - 2.4 deg tilts) appeared to reach a state of stasis, with considerable gate-to-gate shear still present. Though strong shear was still evident between 400 m and 2.0 km, the RIJ had continued to separate from the vortex, and the strongest velocity returns associated with the RIJ were now located over the cold pool, removed from the vortex by a considerable distance.

By 0555 UTC there was little cyclonic shear observed and the residual circulation appeared broad in character (*Figure 4.14*). The RIJ had reached its weakest point in its lifecycle, with only sporadic areas depicting flow greater than 25 m s^{-1} well to south and southwest of the remnant vortex. The mesovortex later moved out of the Shreveport-Bossier City region while a new, stronger mesovortex formed to the north. This tertiary vortex would go on to produce another EF-1 tornado, but study of this circulation is outside the scope of this particular analysis.

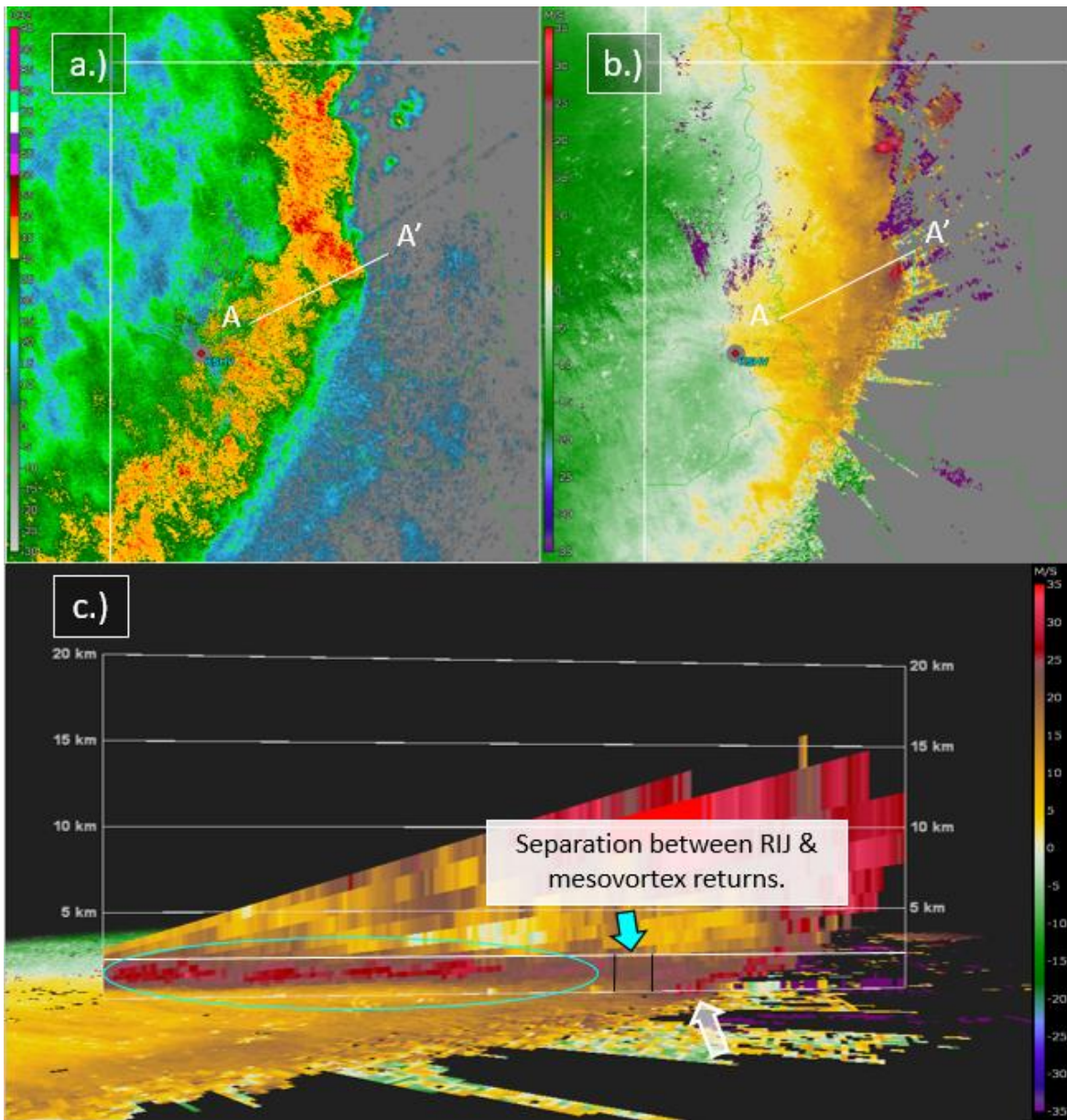


Figure 4.12: Radar reflectivity (a) and radial velocity (b) in the 0.5 deg elevation sweep from KSHV at 0541 UTC. The A to A' line is the approximate location of the cross section of radial velocity depicted in (c). In (c) the location of the vortex is highlighted by the white arrow, and the RIJ is circled in cyan. Note the weaker appearance of the mesovortex, and the separation of the RIJ and vortex.

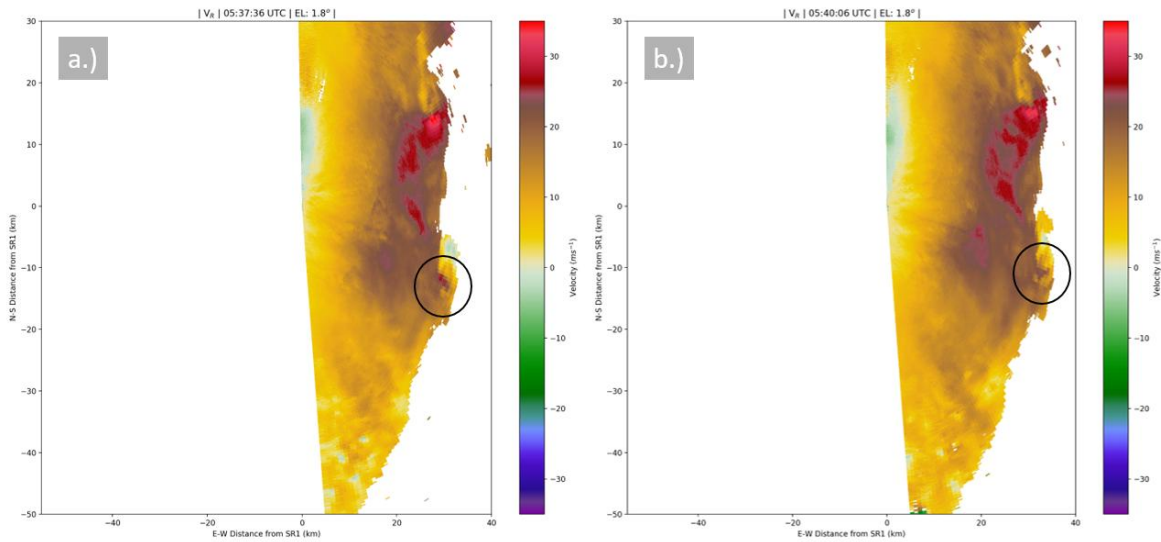


Figure 4.13: Radial velocity from SMART-R1 showing the weakening of both the rear inflow and mesovortex at (a) 0537 UTC, and (b) 0540 UTC by SMART-R1. The vortex of interest is circled in black.

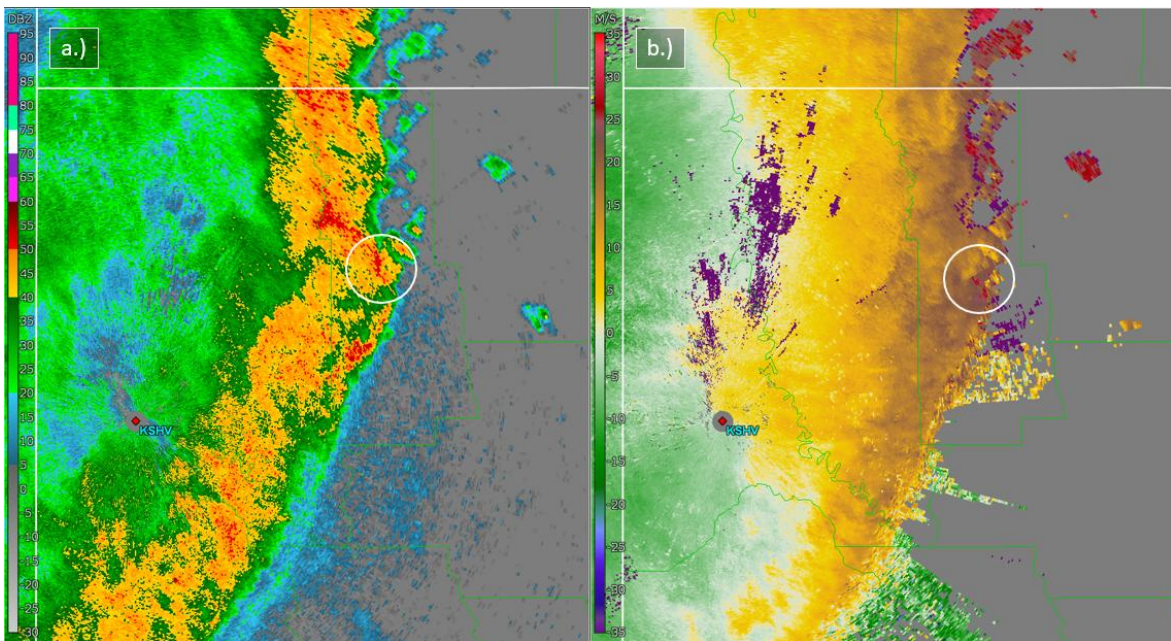


Figure 4.14: KSHV 0.5 deg radar reflectivity (a) and radial velocity (b) at 0555 UTC.

4.2 Mesovortex #2

Similar to Mesovortex #1, the initiation of the second main mesovortex was closely tied with an increase in strength of the RIJ. Between 0445 and 0501 UTC, the inbound SMART-R1 radial velocities continuously showed inbound velocities associated with the RIJ at the 1.3 deg elevation. A wide swath of 30-35 $m s^{-1}$ flow was noted behind the rapidly developing vortex region (*Figure 4.15*). This intensification created an increasingly northwest-southeast oriented convective line segment at the front of the complex as the gust front surged ahead, creating a bow-echo structure. Furthermore, a substantial increase in the area covered by the RIJ was noted, growing 20 to 30 km in north-south extent, and 15 to 20 km in east-west extent.

By 0504 UTC, three separate regions of cyclonic shear had formed downwind of the RIJ axis along the outflow boundary (*Figure 4.16*). The center-most shear zone had locally enhanced areas of rear-to-front flow that extended from the center of the bow echo to the mesoscale RIJ (*Figure 4.17*). These localized pockets of rear inflow were associated with individual convective features. Therefore, the rear-to-front flow feeding into the southern branch of the central, developing mesovortex had contributions from both the mesoscale and convectively-driven outflows. The combined effects of these outflows enhanced rear inflow through a deep layer and enhanced convergence along the leading edge of the convective line.

Similar to the first mesovortex, the enhanced convergence associated with the rear-to-front flows was augmented at low levels by outflow from a nearby convective cell. Prior to mesovortex genesis, the radar reflectivity 1 to 3 km west of the three cyclonic shear zones was comparatively lower than in surrounding regions (*Figure 4.18a*). By 0509 UTC, a reflectivity burst became apparent (*Figure 4.18c*). This burst occurred less than 1 km away from the center mesovortex and was characterized by reflectivity values of 55-60 dBZ. Outflow from

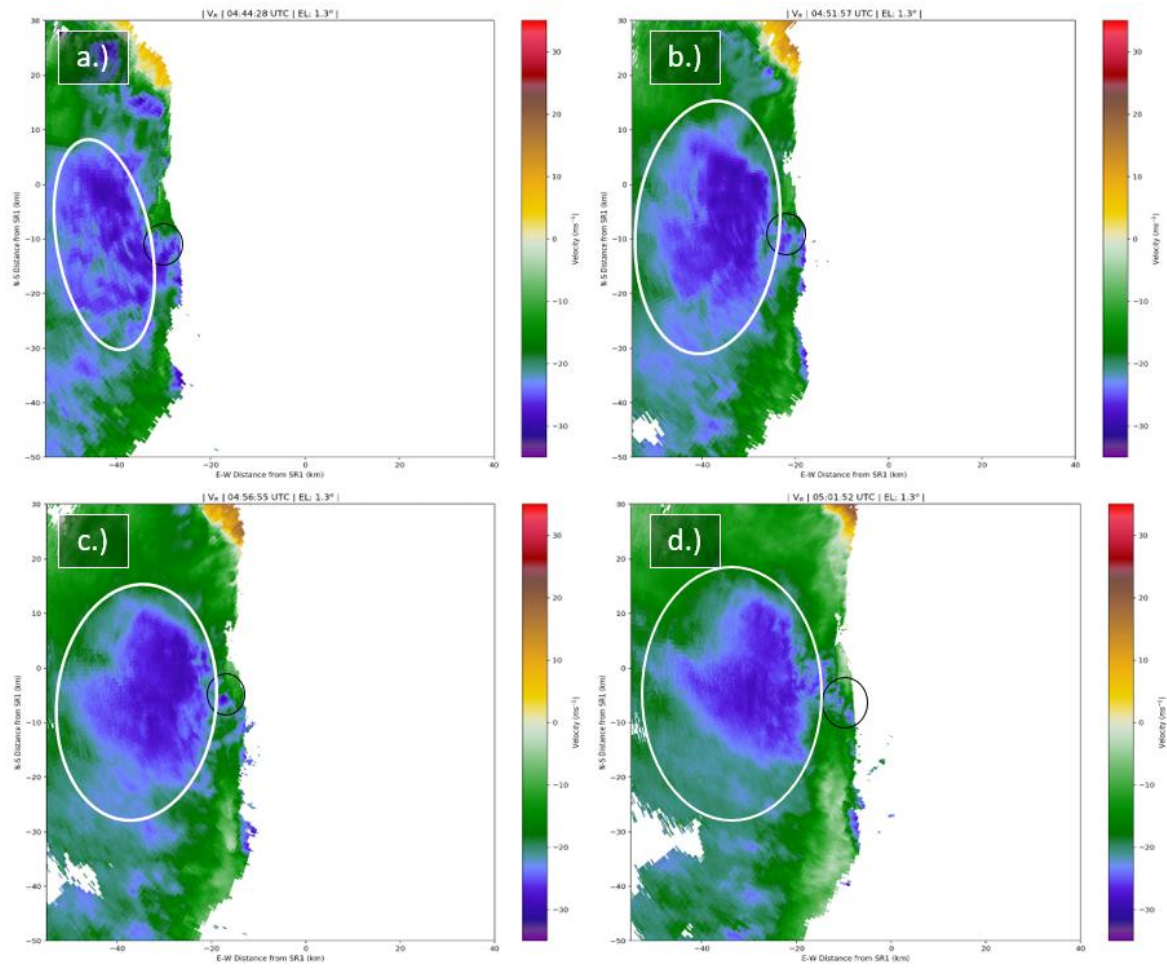


Figure 4.15: Radial velocity from the 1.3 deg elevation angle sweep from SMART-R1 at (a) 0444 UTC, (b) 0452 UTC, (c) 0456 UTC, and (d) 0502 UTC. The rear inflow is circled in white and the mesovortex region is circled in black.

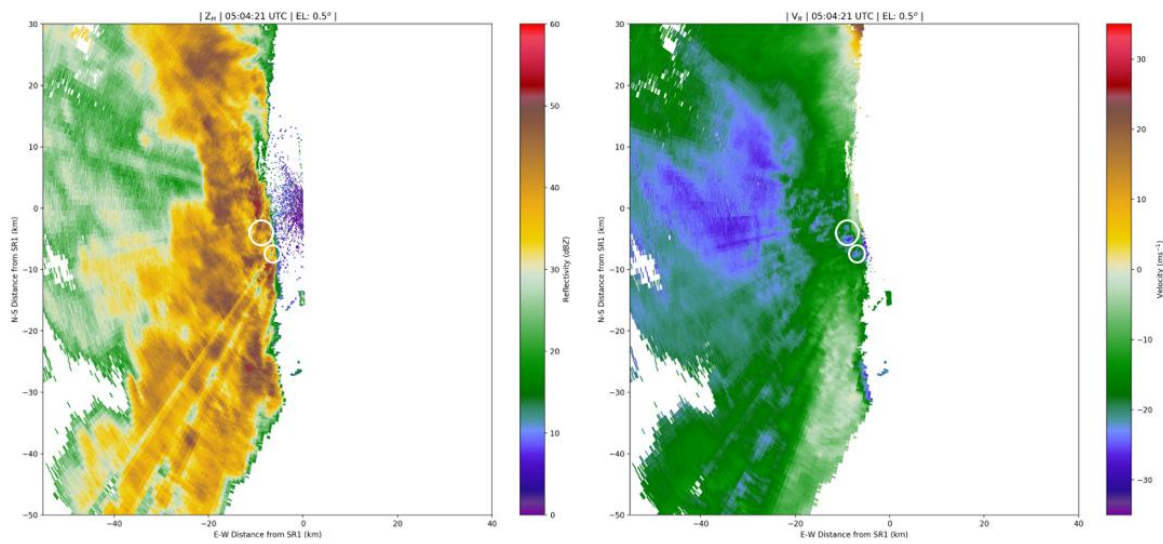


Figure 4.16: (a) Radar reflectivity and (b) radial velocity at 0504 UTC from the 0.5 deg elevation sweep from SR1. Circled areas denote cyclonic shear regions that formed along the line downwind of the RIJ axis. Note that the northern circle encompasses two shear features.

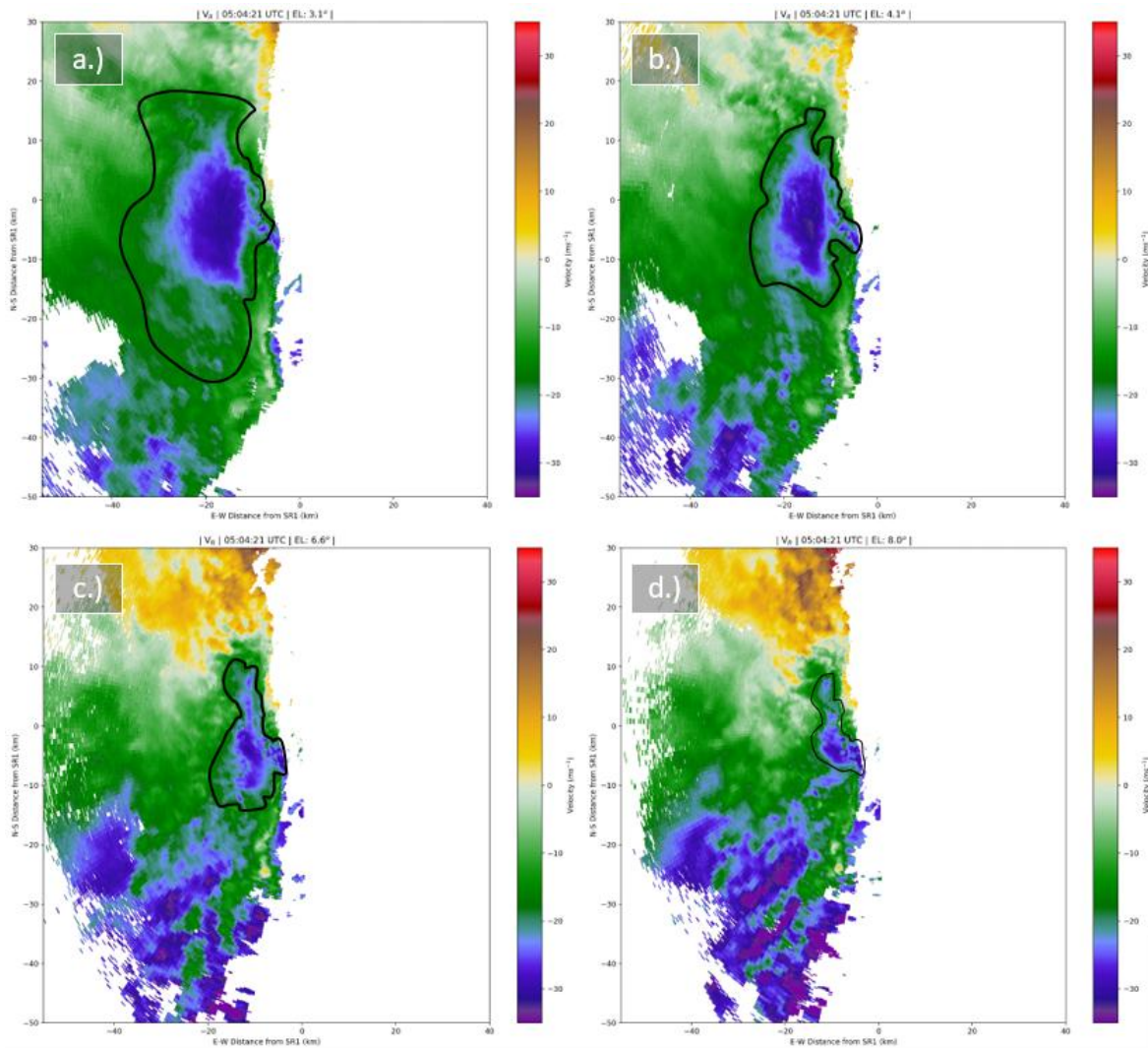


Figure 4.17: Radial velocity at (a) 3.1 deg, (b) 4.1 deg, (c) 6.6 deg, and (d) 8.0 deg elevation angles from the 0504 UTC SMART-R1 volume scan. The mesoscale and convective-scale regions of important rear-inflow are enclosed by the black outline.

this downburst aided in reinforcing the low-level convergence in the central shear zone and marked the beginning of a rapid-intensification stage of Mesovortex #2.

As the cyclonic shear zones passed over SMART-R1, the central feature developed into a strong mesovortex that absorbed the southern shear zone. By 0515 UTC, a single, intense circulation was noted just east of the radar (*Figure 4.19*). Calculated gate-to-gate shear was 23.6 m s^{-1} at the 0.8 deg elevation angle (53 m AGL), increasing to a maximum of 27.2 m s^{-1} in the 4.6 deg elevation scan. Above the 4.6 deg elevation, gate-to-gate shear decreased quickly. Despite the shallow nature of the most intense velocities, the cyclonic circulation associated with the mesovortex was apparent up to approximately 2 km AGL. Additionally, as observed during the early stages of Mesovortex #1, the new mesovortex was located downwind of the RIJ axis, reflecting the importance of the RIJ in both initiating the bowing of the gust front and concentrating the deep convergence that aided the intensification of vorticity over a deep layer. Indeed, the reflectivity bulge had become more pronounced by this time, likely driven by the RIJ-associated, flow-generated convergence maximum along the leading edge of the bow echo.

An inflow banding feature had also developed in elevations below 2.7 deg (*Figure 4.20b*), as suggested by a relative minimum in outbound velocities in a narrow swath just north of the mesovortex. Reduced reflectivity values, coincident with the strong inflow velocity signature, were also noted in this area (*Figure 4.20a*). Significant three-dimensionality in the reflectivity field was evident as the area to the northwest of the reflectivity minima exceeded 50 dBZ, while the area to the southwest exhibited strong curvature. In fact, the reflectivity structure in the area associated with the mesovortex at this time resembled a mini-supercell with its inflow notch, precipitation-laden rear flank, and attendant hook echo. It appears that the rotation associated with the mesovortex wrapped 45-55 dBZ reflectivity returns around the circulation at numerous elevations in the volume scan.

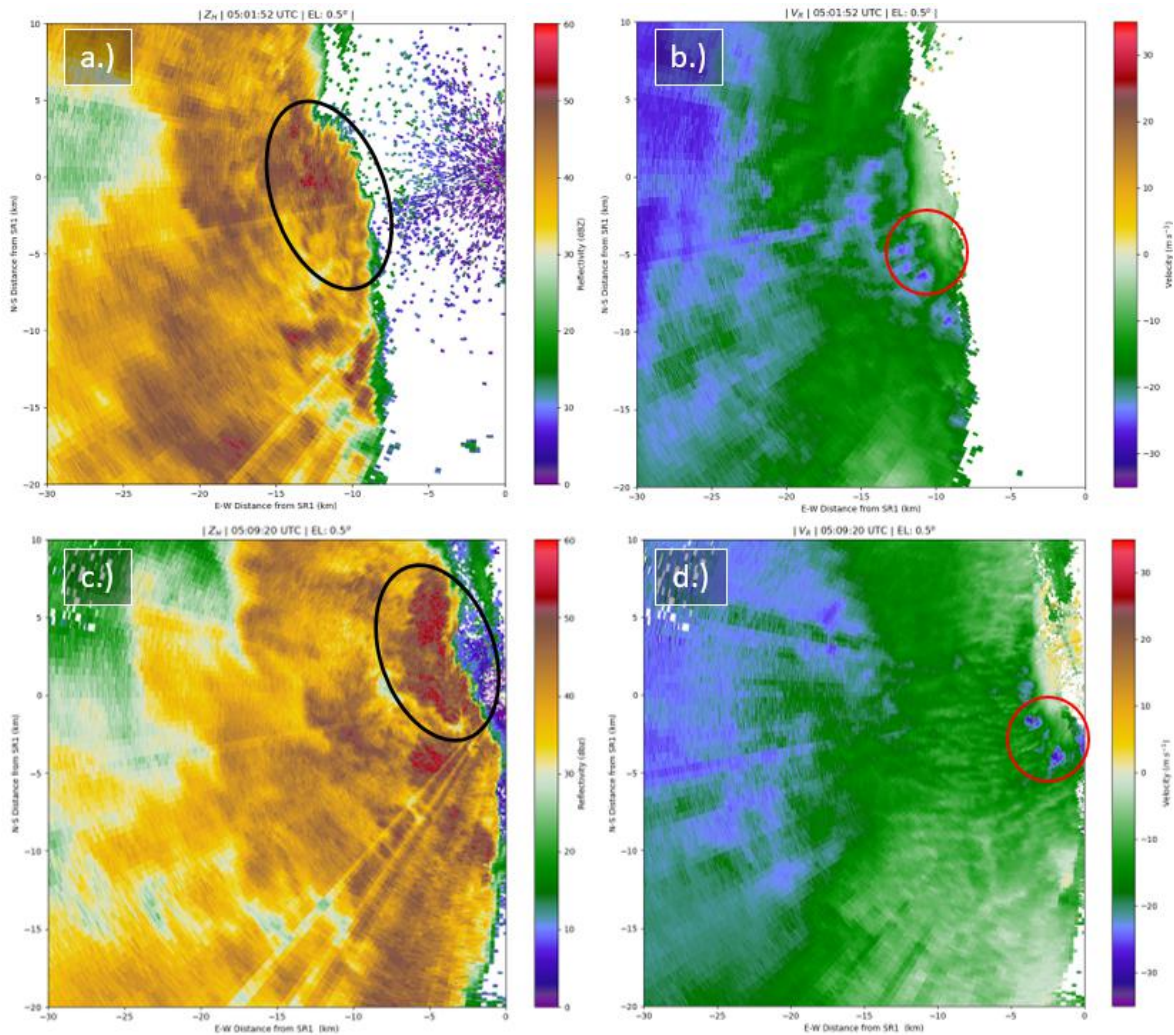


Figure 4.18: (a) Radar reflectivity and (b) radial velocity at 0.5 deg elevation from the 0501 volume taken by SMART-R1. (c) Radar reflectivity and (d) radial velocity at 0.5 deg elevation from the 0509 UTC volume scan taken by SMART-R1. Note the increase in radar reflectivity in the enclosed black curve just west of the cyclonic shear zones enclosed in the red circle.

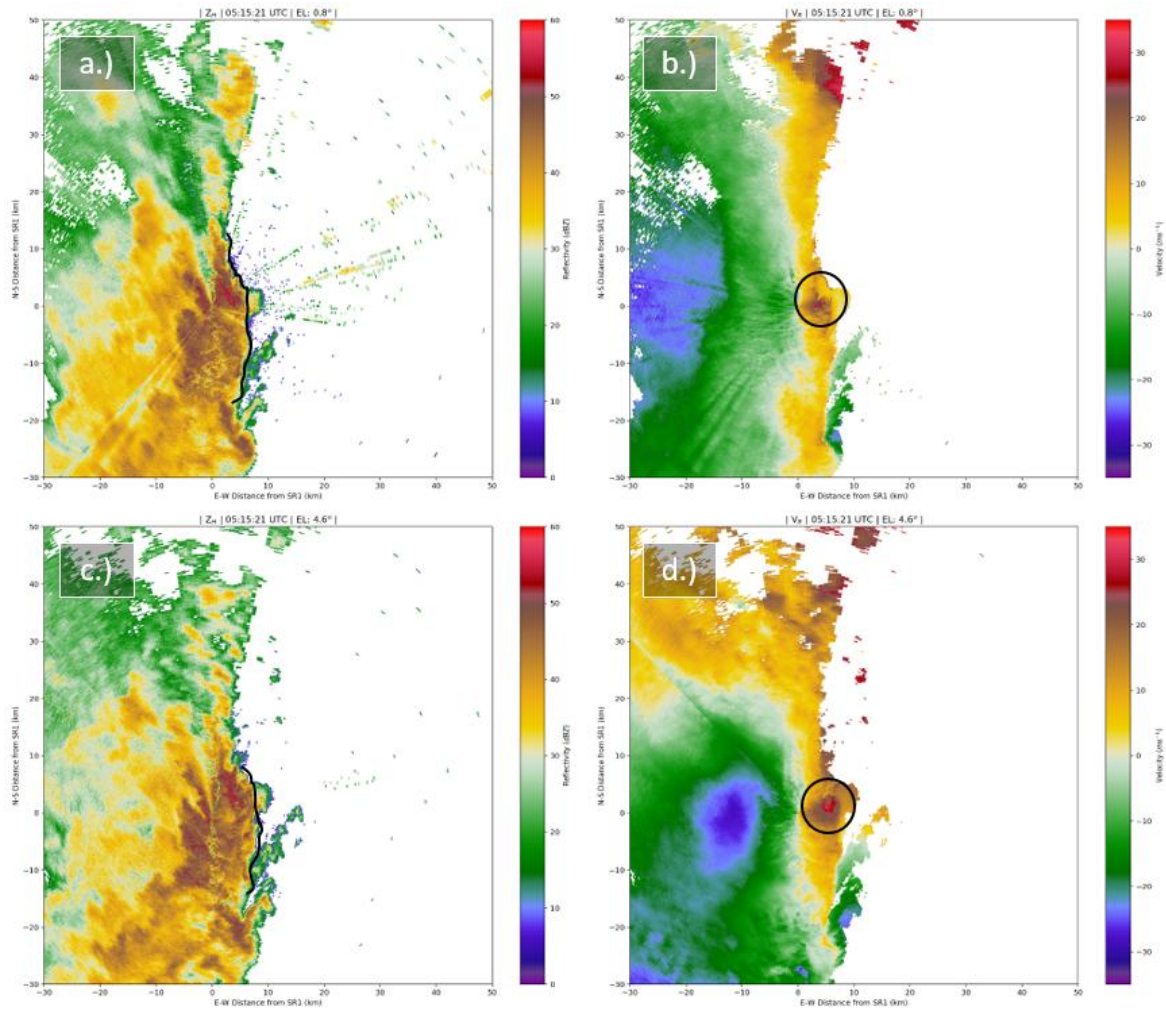


Figure 4.19: (a) Radar reflectivity and (b) radial velocity from the 0.8 deg elevation sweep taken with SMART-R1 at 0515 UTC. (c) Radar reflectivity and (d) radial velocity from the 4.6 deg elevation sweep taken with SMART-R1 at 0515 UTC. The black lines in (a) and (c) denote the gust front location along the bowed line segment. The black circles in (b) and (d) denote the location of mesovortex #2.

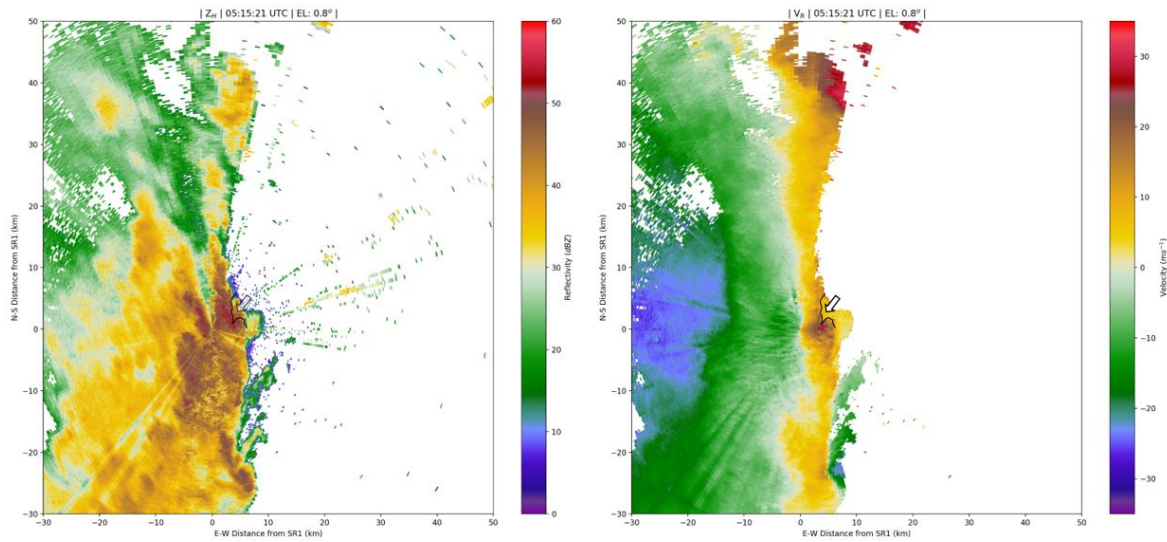


Figure 4.20: The environmental inflow notch feature at 0515 UTC, as observed by SMART-R1 at the 0.8 deg elevation.

At low levels, the circulation remained strong between 0515 and 0525 UTC. However, the circulation became less intense above 2 km AGL, with the velocity couplet becoming nearly indistinguishable from the ambient storm-relative wind flow near altitude (*Figure 4.21*). The juxtaposition between the RIJ axis and the mesovortex also changed during this period. Initially, the mesovortex was immediately downwind of the RIJ and in close proximity to the outbound velocity maxima in the SMART-R1 radial velocity field (*Figure 4.21b*) where it likely continued to be supported by deep convergence along the leading edge of the RIJ axis (*Figure 4.21d*). As the spatial distance increased, the circulation was likely able to benefit from the sustained convergence associated with the RIJ, which may explain why the circulation weakened aloft. Nevertheless, the reflectivity field around the circulation retained its miniature supercell-reminiscent structure.

Between 0528 and 0532 UTC, the circulation reached a relative minimum in intensity, as only a few radar gates displayed velocities of 35 m s^{-1} (not shown). The vortex was weakest in the lowest elevation scans, exhibiting little rotation at the 0.8 deg elevation. Shear did

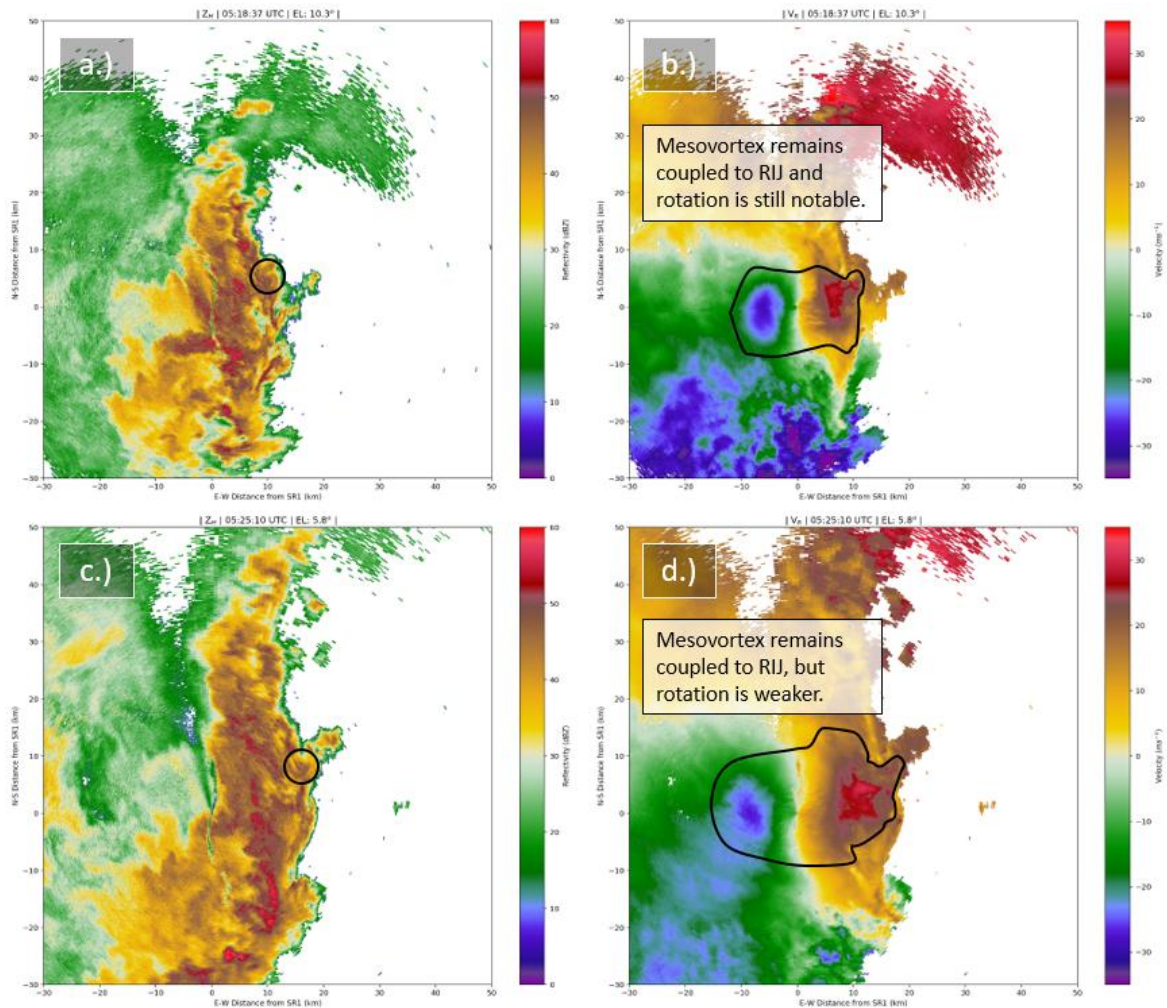


Figure 4.21: (a) Radar reflectivity and (b) radial velocity from the 10.3 deg elevation angle sweep taken by SMART-R1 at 0518 UTC. (c) Radar reflectivity and (d) radial velocity from the 5.8 deg elevation sweep taken by SMART-R1 at 0525 UTC. Regions of the mesovortex are circled in (a) and (c), while (b) and (d) have the ROI of interest highlighted by the black outline.

increase with growing elevation until reaching 3.5 deg (1.3 km AGL). After this elevation, the circulation became weaker once again, becoming indistinguishable from the background storm-relative flow by 10.3 deg (3.5 km AGL). Additionally, the areal extent of outbound velocities exceeding 25 m s^{-1} had also decreased considerably in size, causing the mesovortex to be much more compact in appearance.

Beginning at 0532 UTC, approximately 10 minutes prior to the Sarepta, LA tornadogenesis event, the mesovortex underwent a re-intensification process (*Figure 4.22*). Velocities at the 1.3 deg elevation ($\approx 560 \text{ m}$) began to exceed $25\text{-}30 \text{ m s}^{-1}$ for the first time since 0518 UTC, and the areal extent of heightened velocities surrounding the south and southwest portions of the vortex also increased considerably. Rear-to-front convective outflow reinforced the mesoscale RIJ, resulting in storm-relative rear-inflow wrapping around the southern and southwestern portions of the mesovortex, especially around 1.2 km as observed in the 3.1 deg elevation scan from SMART-R1 (*4.22c*) where the combined front-to-rear flow reached its greatest intensity. The mesovortex's rotation was greatest at the elevation just below that in which the rear-to-front maximum was observed. Above this elevation, the rotational signature weakened rapidly with height. Apparently, the convergence associated with the rear-to-front flow along the leading edge of the convective line intensified just prior to tornadogenesis and may have been responsible for increasing the mesovortex-associated rotation to tornadic levels at 1 km altitude.

Over the next eight minutes, the low-level rotation increased slightly just above the surface level (the 0.9 deg elevation scan; *Figure 4.23d*). Additional intensification was also noted up to 8.0 deg in elevation (3.5 km AGL). Within the reflectivity field, a bounded weak echo region (BWER) had become apparent. The combined rear-to-front flow reached a maximum at 0540 UTC, with numerous velocity gates exceeding 30 m s^{-1} at the 2.3 deg elevation (1.3 km AGL) (*Figure 4.24a*). A narrow band (around 3 to 4 gates wide; 111 to 148 m) of

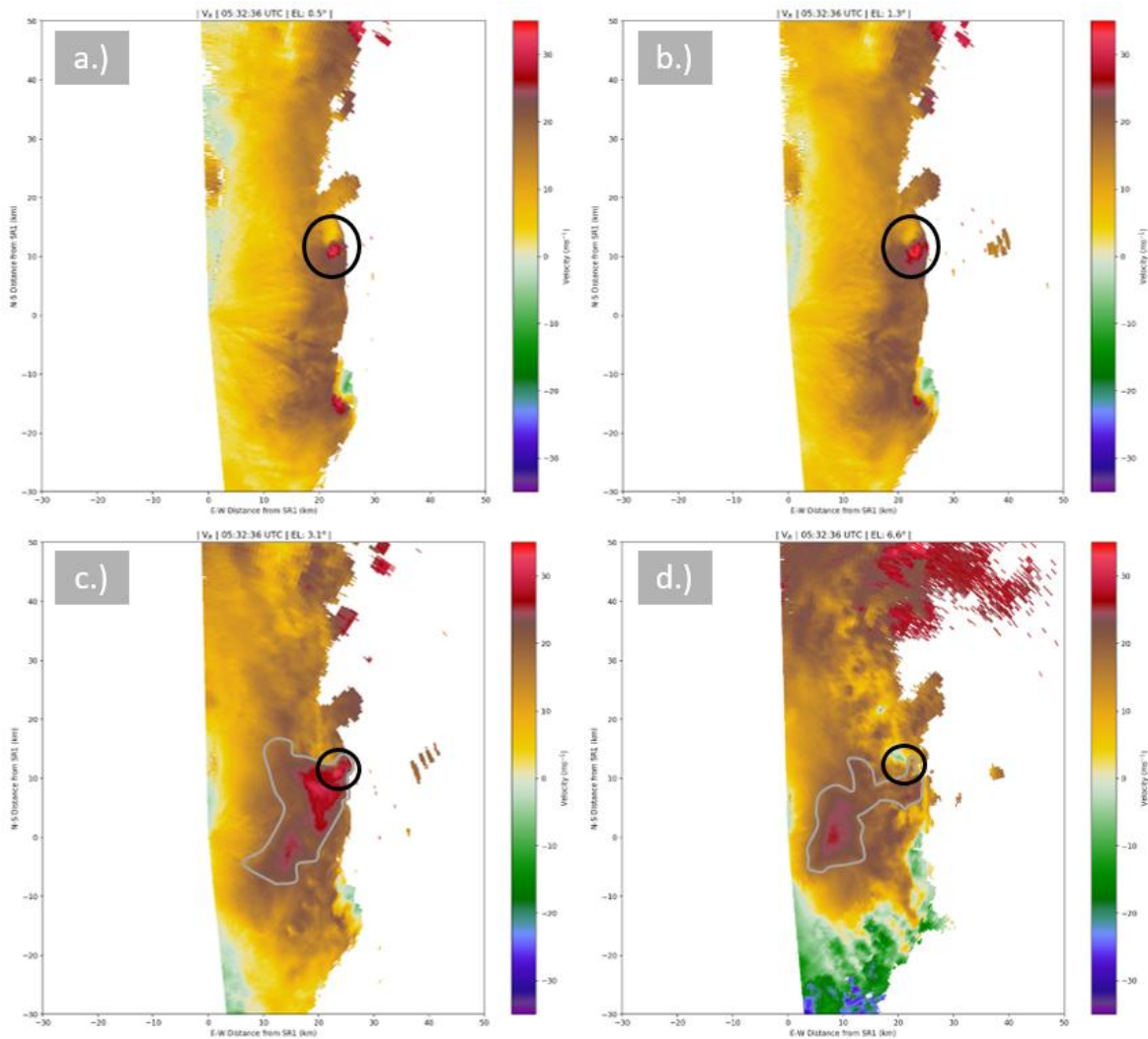


Figure 4.22: Radial velocity from the 0532 UTC volume scan taken by SMART-R1 at (a) 0.5, (b) 1.3, (c) 3.1, and (d) 6.6 deg elevations. The black circle denotes the mesovortex while the gray outline denotes the RIJ feature of interest.

intense outbound flow exceeding 30 m s^{-1} wrapped around the mesovortex region between 1 and 2 km AGL (2.3 - 4.1 deg elevations in *Figure 4.24*).

From 0542 to 0548 UTC, the mesovortex generated a short-lived EF0 tornado in rural areas of Claiborne Parish near Sarepta, LA (National Centers for Environmental Information 2018). Gate-to-gate shear at the time of tornadogenesis was highest just above the surface (0.9 deg elevation; *Figure 4.25a*), though velocities through the layer from 0.5 to 6.6 deg (250 m to 3.8 km) were stronger than 30 m s^{-1} . Intense rotation was observed in the lowest elevations of the volume, indicating that the circulation was strongest at and just above the surface. Nevertheless, the rotational couplet was notable through the lowest 4 km of the atmosphere. A large BWER was again observed, co-located with the area of maximum rotation (*Figure 4.26*).

Above the surface, the mesovortex remained coupled to the strong radial convergence associated with the combined convective and mesoscale rear-to-front flows through a deep layer of the atmosphere (1.3 to 4.1 deg; 730 m to 2.3 km). Rear-to-front flow exceeding $25\text{-}30 \text{ m s}^{-1}$ wrapped around the southern portion of the vortex (*Figure 4.25*). However, the juxtaposition between the tornadic vortex and the leading edge of the combined rear-to-front flows did not remain favorable for long. Just two minutes later (0545 UTC) the rear-to-front flow weakened, as the areal extent of velocities exceeding 25 m s^{-1} lessened between the 1.3 and 5.2 deg elevations. The mesovortex began to decouple from the convergence along the rear-to-front flows, especially at middle levels of the circulation (2.3 to 3.1 deg; 1.6 to 2.1 km AGL, *Figure 4.26b*). As viewed from 2.3 deg elevation, the rear inflow was separated from the outbound velocity of the vortex by around 1.5 km. The reflectivity field had also changed considerably, as 45-55 dBZ reflectivity returns now surrounded the western half of the circulation (*Figure 4.26a*). A BWER was still notable, but had become much broader and was less defined than it was in previous analysis times.

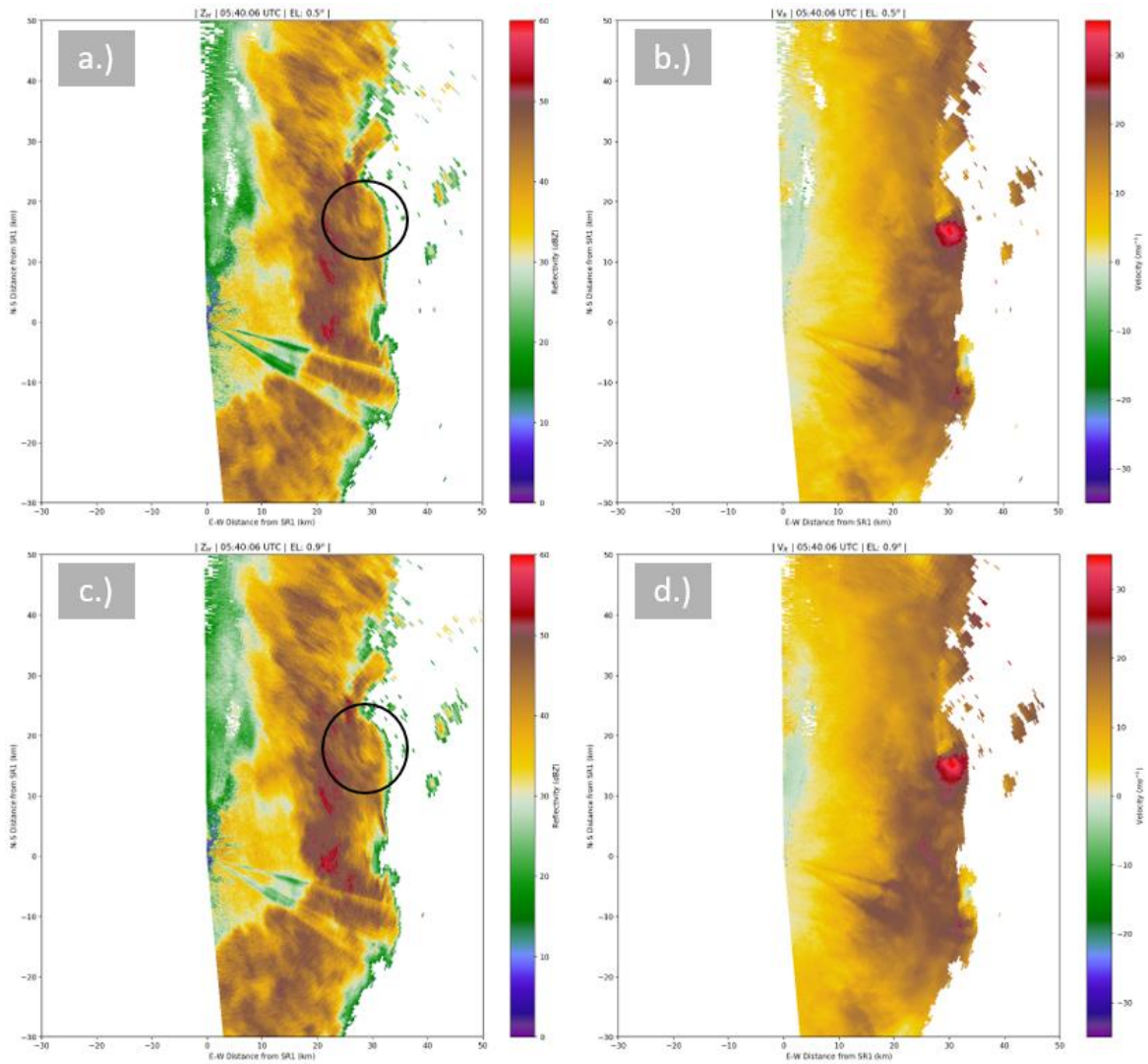


Figure 4.23: (a) Radar reflectivity and (b) radial velocity from SMART-R1 taken at 0.5 deg elevation from the 0540 UTC volume scan. (c) Radar reflectivity and (d) radial velocity from SMART-R1 taken at 0.9 deg in elevation from the 0540 UTC volume scan.

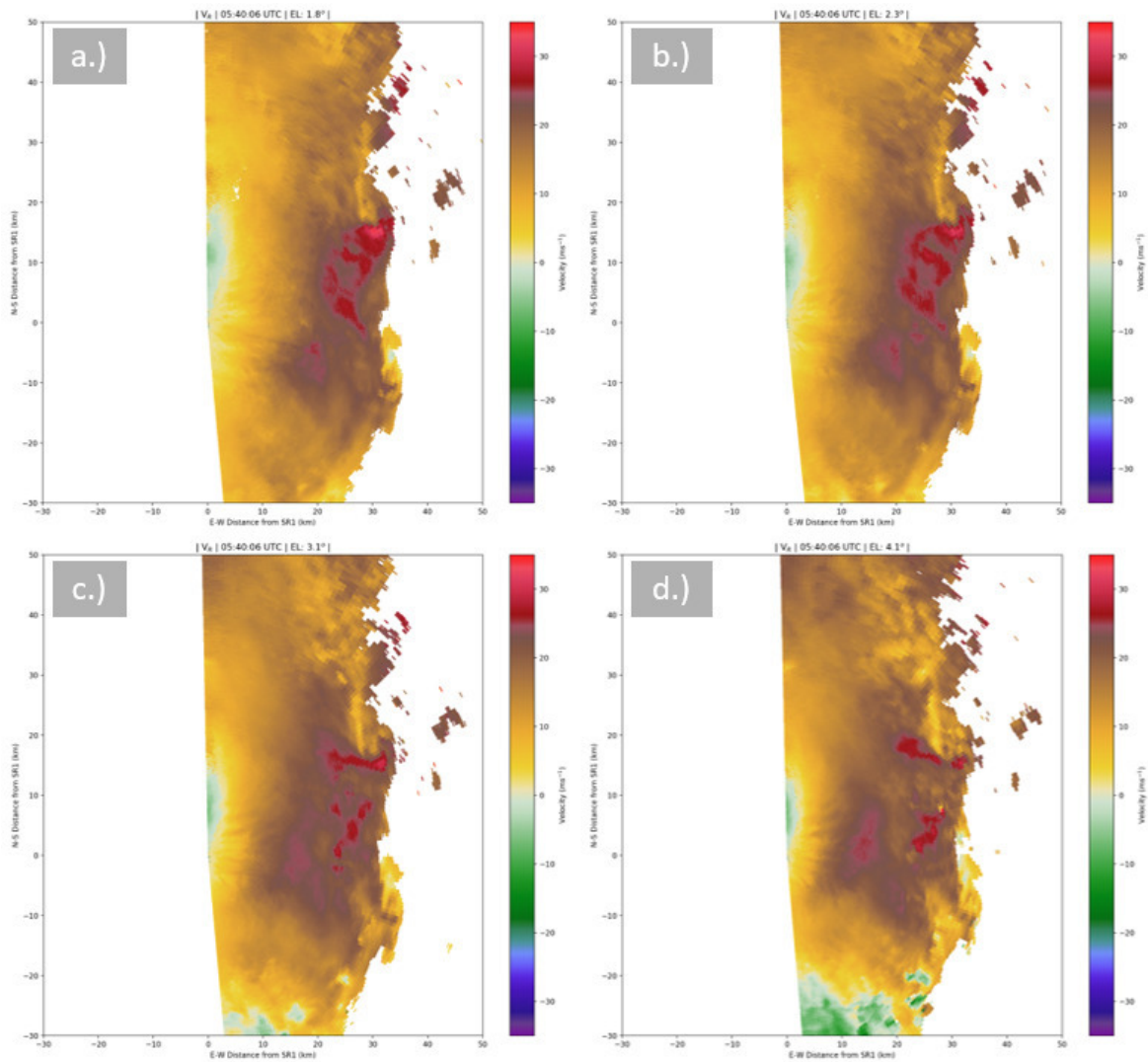


Figure 4.24: Radial velocity from the 0540 UTC volume scan taken with SMART-R1 at (a) 1.8 deg, (b) 2.3 deg, (c) 3.1 deg, and (d) 4.1 deg.

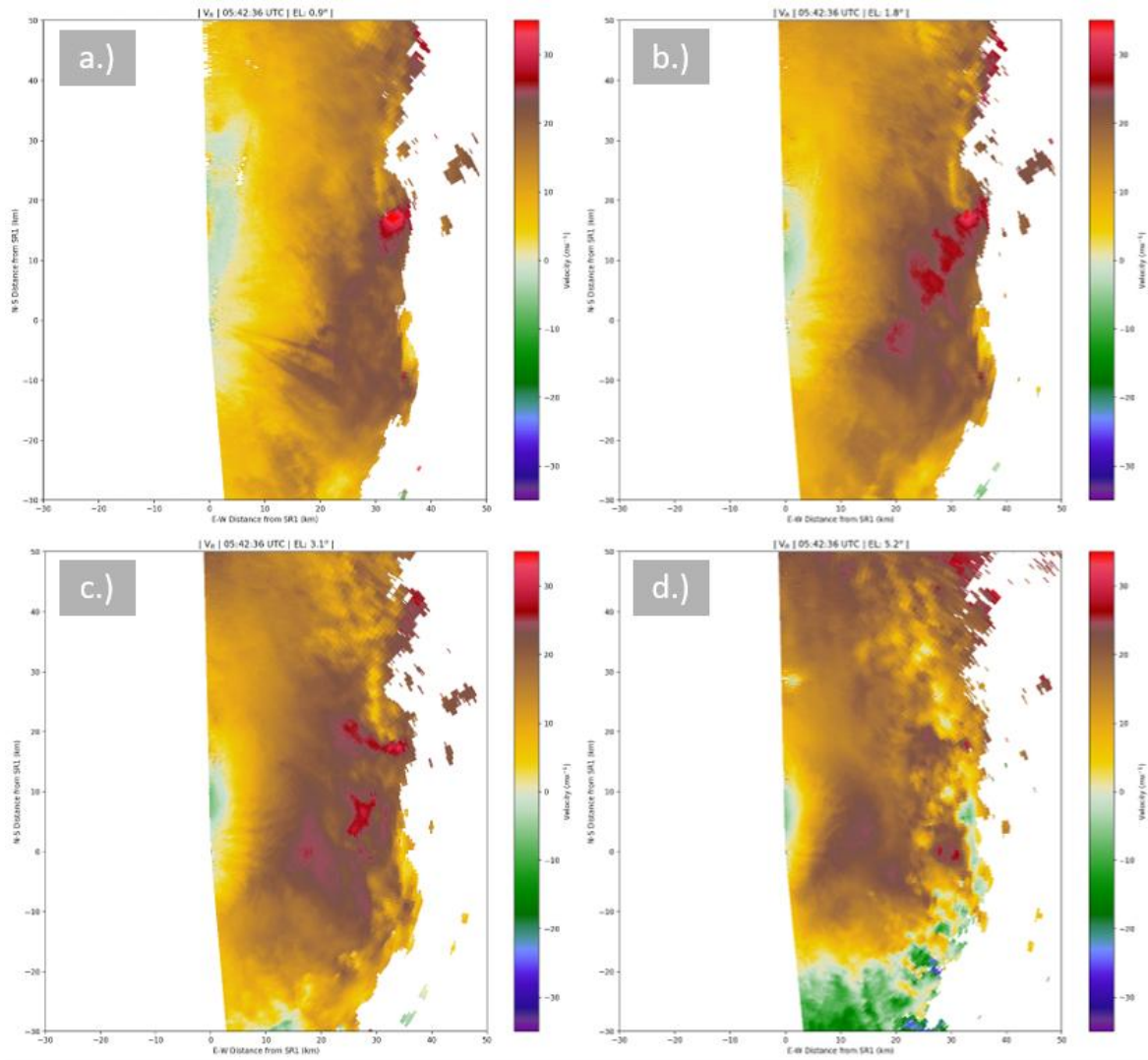


Figure 4.25: Radial velocity from the 0542 UTC volume scan taken with SMART-R1 at (a) 0.9 deg, (b) 1.8 deg, (c) 3.1 deg, and (d) 5.2 deg in elevation.

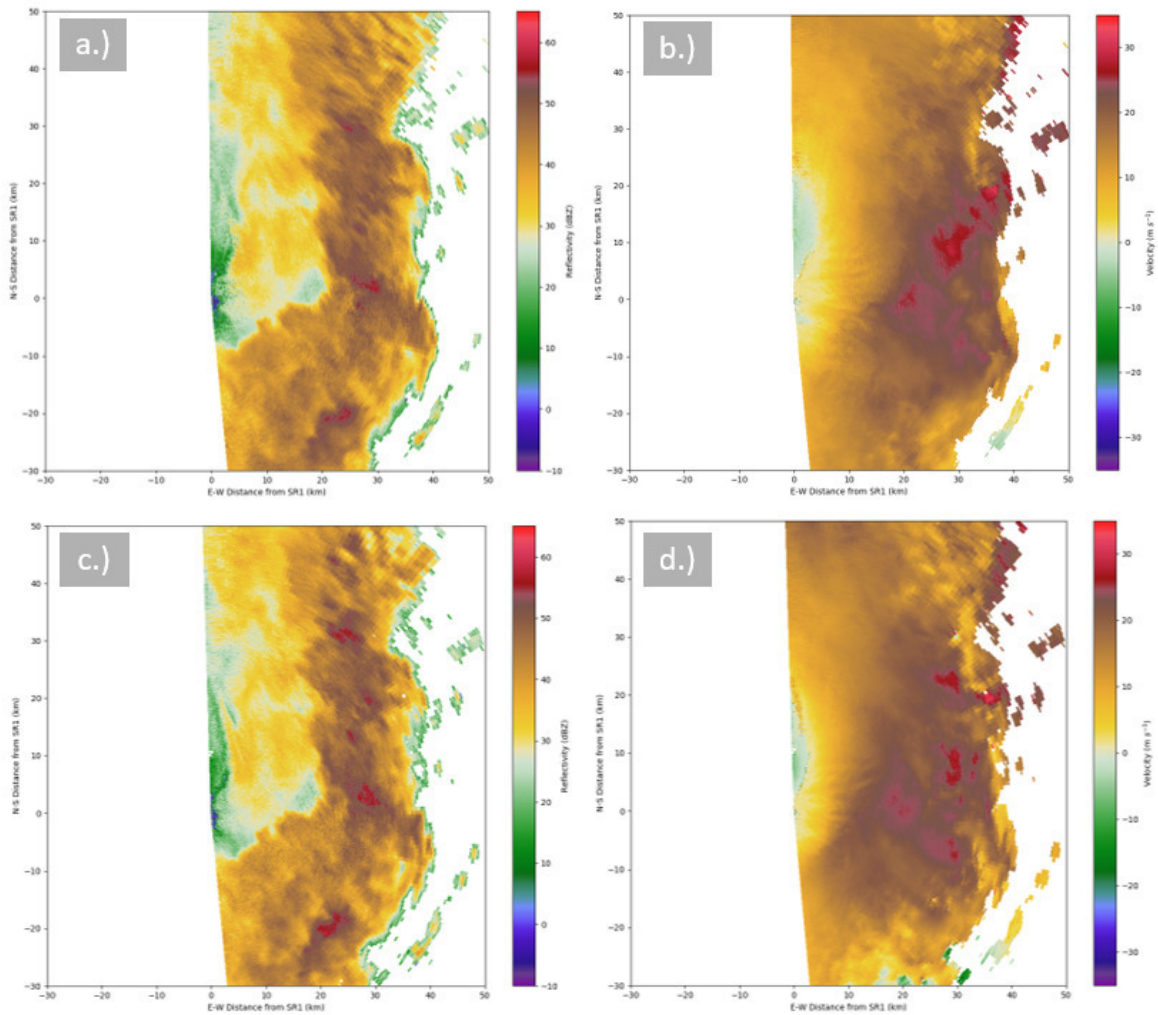


Figure 4.26: (a) Radar reflectivity and (b) radial velocity from the 0545 UTC volume scan at the 1.8 deg elevation taken with SMART-R1. (c) Radar reflectivity and (d) radial velocity from the 0545 UTC volume scan at the 3.1 deg elevation taken with SMART-R1.

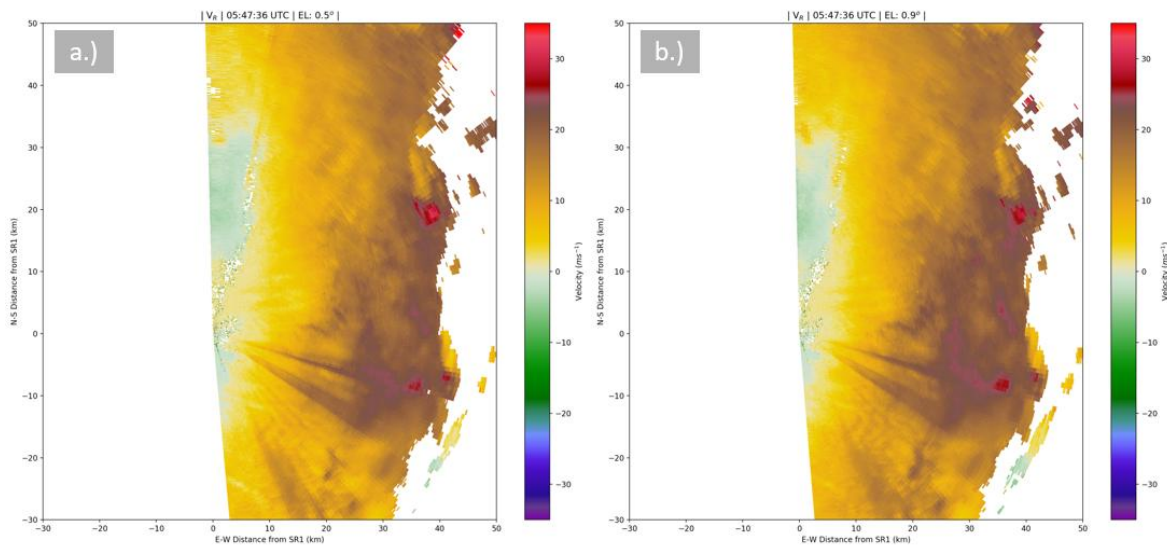


Figure 4.27: Radial velocity from SMART-R1 taken from the 0547 UTC volume scan at elevations of (a) 0.5 and (b) 0.9 deg.

In the final volume taken during the lifetime of the tornadic circulation at 0547 UTC, the rotational velocity of the circulation weakened significantly at all elevations. The highest observed velocities persisted mainly at the 0.5 and 0.9 deg tilts (*Figure 4.27*). The number of velocity gates exceeding 25 m s^{-1} was lower than at previous times, and mesovortex-associated circulation vanished above 2.3 deg (1.5 km). Above this elevation, the circulation was indistinguishable from the ambient storm-relative flow, indicating that weakening of rotation was well underway within the mesovortex at these heights. The mesovortex became further decoupled from rear-to-front flows at all but the 1.3 deg elevation angle ($\approx 990 \text{ m}$) and exhibited lower maximum velocities in the vortex region. The main core of the rear-to-front flow was now 5-7 km behind the main convective line at all other observed levels. The BWER had also eroded and was replaced with reflectivities of 45-50 dBZ, even at low levels (not shown).

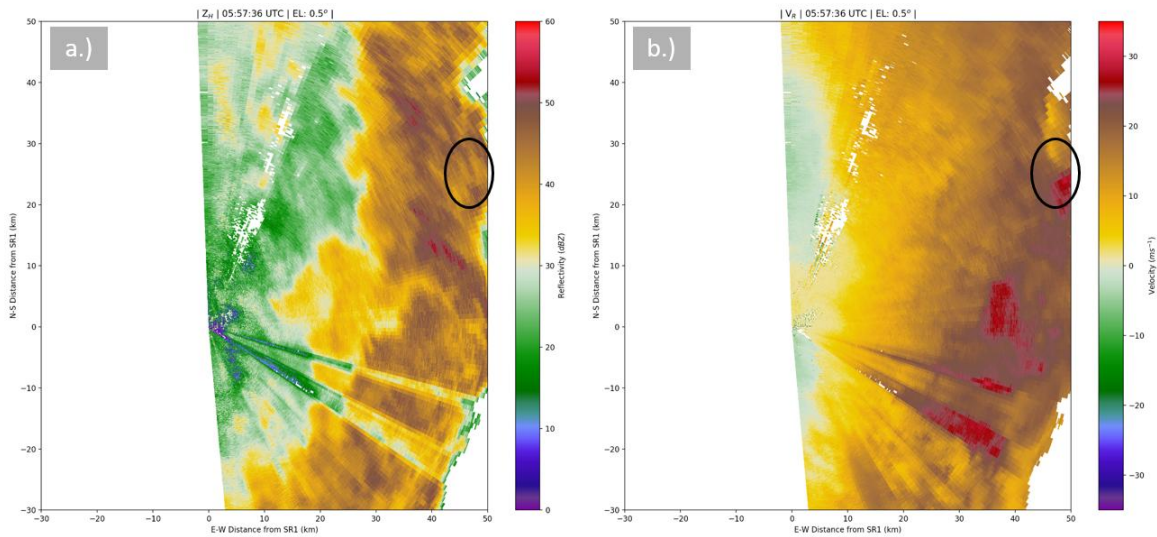


Figure 4.28: (a) Radar reflectivity and (b) radial velocity from the 0557 UTC SMART-R1 volume scan at 0.5 deg elevation.

The weakening of the vortex led to the dissipation of the tornado at 0548 UTC. Only a remnant circulation of cyclonic shear was observed by the last volume scan in the SMART-R1 analysis at 0557 UTC (*Figure 4.28*). The mesovortex continued to decouple from the combined rear-to-front flows and their associated convergence. By the final volume scan collected at 0557 UTC, the vortex had become embedded in an area of heavy precipitation associated with a thunderstorm along the edge of the complex's cold pool. Divergence underneath a likely downdraft effectively ended the mesovortex's lifecycle.

Chapter 5

Results: Dual Doppler Analyses

5.1 Mesovortex #1

5.1.1 Data Analysis Limitations

Data from the dual-Doppler analyses between KSHV and SMART-R1 elucidate numerous details about the processes of mesovortex maintenance and decay that influenced the tornado's lifecycle. Nevertheless, limitations to the analyses exist. To begin, the tornado first touched down at approximately 0511 UTC in front of the National Weather Service Shreveport, LA office (NWS Shreveport) and the KSHV NEXRAD site. As a result, the circulation was present in the "cone of silence" of the KSHV radar and little data could be gathered on the circulation's vertical structure at that time. Additionally, the crossbeam angle between KSHV and SMART-R1 was too low to garner meaningful wind retrievals during the five to six minutes following tornadogenesis. Therefore, there is an approximately six-minute gap in the dual-Doppler data around the time of tornado formation. Lastly, as the KSHV NEXRAD was operating in VCP-212 throughout this event, temporal resolution is around six to seven minutes for this mesovortex's analysis. As discussed in Houser et al. (2015), tornadoes and their parent, storm-scale circulations intensify on the order of ten seconds in supercell storms. Because some similarities exist between tornado formation across various storm modes, it is likely that the details related to tornadogenesis may be marred by this long update time. Regardless of the limitations, results obtained from the dual-Doppler analyses

still have significant observational value and should contribute to our understanding of this tornadic-QLCS mesovortex in terms of its maintenance and decay.

5.1.2 Vorticity Evolution Prior to Tornadogenesis

The mesovortex that produced the Shreveport-Bossier City, LA tornado was observed in two dual-Doppler analyses before tornadogenesis. At 0456 UTC the developing tornadic vortex was found at the southern end of a roughly north-south oriented band of enhanced vertical vorticity just behind the low-level broken band of convective updrafts (*Figure 5.1*).

The mesovortex of interest was within a region of weak vertical motion at 0456 UTC. At low levels, vorticity was well defined throughout the lowest 1 km of the atmosphere, exhibiting a slight northeastward tilt with height and having the highest intensity at 500 m. By 0504 UTC the highest low-level vorticity was found at 250 m (*Figure 5.2*). Surprisingly, the strength of the mesovortex weakened above 250 m between the two analysis times. The 500 m vorticity decreased significantly from $\sim 2.0 \times 10^{-2} s^{-1}$ at 0456 UTC to less than $8.0 \times 10^{-3} s^{-1}$ at 0504 UTC.

Vertical motion, on the other hand, had become increasingly organized above 500 m altitude, with the mesovortex embedded in the updraft core at 750 m. Updraft speeds were only 5-15 $m s^{-1}$ at low levels but increased aloft (*Figure 5.3*), suggesting that stretching processes may have contributed to the later vorticity intensification. After 0504 UTC the vortex moved into the KSHV cone of silence, resulting in a temporal gap in the analysis between 0504 UTC and the next available analysis time at 0517 UTC.

| 04:56 UTC | ζ & W |

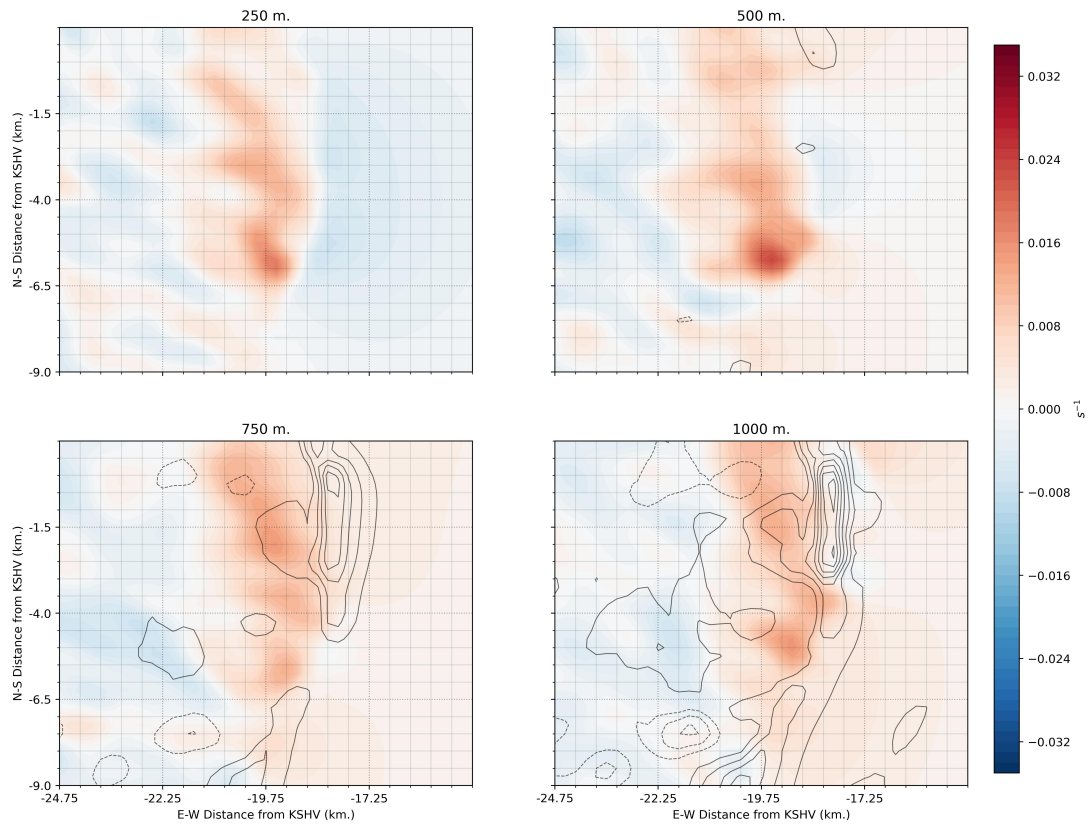


Figure 5.1: The mesovortex region at 0456 UTC from 250 m to 1 km AGL. Vorticity is filled in color, and vertical motion is contoured every $2.5 m s^{-1}$ in black (positive values use solid contours; negative values use dashed contours).

| 05:04 UTC | ζ & W |

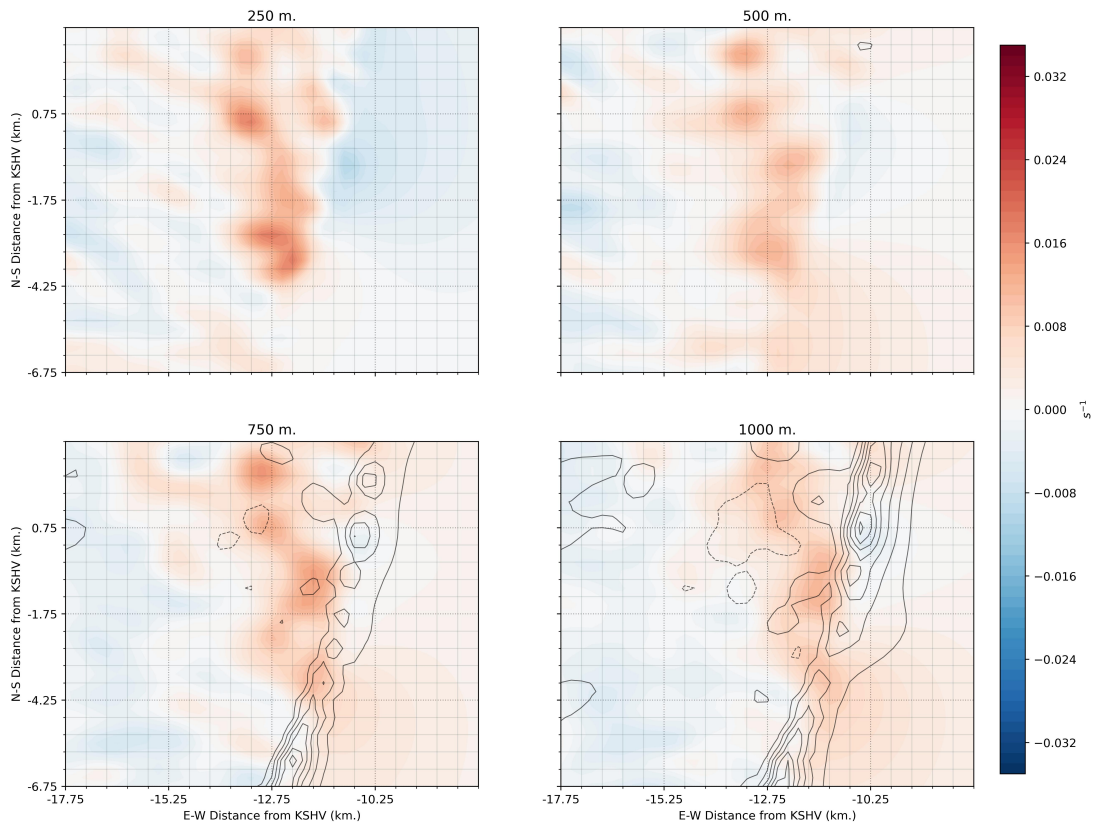


Figure 5.2: As in *Figure 5.1*, but for 0504 UTC.

| 05:04 UTC | ζ & W |

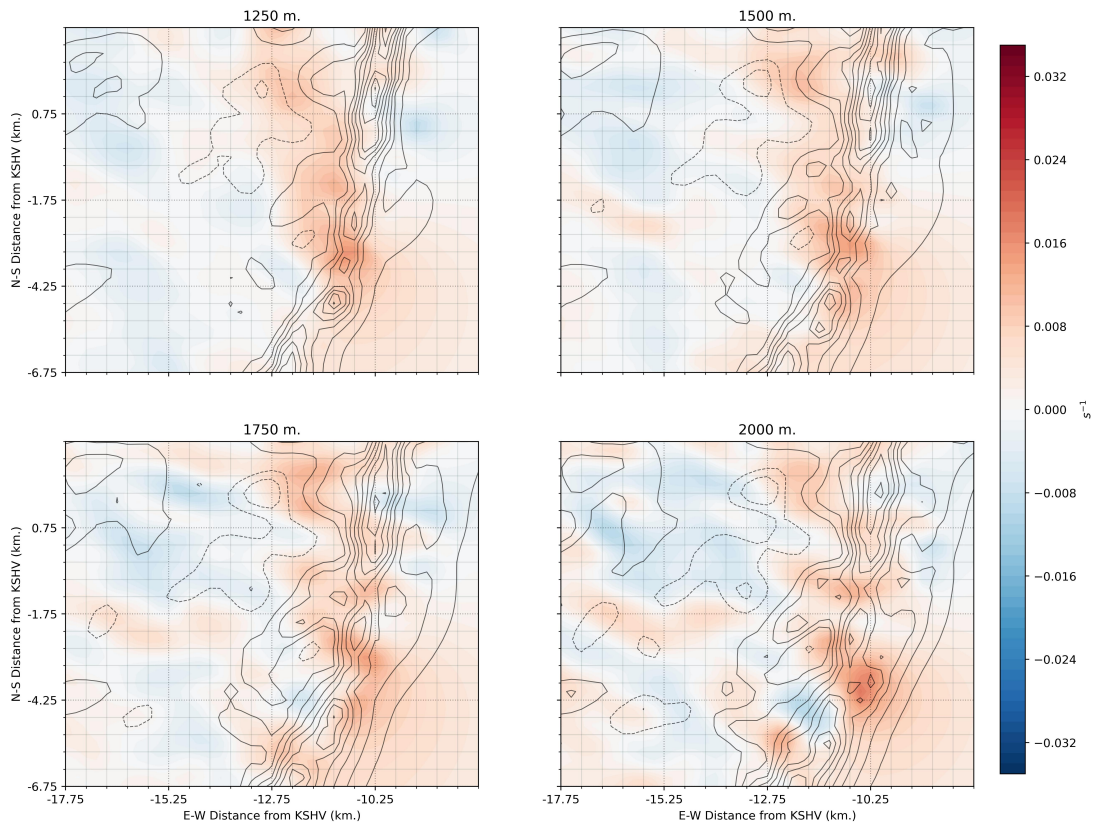


Figure 5.3: As in Figure 5.2, but for heights between 1.25 and 2 km.

5.1.3 Tilting and Stretching Before Tornadogenesis

Evaluating the tilting and stretching portions of the vorticity tendency equations can help to explain the mesovortex's behavior. It should be noted it is not possible to evaluate tilting at the lowest altitude in the analysis (250 m).

The tilting term magnitude at 0456 UTC (*Figure 5.4*) yields a partial explanation as to why the vortex underwent weakening above 250 m. While there is a strong maximum in positive tilting of vorticity along the back edge of the main convective updraft at 750 m, this region of maximum tilting is not collocated with the primary mesovortex. The primary vortex is instead associated with weak negative tilting at 500 and 750 m, and mostly neutral tilting at 1 km. Given that the vortex was in a region having weak vertical motions at the time, stretching of the existing vorticity (*Figure 5.5*) did not compensate for the loss through negative tilting despite weakly-positive stretching at both 750 m and 1 km altitudes. Therefore, vorticity decreased in the core of the mesovortex above 250 m between 0456 and 0504 UTC.

Much of the area of strong tilting at 0456 UTC was also associated with positive stretching of vorticity (*Figure 5.5*), and that area of vorticity did increase in strength (c.f. *Figures 5.1* and *5.2*). However, this lobe of enhanced vorticity was nearly 2 km north of the mesovortex that would later become tornadic and did not appear to contribute to tornadogenesis. Perhaps the most telling indicator that the southern mesovortex would develop further while the northern lobe of vorticity would weaken with time was the collocation of the updraft with the southern vortex at 0504 UTC. Looking at both the 750 m and 1 km levels in *Figure 5.2*, the updraft features only intersect with the southern vortex. The various other, stronger regions of vorticity at these altitudes are all located to the rear of the main updraft band. Hence, only the southern vortex was in a position to benefit from rapid intensification via enhanced stretching.

The stretching of vertical vorticity at 0504 UTC is shown in *Figure 5.6*. As suggested by the juxtaposition between the vortex and the updraft band, significant positive stretching is occurring within the existing vortex at 750 m and 1 km altitude. It is likely that the updraft matured as the vortex crossed the baseline with additional significant stretching over the entire depth of the vortex during the period between wind retrievals.

Decomposing the tilting term into its streamwise and crosswise components was undertaken, as numerical simulations have highlighted the presence of tilted crosswise vorticity as a main player in the intensification process of mesovortices in QLCSs (Trapp and Weisman 2003; Atkins and St. Laurent 2009b). Given that the total tilting was weakly negative for the southern mesovortex at 0456 UTC, it comes as no surprise that the crosswise component of tilting was also weak in the southern mesovortex region (*Figure 5.7*). In the area with strongly positive total tilting, 2 km to the north of the primary vortex, there was again relatively weak crosswise tilting, indicating that streamwise tilting of horizontal vorticity into positive vertical vorticity was the primary mechanism increasing vorticity in that area. The only significant positive crosswise tilting was found along the edges of the updraft band well north (by ~ 5 km) of the mesovortex of interest. These observations remained true at 0504 UTC (*Figure 5.8*), especially at 1 km altitude.

While the low-level vorticity weakened above 250 m altitude between 0456 and 0504 UTC, there was a slight increase in the vorticity at 250 m. Apparently, this increase was associated with unobserved tilting below 500 m, as no other sources could be identified. Either near-surface tilting was responsible for the modest increase or the forcing occurred too rapidly to be captured by the temporal resolution of the SMART-R1 and KSHV volume scanning repeat cycle.

The 0504 UTC analysis also illustrates the complexity of vorticity changes along the convective line. The northern part of the updraft band shown in *Figure 5.2* had positive

| 04:56 UTC | Tilting, SR-Wind, ω_H |

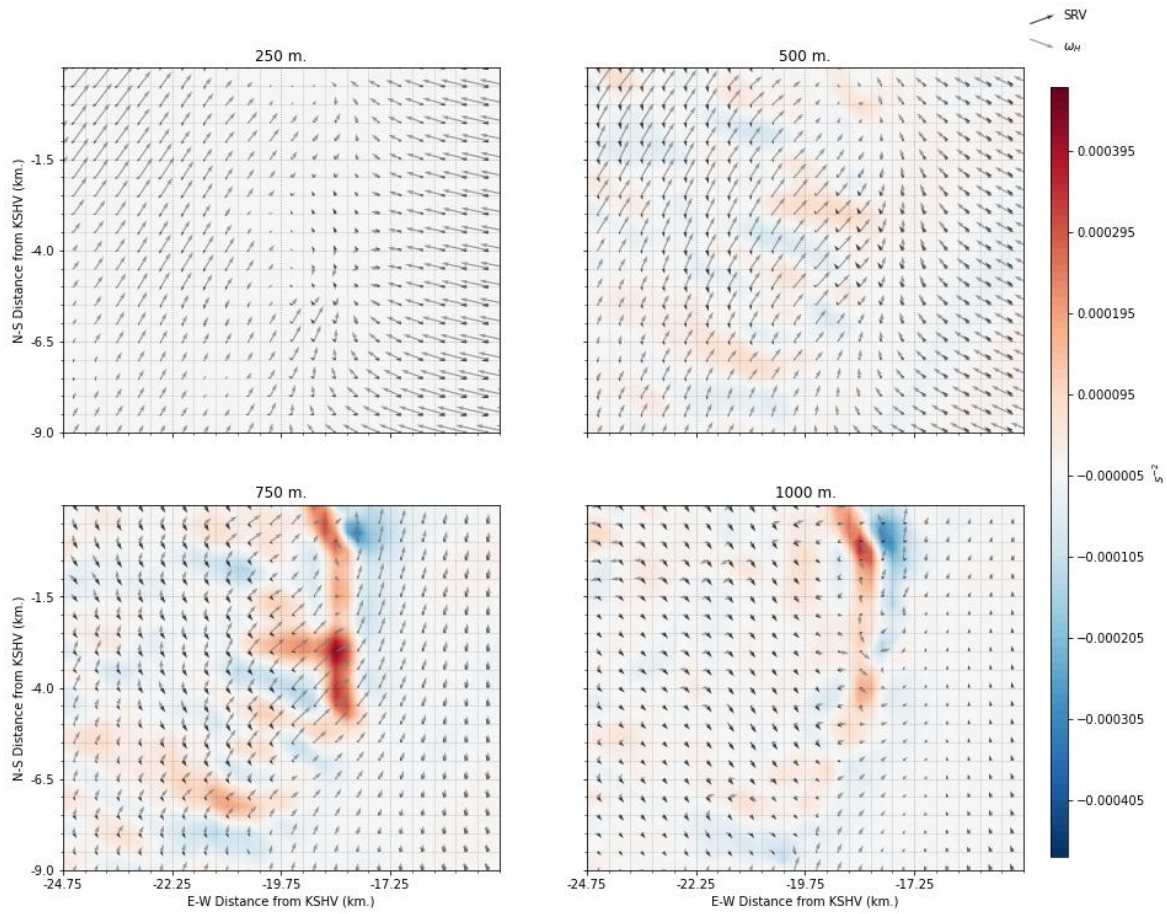


Figure 5.4: The total tilting term magnitude (in color), storm-relative winds (black arrows), and the horizontal vorticity vector (ω_H ; gray arrows) in the mesovortex region at 0456 UTC. The domain of this figure matches that of *Figure 5.1*.

| 04:56 UTC | Stretching & ζ |

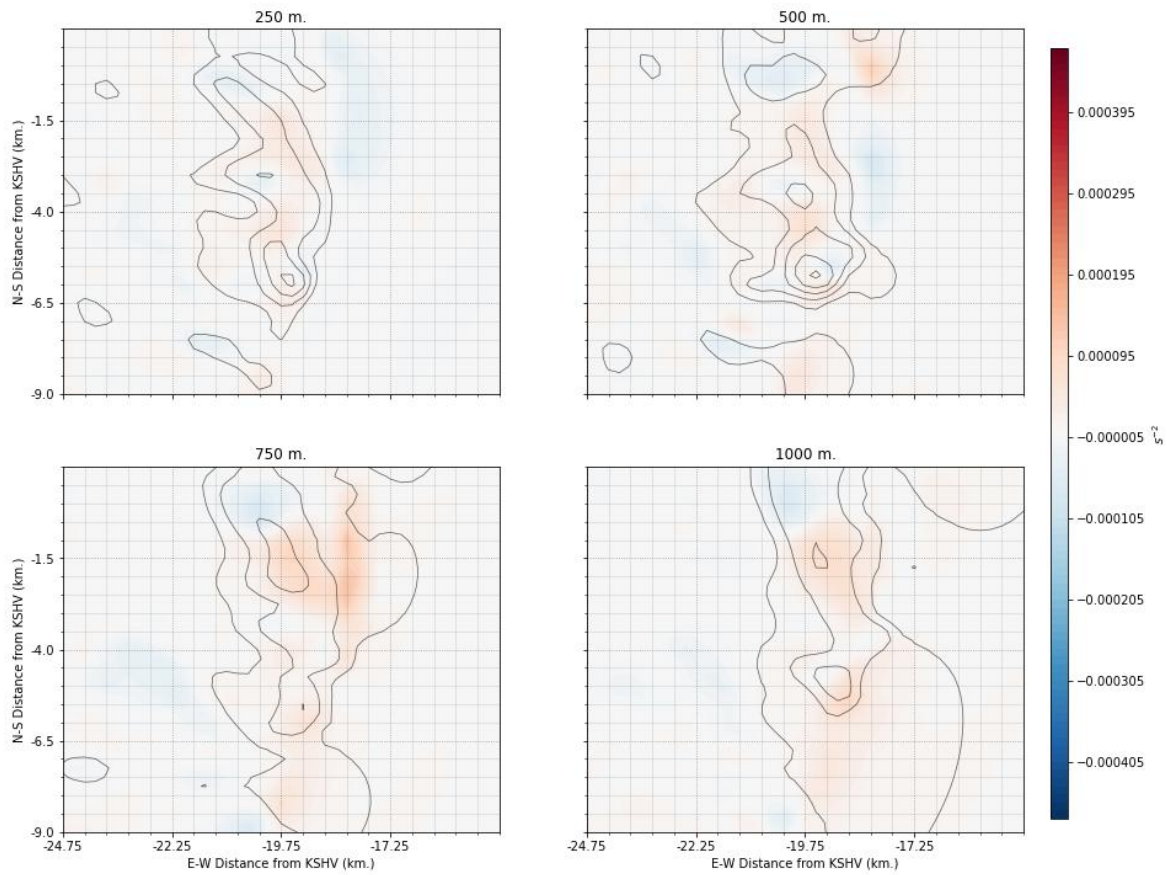


Figure 5.5: As in *Figure 5.4*, but for the stretching term magnitude.

| 05:04 UTC | Stretching & ζ |

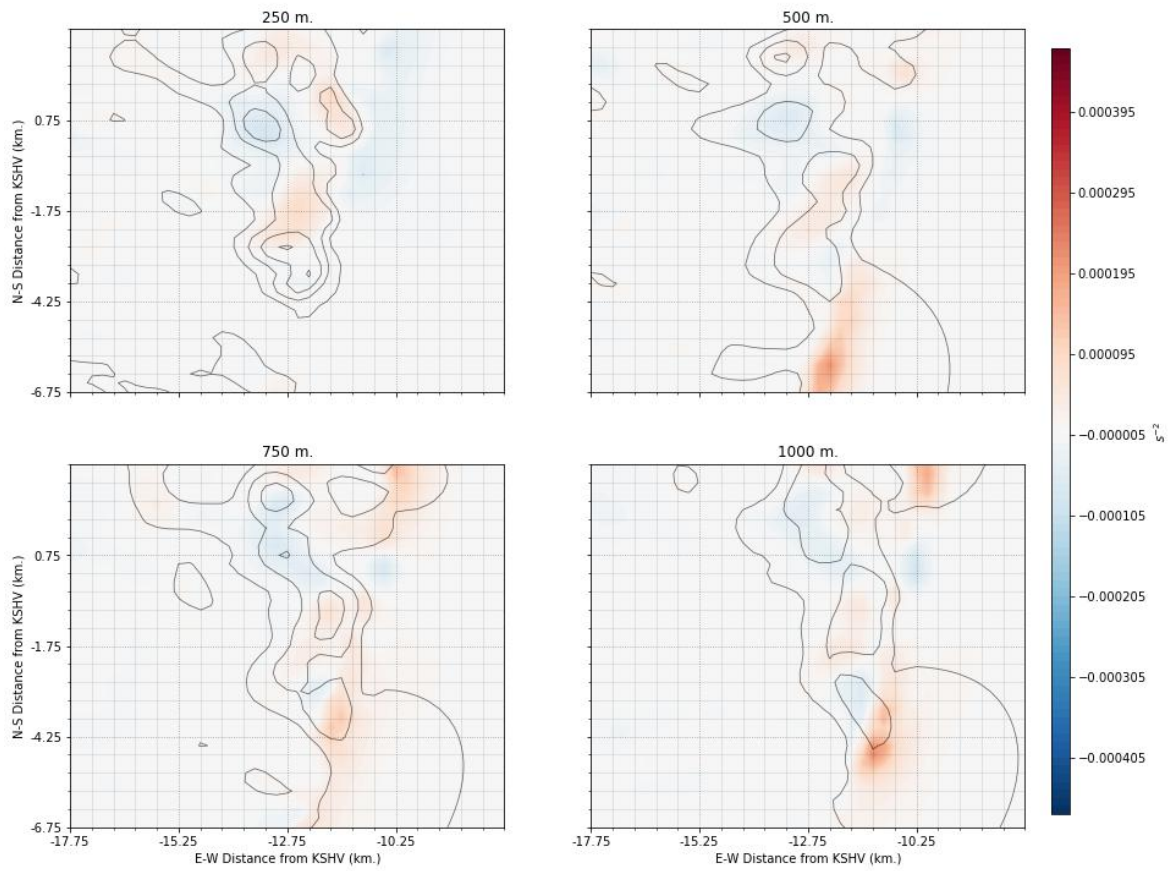


Figure 5.6: As in *Figure 5.5*, but for stretching at 0504 UTC.

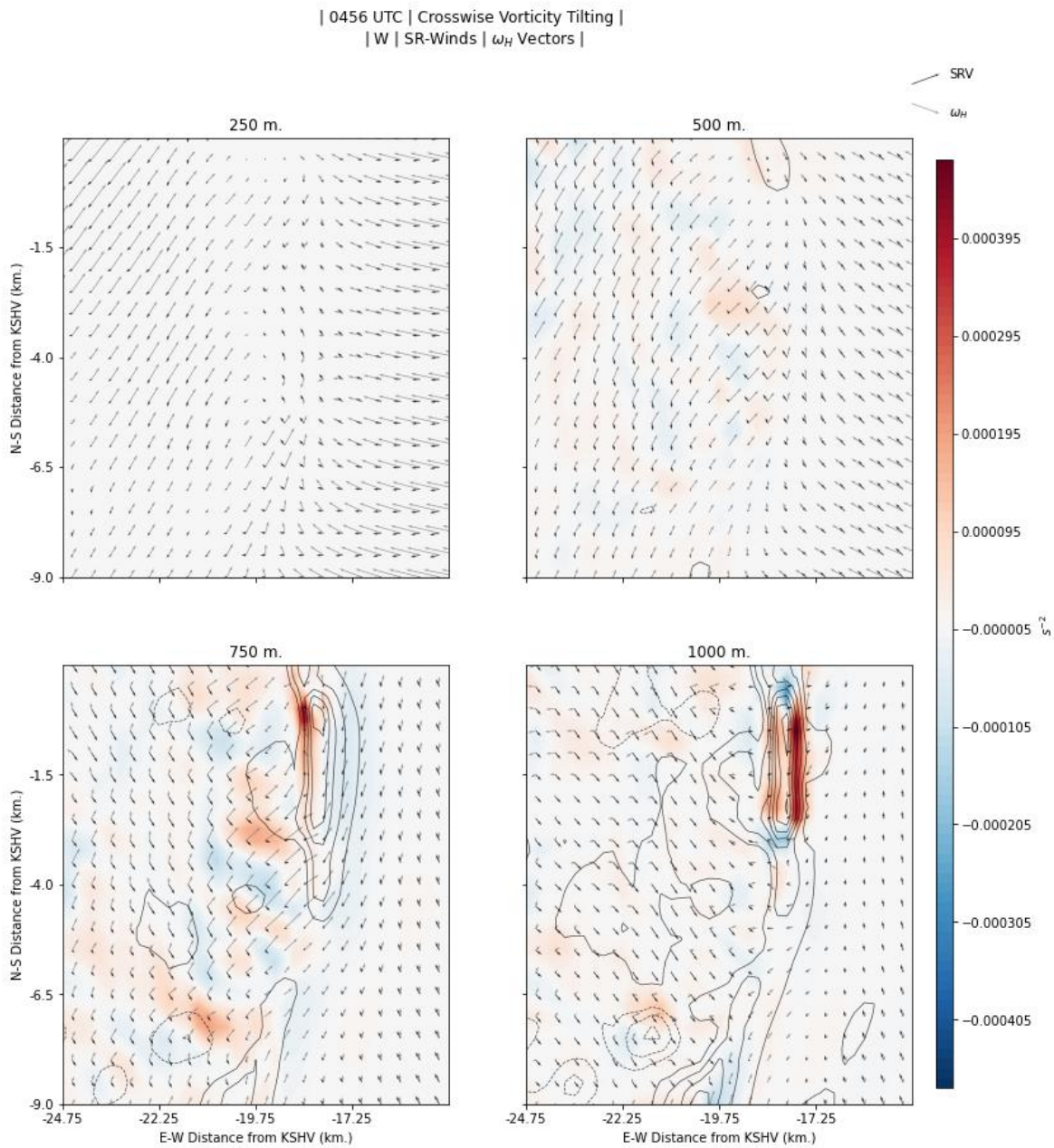


Figure 5.7: The magnitude of the crosswise component of the tilting term at 0456 UTC. Tilting magnitude filled in color, vertical motion is contoured in black every 2.5 m s^{-1} (solid contours represent upward motion, dashed contours represent downward motion), horizontal vorticity vectors are in gray, and storm-relative wind vectors are in black.

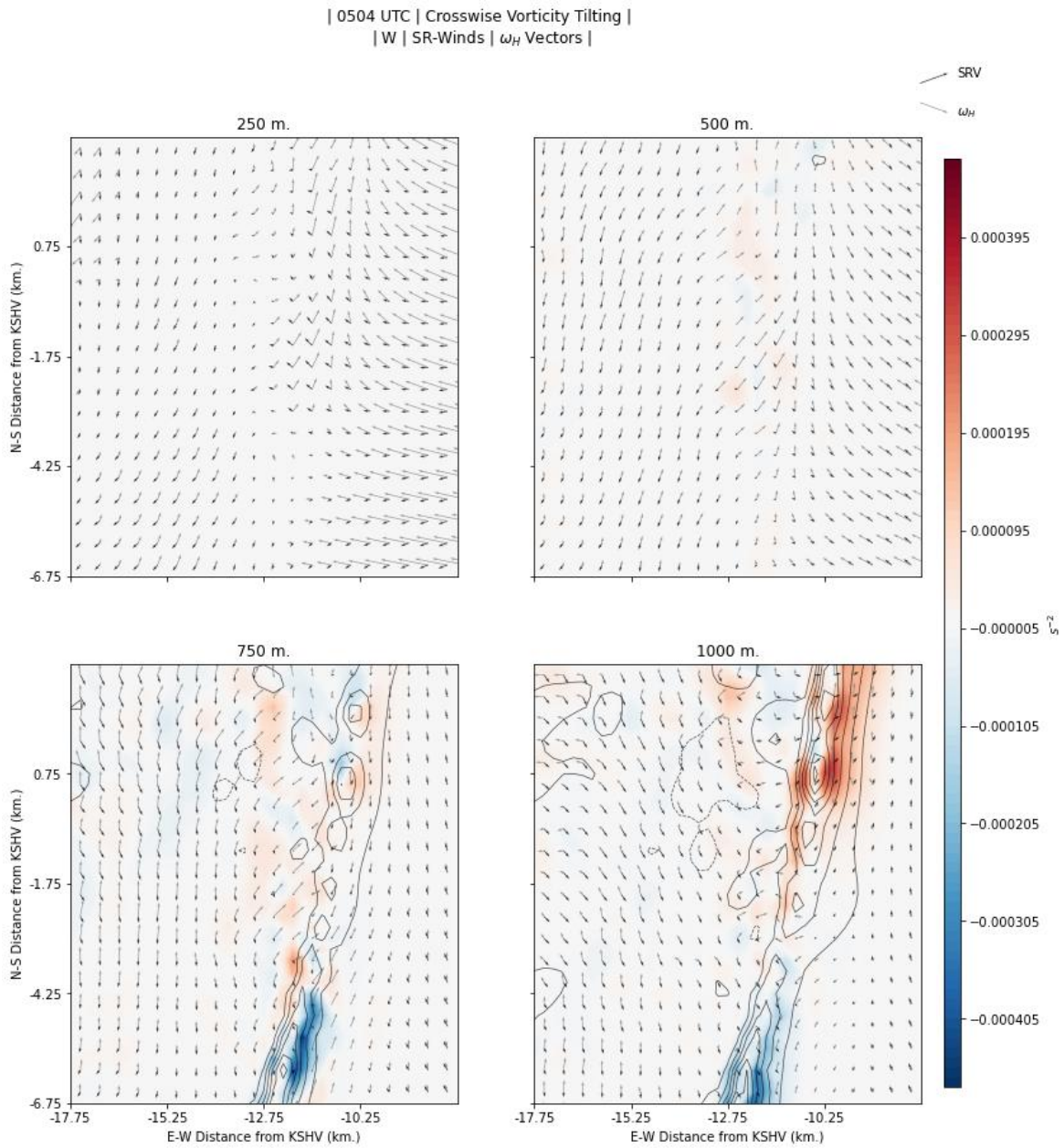


Figure 5.8: As in *Figure 5.7*, but for 0504 UTC.

crosswise tilting while the southern part had negative crosswise tilting of comparable magnitude. These differences were the result of slight discrepancies in the orientation of the horizontal vorticity vector. In the southern part of the band, the horizontal vorticity had an easterly component while to the north of it had a westerly component. With the updraft band being quasi-north-south oriented, a westerly component of horizontal vorticity was required to gain positive vertical vorticity as the air entered the leading edge of the system's updraft gradient.

One of the most noteworthy characteristics of the vorticity field and its changes during this period is the spatial and temporal scales of the features. Individual areas of vorticity undergo significant evolution from one analysis to the next. Additionally, the spatial extent of the of the tilting and stretching regions is between 500 m to 2.0 km in horizontal dimension. The primary mesovortex of interest only strengthened below 500 m between 0456 and 0504 UTC, slightly weakening at the other altitudes shown. It appears that the increase in vorticity at 250 m was associated with unobserved tilting below 500 m, as no other sources could be identified. Either near-surface tilting was responsible for the modest increase or the forcing occurred too rapidly to be captured by the temporal resolution of the SMART-R1 and KSHV volume scanning repeat cycle.

Another important aspect of the storm structure during this time period was that significant positive tilting of vorticity was occurring in different areas along the convective line, away from the soon-to-be tornadic vortex. If any of these other areas along the line were sustained for a longer period of time or would have been later enveloped by an updraft core with increasing vertical motion with height, other tornadic circulations may have developed. However, only the southern mesovortex was collocated with an updraft core at 0504 UTC.

5.1.4 Vorticity Evolution Post-Tornadogenesis

As the vortex moved through the KSHV NEXRAD cone of silence tornadogenesis occurred at 0511 UTC, yielding an extended-track, long-lasting EF1 tornado (National Centers for Environmental Information 2018). The first available analysis time post-tornadogenesis was 0517 UTC. At this time an intense vortex was found, especially at heights below 1 km altitude (*Figure 5.9*). Vorticity at 250 m was $3 \times 10^{-2} s^{-1}$, and generally increased with height up to 1 km altitude. Above this height, vorticity decayed slowly with altitude, though high vorticity magnitudes were observed through 2.75 km (*Figure 5.10*).

Additionally, strong updrafts were observed just to the north and north-northwest of the vorticity maximum. The updrafts were present from the lowest layers of the mesovortex structure at 500 m, rapidly increasing in intensity with height through 3 km. This intense updraft maintained a large degree of vertical alignment through the entirety of this layer; though a slight tendency to “lean” north in the environmental flow was noted.

A strong downdraft positioned to the northeast of the mesovortex was also observed at the same heights where updrafts were present. The combination of increasing vertical motion on the western part of the vortex and subsidence on the eastern portion of the vortex is reminiscent of the divided structure of the mature stage of a supercell mesocyclone (Lemon and Doswell 1979; Betten et al. 2018). However, in this case the vertical drafts were bands of upward and downward motion associated with multicellular convection.

Despite the banded nature of the strong gradients in vertical motion around the mesovortex, tilting of horizontal vorticity into positive vertical vorticity occurred in small pockets mainly on the western side of the existing vortex (*Figure 5.11*). Once again, the tilting features that supported the maintenance and strengthening of the mesovortex were relatively small (less than 1 km in horizontal scale), occurring in a shallow layer below 1 km above ground level. As noted by previous numerical studies of QLCS mesovortices (Trapp and Weisman 2003; Atkins and St. Laurent 2009b), the positive tilting of vorticity is mainly

| 05:17 UTC | ζ & W |

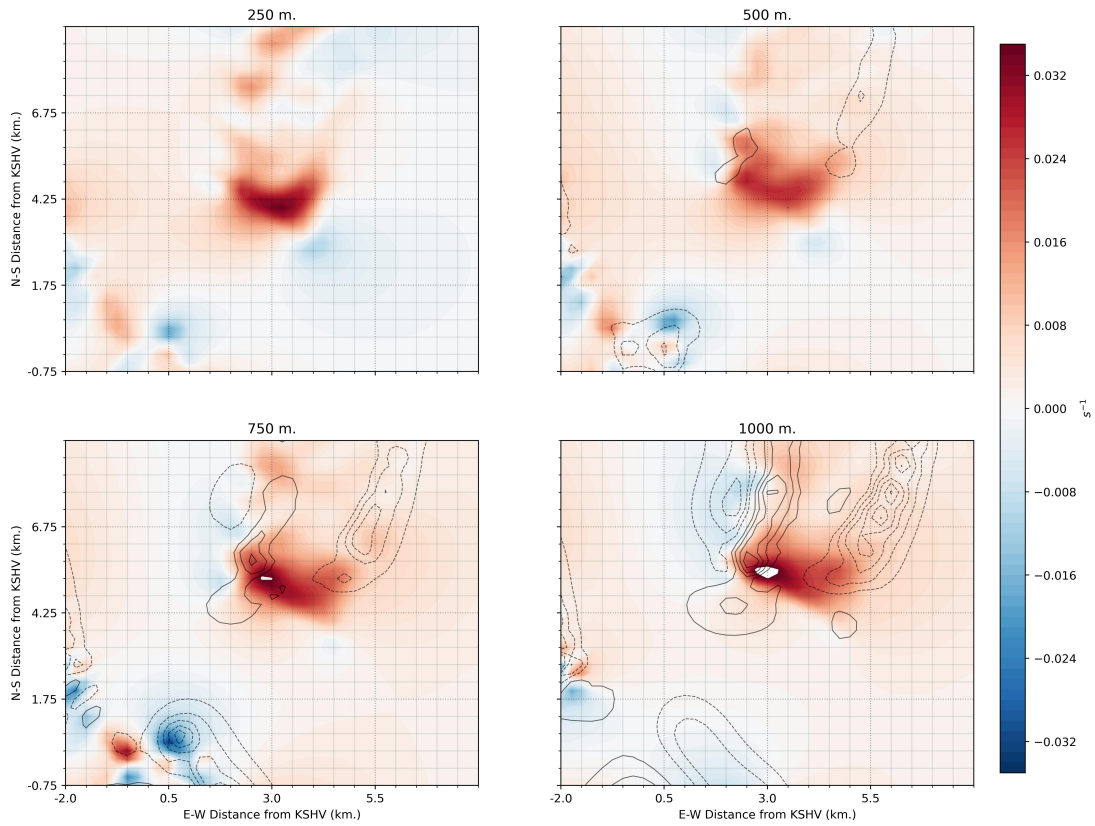


Figure 5.9: As in *Figure 5.1*, but for 0517 UTC as the vortex emerges from the baseline of the dual-Doppler domain.

| 05:17 UTC | ζ & W |

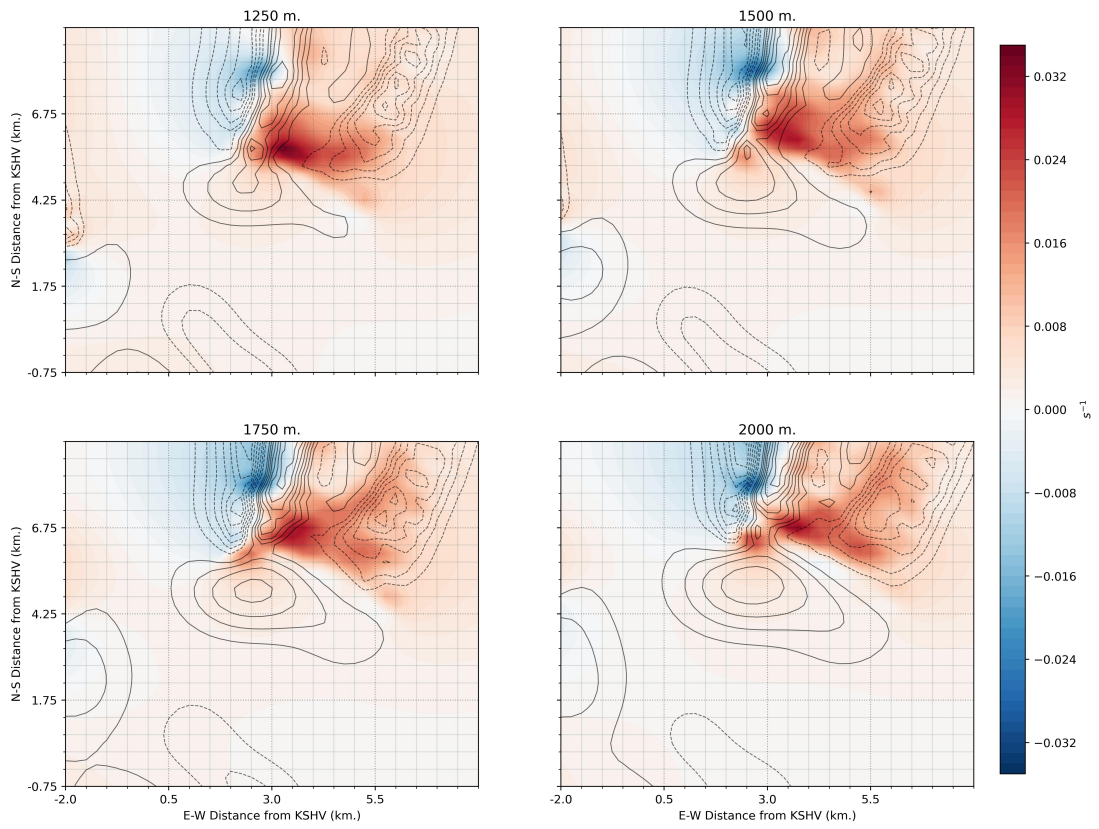


Figure 5.10: As in *Figure 5.9*, but for the 1.25 to 2 km layer.

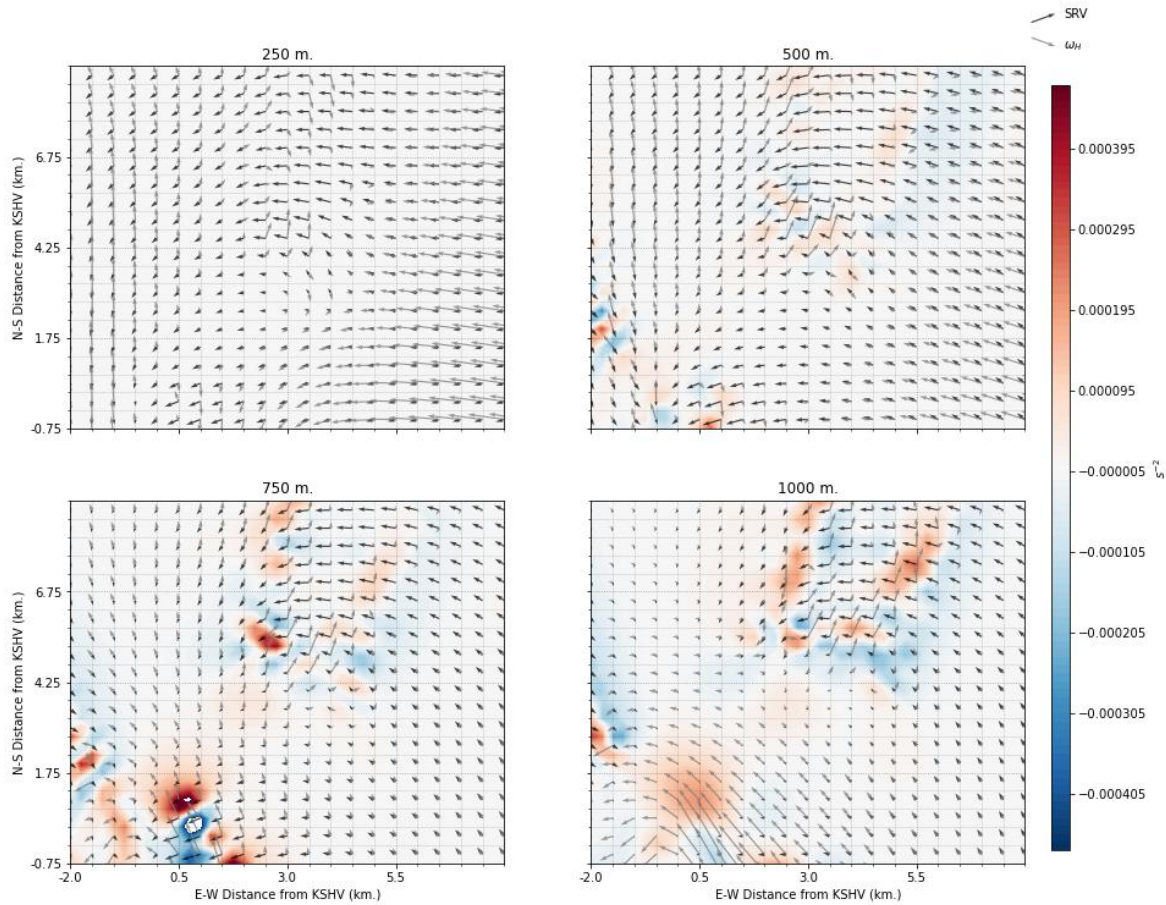


Figure 5.11: As in *Figure 5.4*, but for 0517 UTC.

through the crosswise component (*Figure 5.12*), with the streamwise component acting to dampen the total tilting rather than enhancing it in the area of the vortex (*Figure 5.13*). For example, the crosswise vorticity component tilting is strongly positive along the western edge of the updraft at 1 km altitude. Conversely, the streamwise vorticity component is strongly negative in that same region. The crosswise component was indeed stronger, yielding a moderately strong narrow band of positive vorticity tendencies on the western apex of the strong updraft. It should be noted that the tilting to the northeast of the vortex is co-located with the “inflow band” feature mentioned in *Section 4.1* and remained vertically continuous through much of the 250 m to 1 km layer.

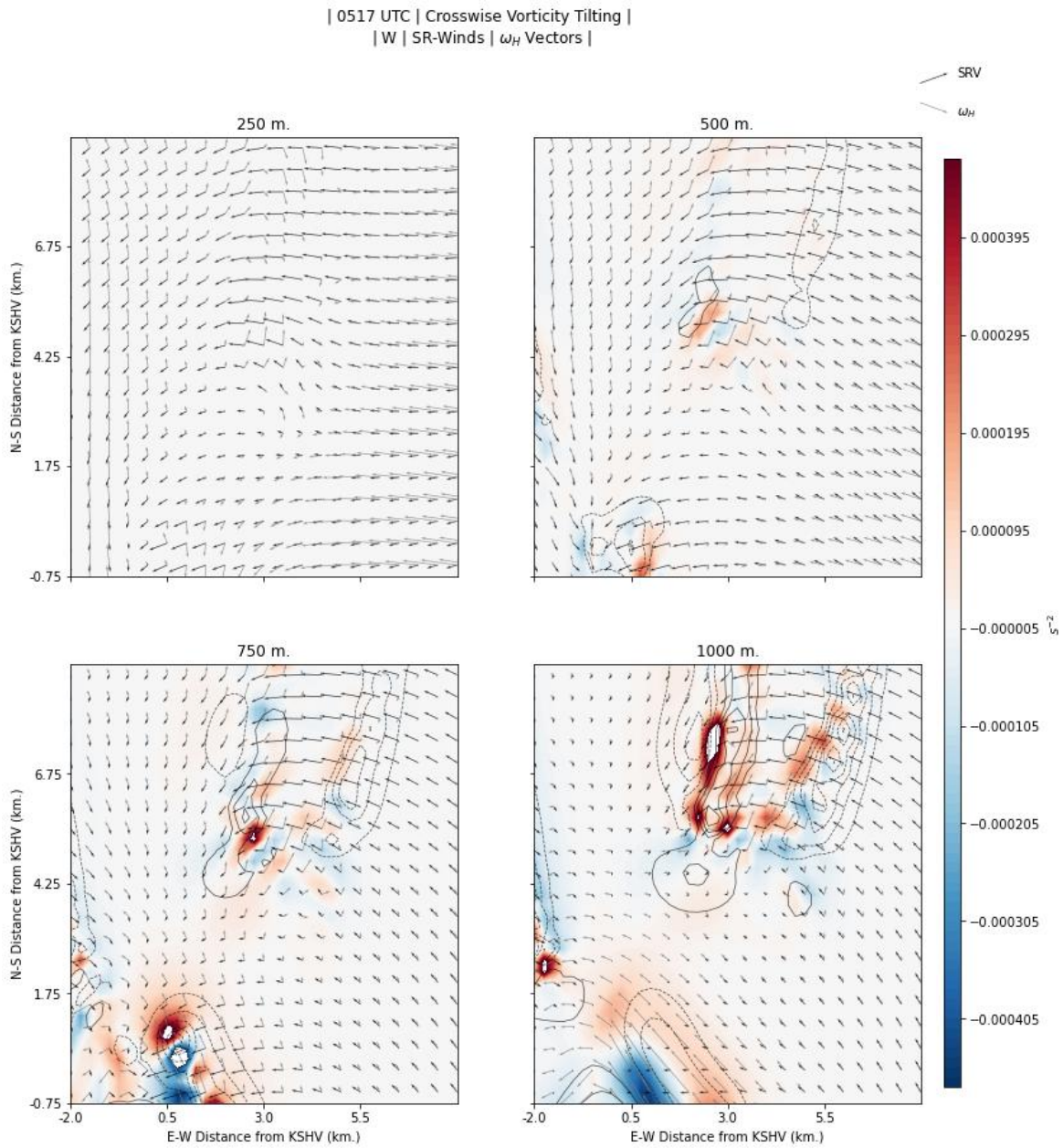


Figure 5.12: As in Figure 5.8, but for 0517 UTC, analyzed just after tornadogenesis.

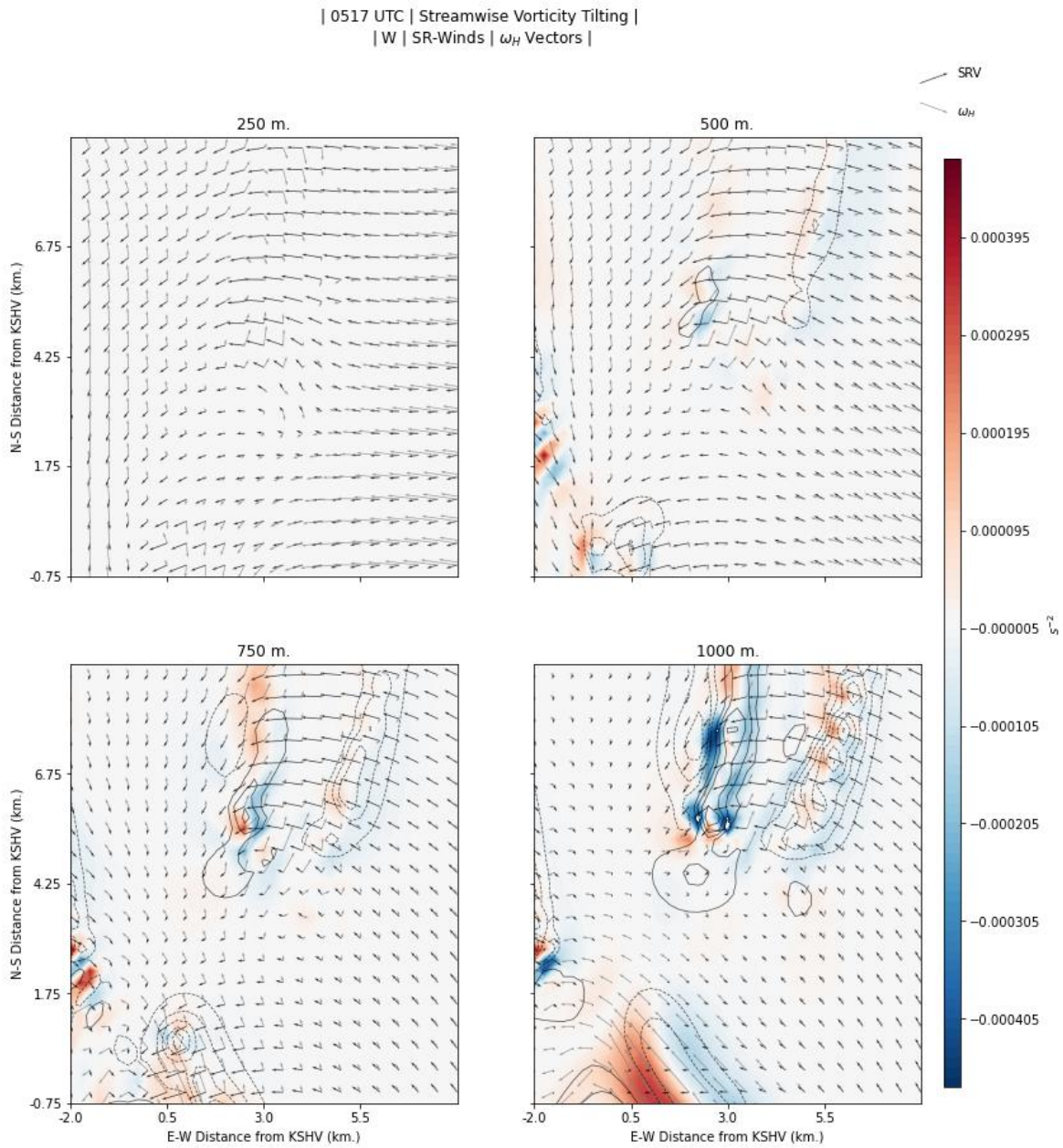


Figure 5.13: As in *Figure 5.12*, but for streamwise vorticity tilting term magnitude.

As suggested by the vertical gradient in vertical motions around the mesovortex depicted in *Figures 5.9* and *5.10*, the western side of the vortex was undergoing significant positive stretching through the lowest 1 km while the east side of the vortex was dominated by negative stretching (*Figure 5.14*). Therefore, maintenance and strengthening of the tornadic vortex was associated with crosswise vorticity tilting of in small pockets around the existing vortex, and positive stretching over a slightly larger scale and a larger portion of the mesovortex. Clearly, the regions of maxima in positive vorticity tendencies are less than 1 km in horizontal dimension and likely occurring on the tornadic scale within the broader mesovortex.

As the mesovortex continued eastward, the tornadic circulation continued to exhibit large magnitudes of vorticity close to the surface. Indeed, the time of the strongest vorticity observed at 250 m was found at 0524 UTC (*Figure 5.15*). Vorticity at that time approached $4 \times 10^{-2} s^{-1}$. While vorticity was maximized near the surface, the mesovortex was strong through its entire 3 km depth. While the vortex was mostly vertically oriented, there was a slight tilt to the northeast between 500 m and 1 km altitude.

Similar to the previous time period, the vorticity maximum was located in between an updraft and downdraft. However, at 0524 UTC, the vertical motions were weaker and the updraft was displaced further north, away from the vortex. Additionally, the downdrafts associated with the vortex region had become less intense, with speeds decreasing from between -10 to $-15 m s^{-1}$ to only $-5 m s^{-1}$ at 1 km altitude. The separation of the updraft away from the vortex and the weakening of vertical motions led to an abrupt change in the stretching term within the mesovortex (*Figure 5.16*, especially at the lowest analysis level. At 250 m, the vortex was dominated by strong negative vorticity tendency within its core, with this tendency extending eastward. Only the far northwest edges of the mesovortex were associated with positive stretching. While the magnitudes decreased with height somewhat, the negative vorticity stretching tendency dominated through 1 km altitude.

| 05:17 UTC | Stretching & ζ |

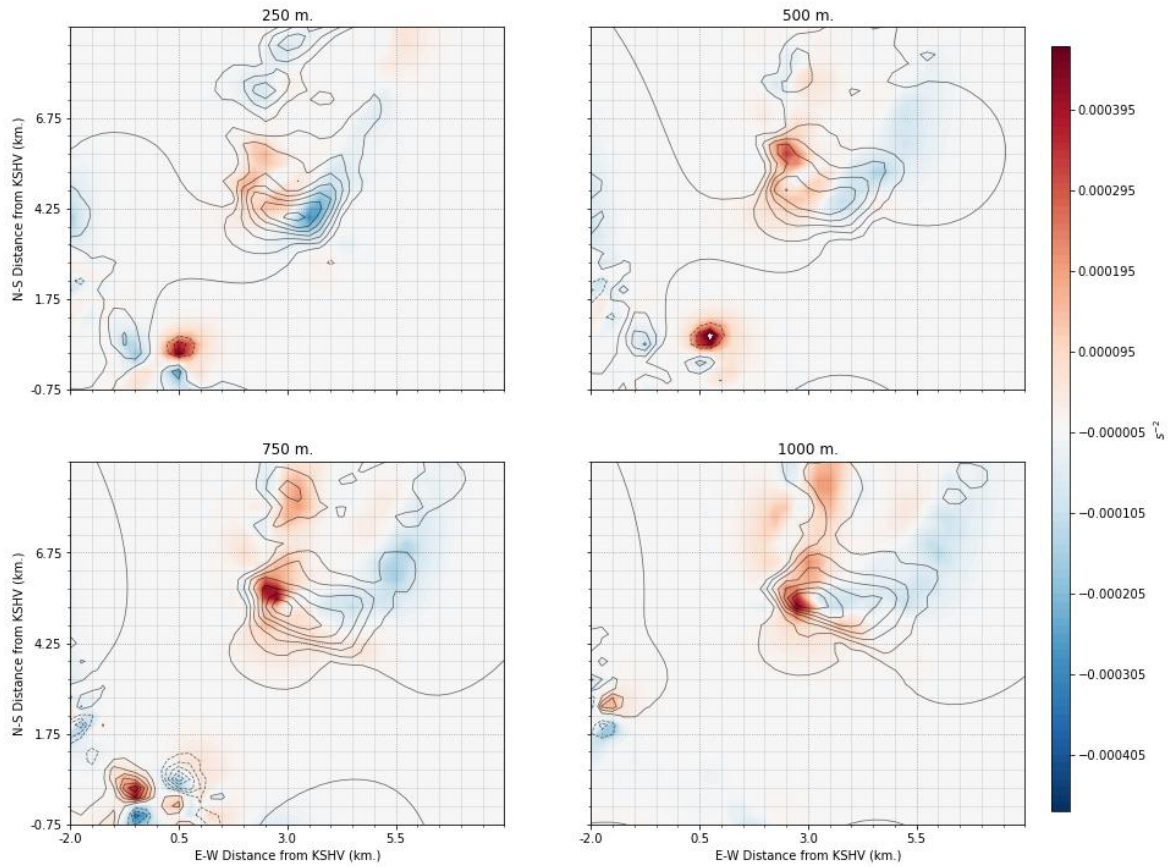


Figure 5.14: The stretching of vorticity term magnitude (color fill) and vorticity contours (positive values are solid; negative values are dashed) at 0517 UTC between 250 m and 1 km AGL.

| 05:24 UTC | ζ & w |

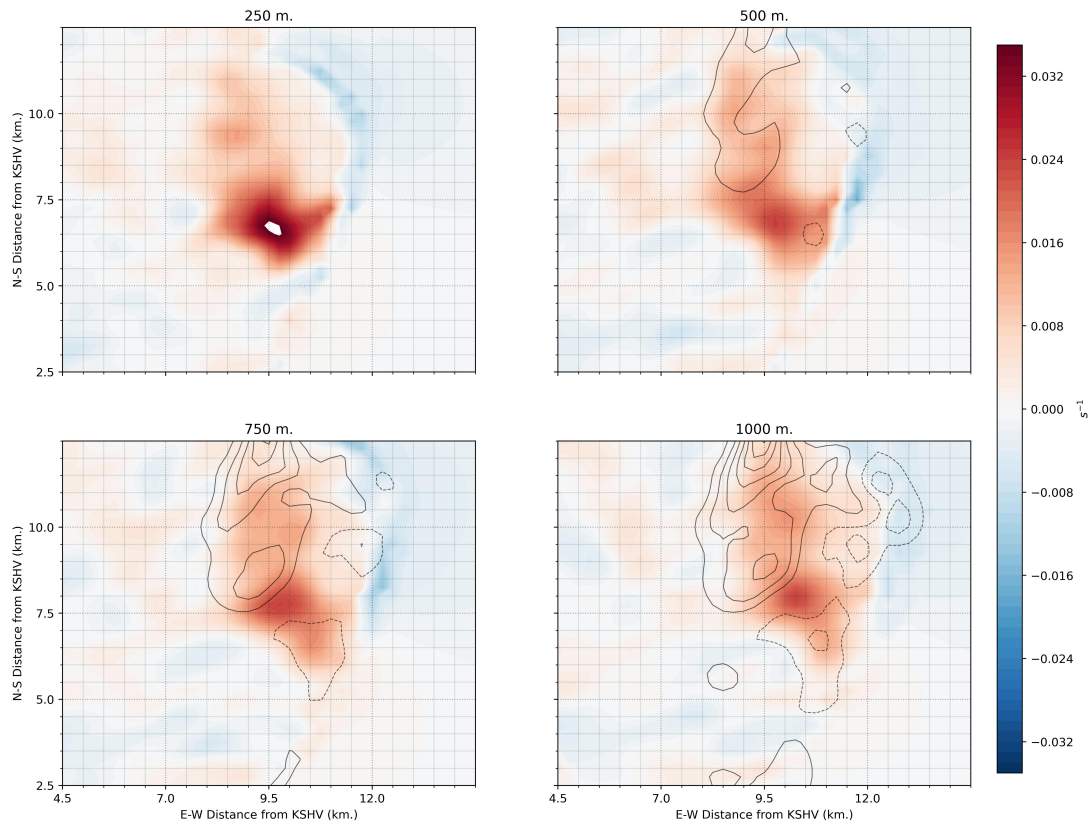


Figure 5.15: The vorticity field (color fill) and vertical motion (black contours with updraft denoted by solid lines, and downdrafts indicated by dashed lines) at 0524 UTC, between 250 m and 1 km.

| 05:24 UTC | Stretching & ζ |

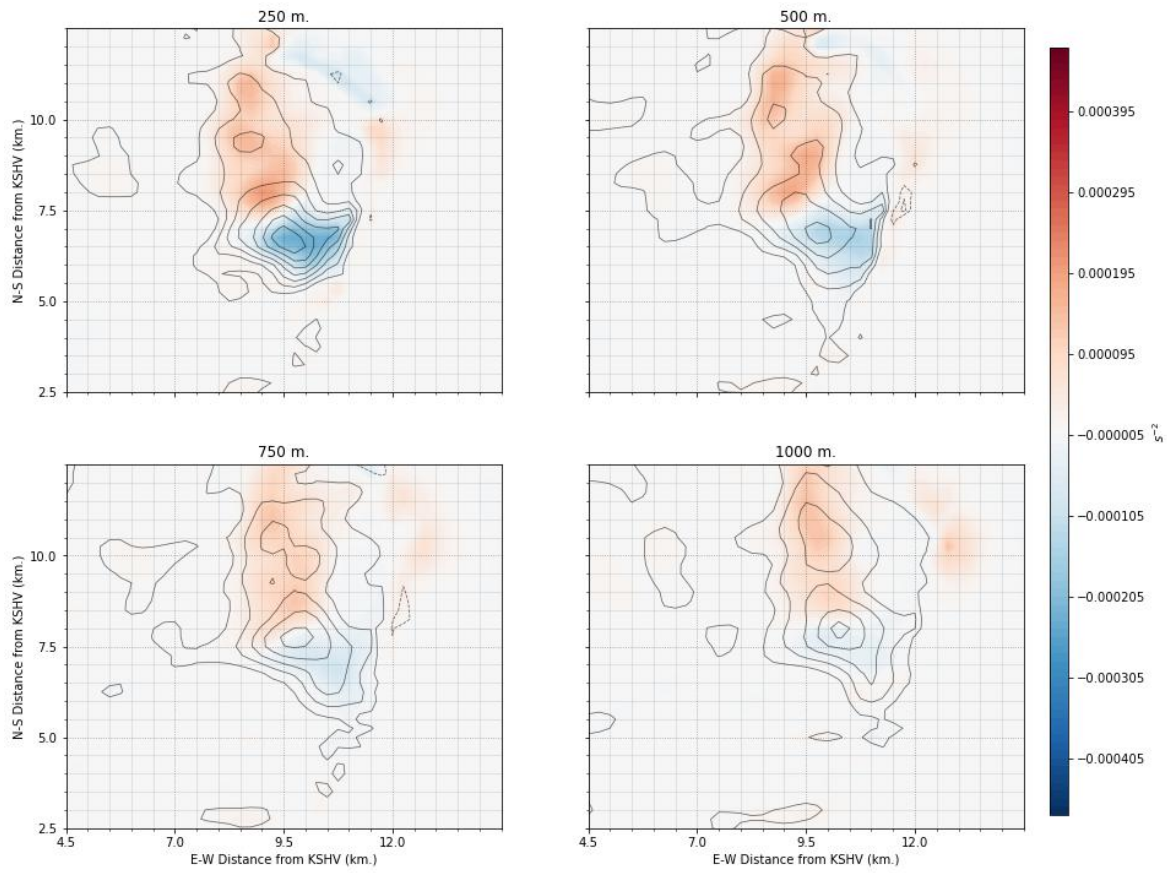


Figure 5.16: As in *Figure 5.14*, but for 0524 UTC.

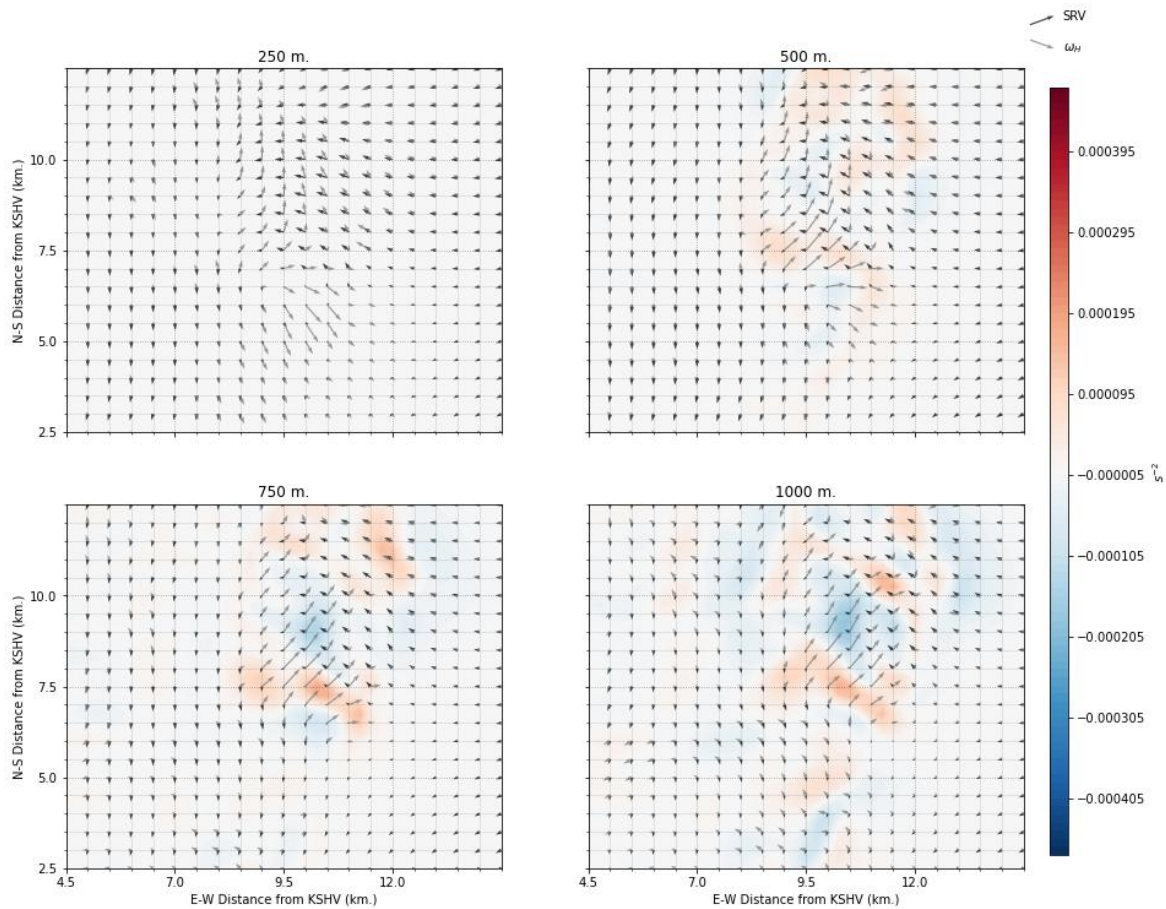


Figure 5.17: As in *Figure 5.11*, but for 0524 UTC.

The tilting term vorticity tendency behaved in a manner consistent with the much weaker gradients in vertical motion within the vortex region as the magnitude of total tilting decreased from values observed at 0517 UTC (*Figure 5.17*). Nevertheless, tilting of horizontal vorticity into vertical vorticity was still occurring across the northern part of the vortex. This tilting helped to compensate for the losses through negative stretching in that part of the mesovortex. This tilting maximum shifted in orientation from east-west at low levels to northeast-southwest oriented after 1 km altitude, highlighting continued interaction between the area of maximum tilting and the “inflow notch” of the mesovortex (discussed in the single Doppler analysis, *Section 4.1*).

More importantly, the nature of the positive tilting had evolved. Previously, the positive tilting around the mesovortex was associated with the crosswise component. At 0524 UTC, the positive tilting was associated with the streamwise component (*Figure 5.18*), while the crosswise component (not shown) was weak. The ingestion of and subsequent tilting of streamwise vorticity that occurred at this analysis time highlights a marked change in the predominant mechanism responsible for vorticity generation in the vortex region. The ability of the vortex to transition to a new source of tilted vorticity may explain why this particular mesovortex was able to effectively maintain its intensity for a long period of time, consequently producing a long-track tornado in the process.

Consistent with the negative stretching and narrow regions of positive tilting observed at 0524 UTC, the strength of the circulation began to lessen with time. This decrease occurred at all altitudes. However, the vorticity remained relatively strong in the lowest 500 m of the vortex region despite becoming somewhat elongated (*Figure 5.19*) due to the structure of the tilting of streamwise vorticity. Also notable in *Figure 5.19*, vertical motions remained weak, growing more displaced from the vortex center. At 1 km altitude the center of the vortex was embedded in mostly subsiding air. Given the lack of horizontal gradients in vertical motion near the vortex necessary for generating tilting and the weakness in vertical motions, it is not surprising that the vortex intensity diminished quickly between 0531 and 0537 UTC (*Figure 5.20*).

The most significant contribution to the decrease in vorticity was through the negative stretching (not shown) that existed throughout most of the vortex below 1 km altitude. The largest decrease in vorticity magnitude took place near the surface. Values of vorticity at 250 m plummeted from $2 \times 10^{-2} s^{-1}$ to much less than $8 \times 10^{-3} s^{-1}$. This stark decrease marked the beginning of the dissipation phase of the vortex's lifecycle.

Two main indicators underscored the weakening trend. First, the vertical motions in the vortex region had greatly decreased in intensity. Though updrafts were still present

| 0524 UTC | Streamwise Vorticity Tilting |
 | W | SR-Winds | ω_H Vectors |

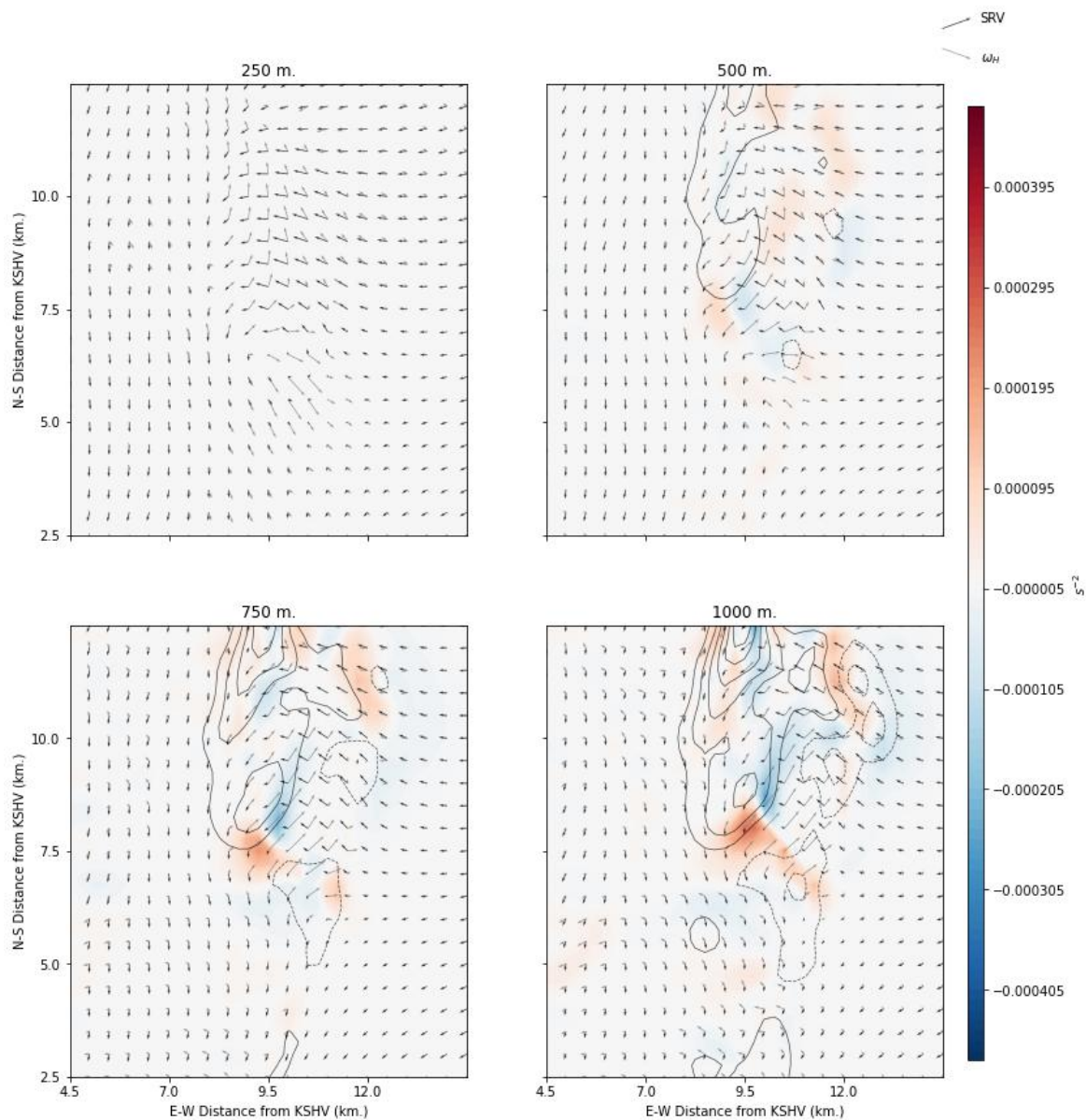


Figure 5.18: As in *Figure 5.13*, but for 0524 UTC.

| 05:31 UTC | ζ & ω |

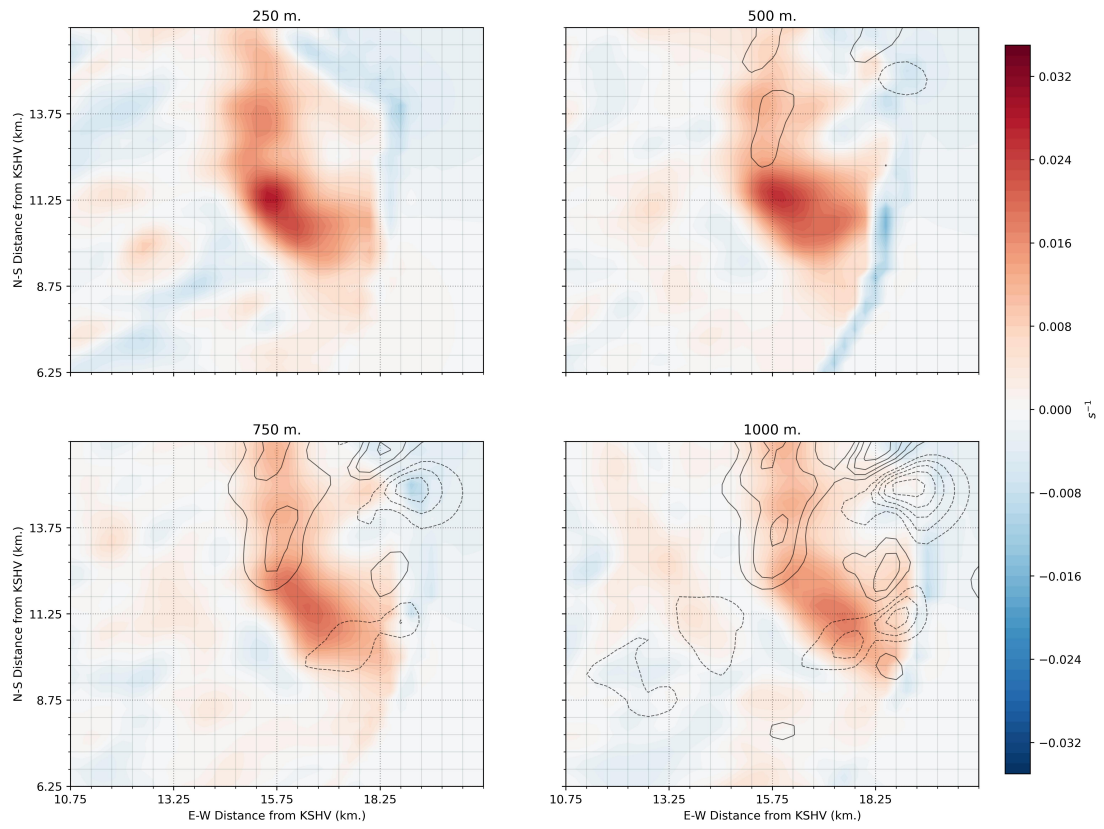


Figure 5.19: As in *Figure 5.15*, but for 0531 UTC.

| 05:37 UTC | ζ & W |

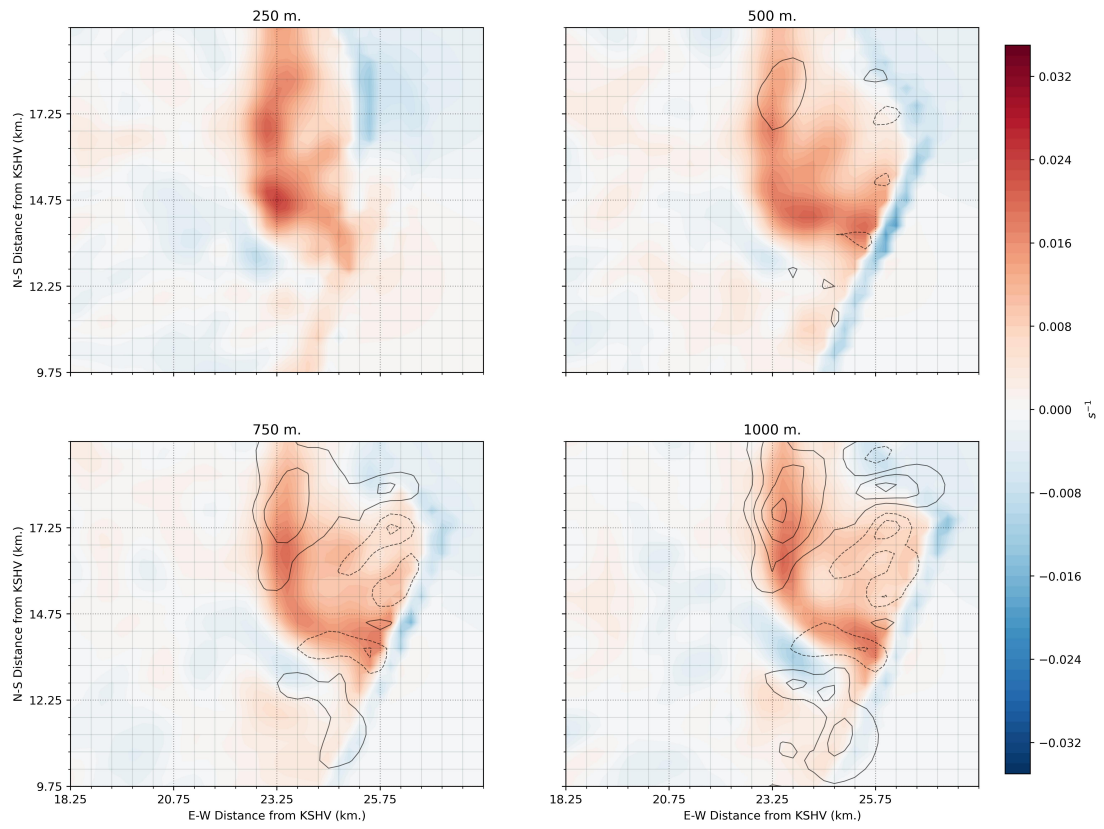


Figure 5.20: As in *Figure 5.19*, but for 0537 UTC.

and continued to increase in intensity with height, they were weak in character. Second, the strongest updrafts had become displaced from the vortex region, moving more than 2 km from the north-northwest to the center of the vorticity maximum. The effect of this displacement coupled with subsidence occurring on the eastern edges of the mesovortex was profound in the vorticity stretching term, as it quickly became negative. Additionally, the weaker and more separated vertical drafts resulted in weaker gradients of vertical motion around the vortex, which in turn weakened the tilting term.

During the dissipating stages of the mesovortex, the tilting term was minuscule in the vortex region, possessing values of less than $1 \times 10^{-4} s^{-2}$ within the inflow region east of the vortex. This small tilting maximum was displaced entirely from the mesovortex region by the end of the analysis period at 0537 UTC, decoupled from the mesovortex and confined to locations 2 to 4 km east and northeast of the main circulation (*Figure 5.21*).

Between the 0537 and 0544 analyses the EF1 tornado associated with the mesovortex dissipated (at 0541 UTC; National Centers for Environmental Information 2018). Within the final dual-Doppler analysis time at 0544 UTC, vorticity magnitudes had eroded at all levels below 500 m and the vorticity became notably elongated (*Figure 5.22*). The elongation of vorticity contrasted sharply with the concentrated, intense appearance of the vortex during its mature phase.

Despite the demise of the tornado at 0541 UTC and the weakening of surface vorticity, the formation of a new updraft to the north of the previously tornadic vortex and some positive stretching in the southern portion of the vortex at 750 m indicated that the storm system still possessed the ability to generate new regions of strong vorticity. In that regard, while the tornado may have dissipated, the vorticity associated with the mesovortex was simply weakened, broadened, and elongated. It remained available to help create new circulations as the storm system moved outside the dual-Doppler domain. The 0544 UTC analysis suggests that two new mesovortices (Orlanski 1975; Fujita 1981) were attempting to develop

| 05:37 UTC | Tilting, SR-Wind, ω_H |

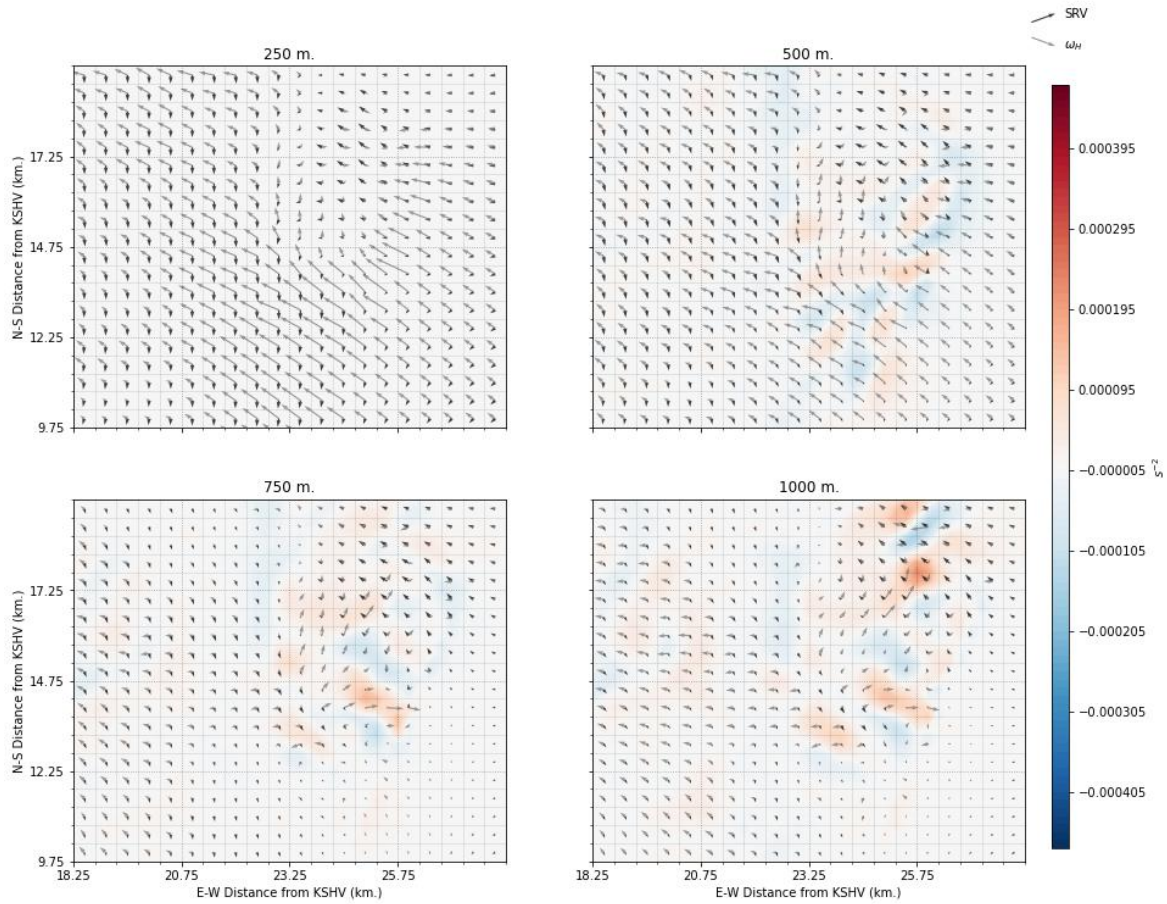


Figure 5.21: As in *Figure 5.17*, but for 0537 UTC, when the mesovortex was in its weakening stages.

| 05:44 UTC | ζ & w |

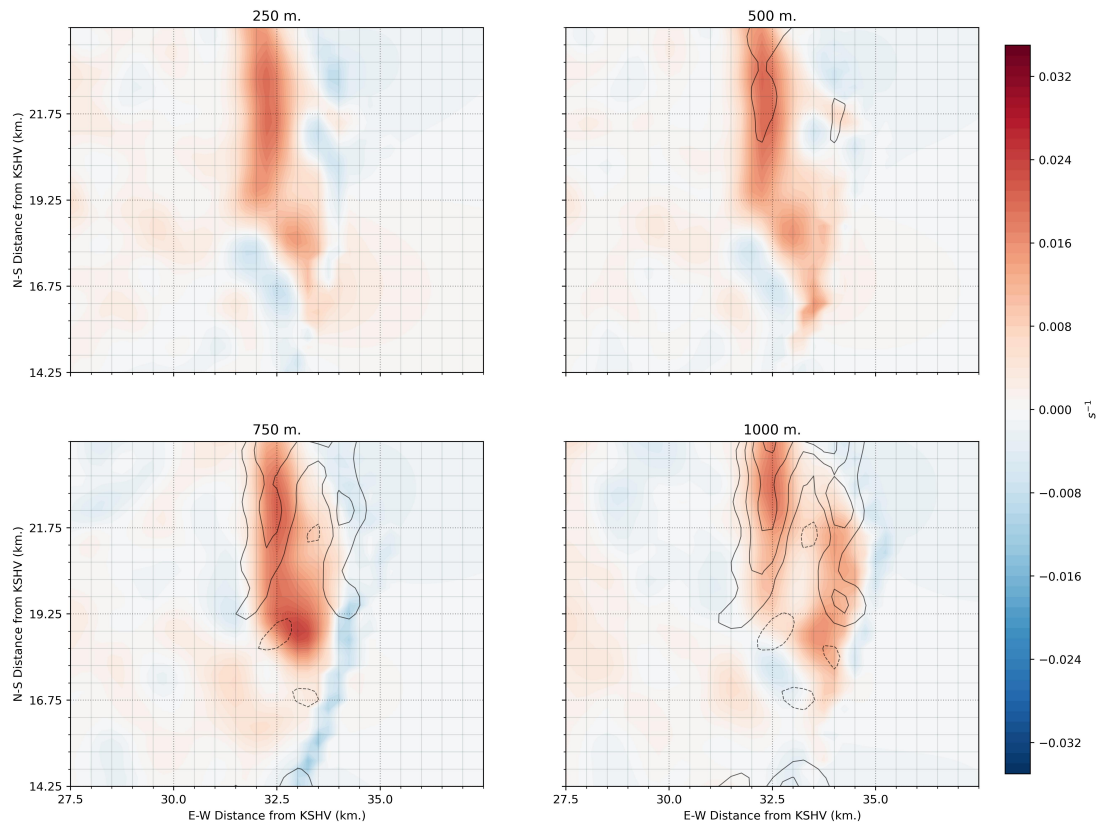


Figure 5.22: As in *Figure 5.20*, but for the decaying period of the vortex at 0544 UTC.

along the leading edge of the QLCS, taking advantage of the elevated, preexisting low level vorticity.

5.2 Mesovortex #2

5.2.1 Pre-Tornadic Stage

In contrast to the first mesovortex analyzed in this study, the second mesovortex was located squarely in the dual-Doppler domain created between SMART-R1 and SMART-R2. This geometry allowed for well-resolved wind retrievals over the entire lifecycle of the mesovortex as it intensified, produced a tornado, and began to weaken. The dynamics associated with this mesovortex are objectively weaker than those observed for the vortex in *Section 5.1* but were still intense enough to produce severe weather.

The analysis begins at 0536 UTC, about six minutes prior to the formation of an EF0 tornado near Sarepta, LA. At 0536 UTC, the mesovortex was in a mature stage of its lifecycle with vorticity (*Figure 5.23*) in the lowest 500 m already concentrated into a roughly 2 km by 2 km area with peak magnitudes of just over $2 \times 10^{-3} \text{ s}^{-1}$. Unfortunately, we were unable to observe the initial development of this particular mesovortex. Above this layer, vorticity magnitudes decreased slightly to 1 km altitude. The vortex was vertically oriented in the lowest 750 m, but exhibited a distinct tilt eastward between 750 m and 1 km before again becoming vertically aligned between 1 and 2 km altitude (*Figure 5.24*). The negative vertical gradient in vertical vorticity below 1 km may have just recently developed as an occlusion downdraft (Klemp and Rotunno 1983) was not yet evident in the analysis.

Both an updraft and downdraft were located in close proximity to the center of the vortex above 500 m altitude. However, vertical motions at the vortex's altitude were still relatively weak with vertical draft speeds increasing slightly from 3 m s^{-1} below 1 km to about 6 m s^{-1} by 2 km. The main relevance of the updraft is that it was embedded in the core of the vortex and contributed to producing some weak positive vorticity stretching above 750 m (not shown). Tilting on the other hand, was minimal due to the lack of significant gradients in vertical motion around the mesovortex (not shown).

| 05:36 UTC | ζ & W |

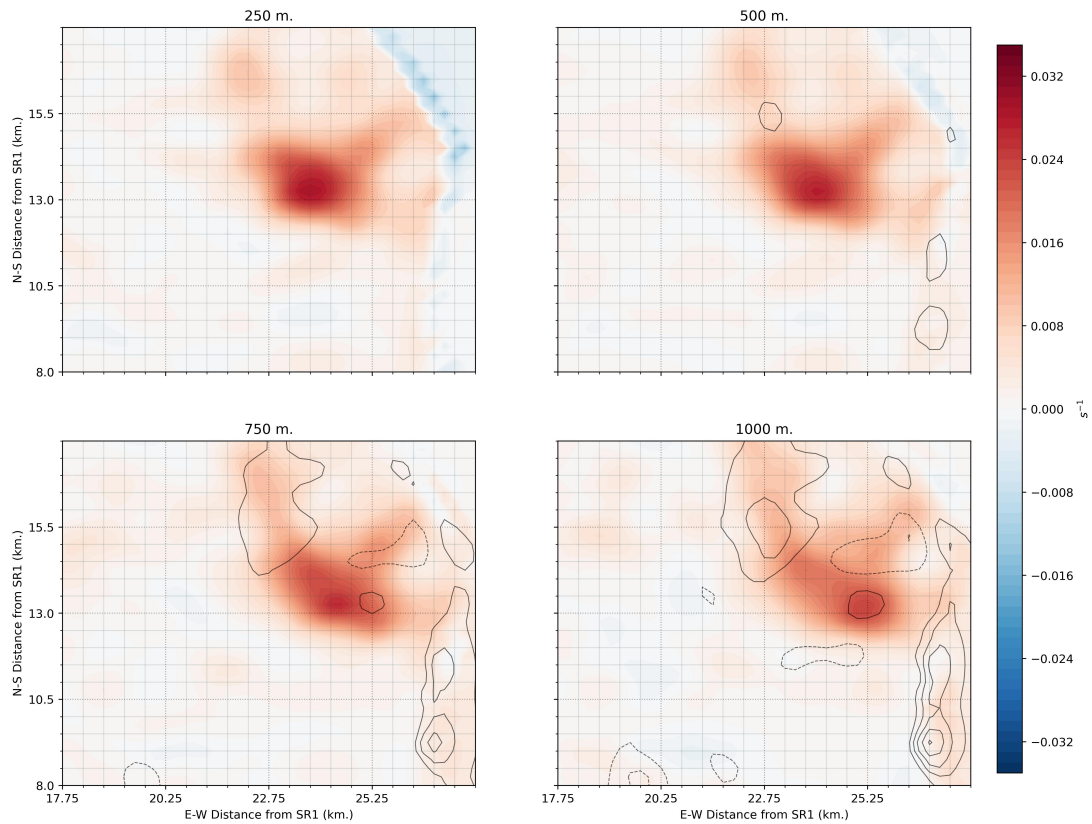


Figure 5.23: Vorticity (color fill) and black vertical motion contours every $2.5 m s^{-1}$ (solid contours represent updrafts; dashed contours represent downdrafts) in the vortex region at 0536 UTC. Heights in this layer range from 250 m to 1 km AGL.

| 05:36 UTC | ζ & W |

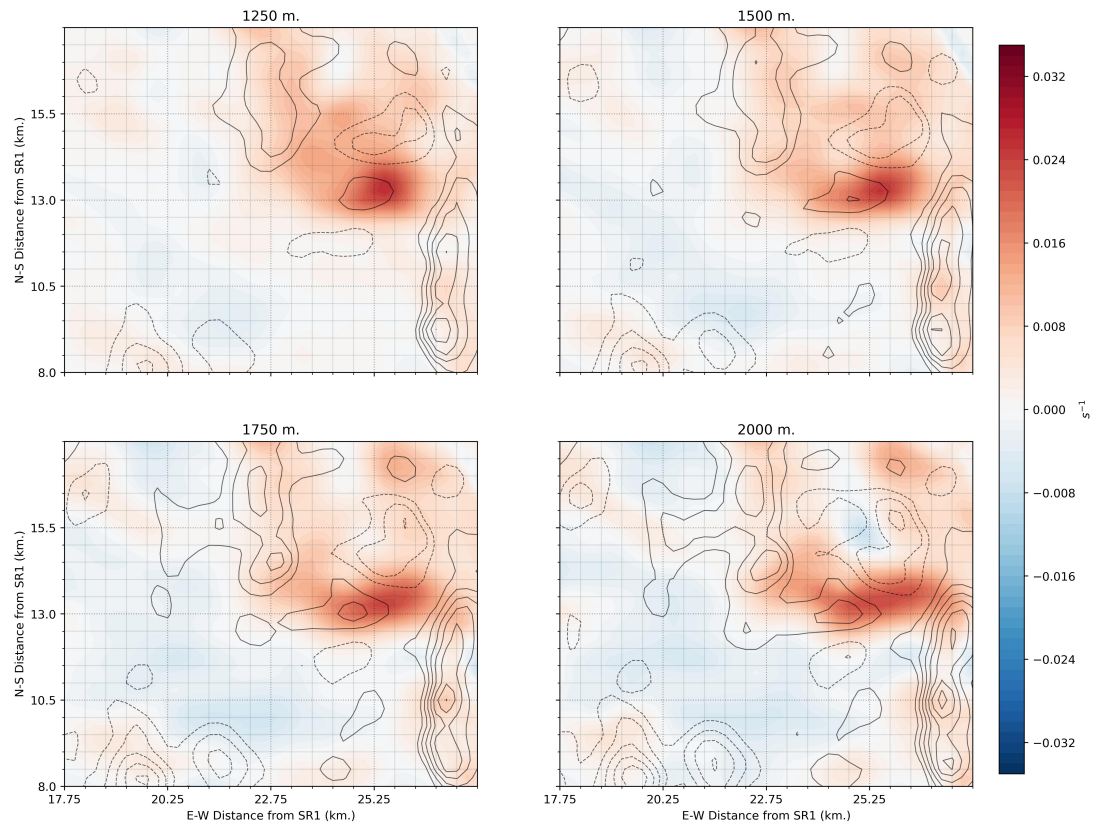


Figure 5.24: As in *Figure 5.23*, but for 1.25 to 2 km layer.

Between 0536 and 0538 UTC, vorticity below 1 km (*Figure 5.25*) remained at about the same intensity but then decreased above 1 km altitude (*Figure 5.26*). More importantly, the vortex was considerably more vertically aligned through the lowest 1.5 km. Above 1.5 km altitude, the vortex became less well-defined and was embedded within a northeast-southwest oriented band of vorticity near the leading edge of the convective line. While the vortex was not well-separated above 1.5 km, there was a small updraft that increased in strength with height, co-located with the vortex center. This co-location suggests that vorticity stretching would continue to deepen at the core of the mesovortex above 1 km altitude.

While the small updraft above 1 km is important to note, the feature that likely aided in further intensification of the vortex below 1 km was actually a downdraft that formed along the southern edge of the mesovortex at 750 m and 1 km (*Figure 5.25*). The downdraft-induced gradients of vertical motion coupled with the easterly oriented horizontal vorticity created two separate, but somewhat connected areas of positive vorticity tilting. One tilting region was identified in the southeastern portions of the vortex, and the other on the western periphery of the vortex (*Figure 5.27*).

Analysis of the crosswise and streamwise components of vorticity tilting revealed that a great proportion of the tilting occurring during this time was streamwise (*Figure 5.28*). Hence, just 4 minutes prior to tornado formation, the mesovortex below 1 km was ingesting streamwise vorticity on its southeastern flank in association with a convective downdraft and rear-to-front flow. Markowski and Richardson (2009) note that the tilting of horizontal vorticity by downdrafts is a leading proponent for the intensification of low-level vorticity in supercell thunderstorms. Similar dynamic processes are evidently at work in QLCS-associated circulations as well.

The vortex was also ingesting streamwise vorticity on its western flank where the front-to-rear flow was present in the northern part of the vortex. This front-to-rear environmental

| 05:38 UTC | ζ & W |

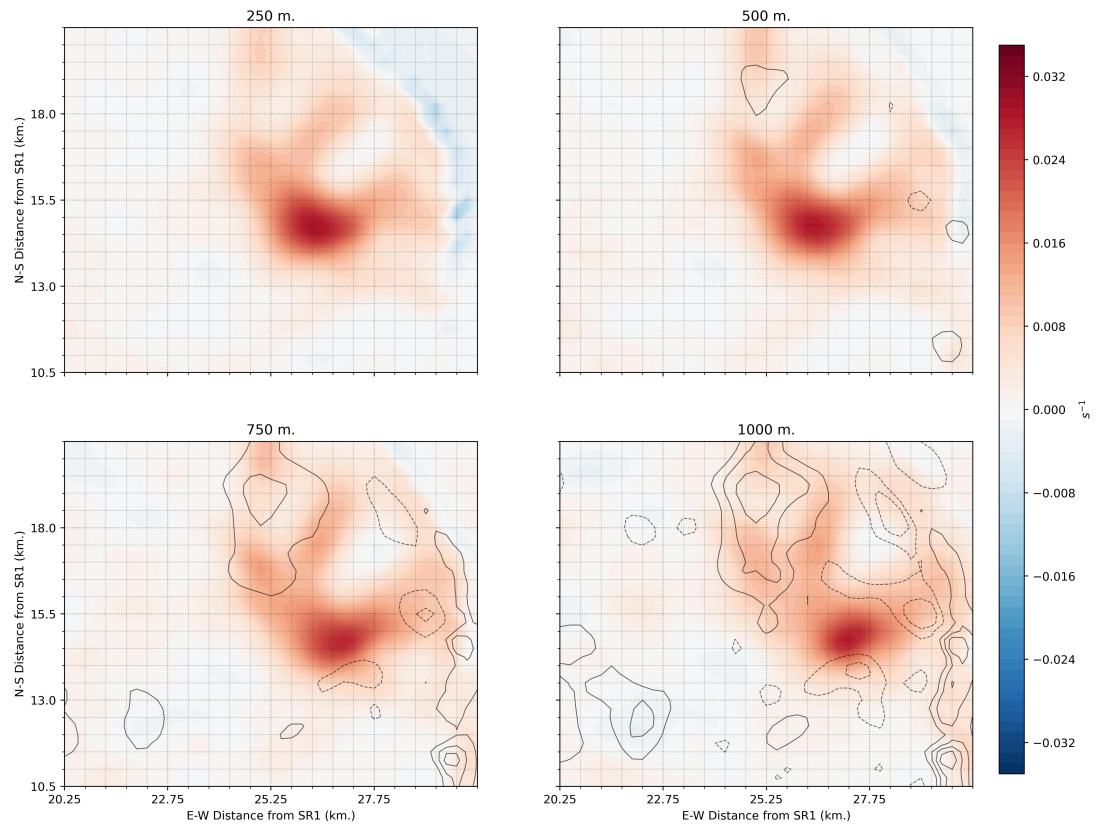


Figure 5.25: As in *Figure 5.23*, but for 0538 UTC.

| 05:38 UTC | ζ & W |

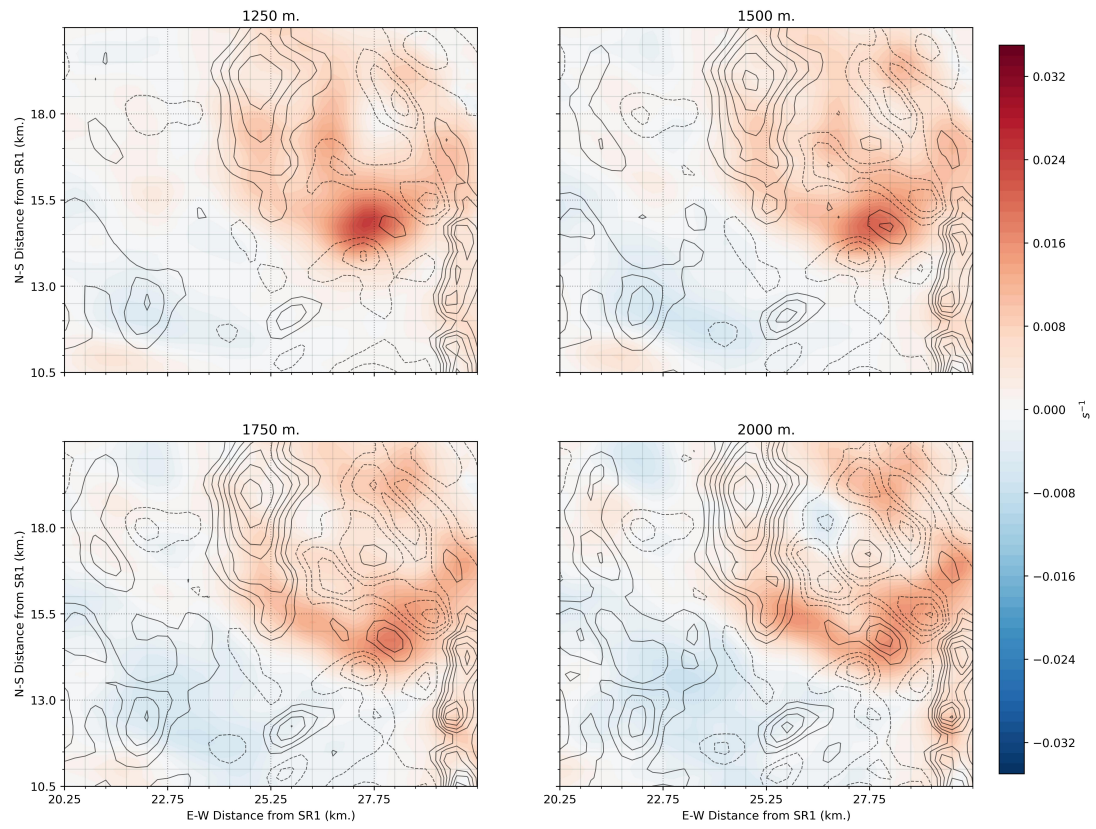


Figure 5.26: As in *Figure 5.25*, but for the 1.25 to 2 km layer.

| 05:38 UTC | Tilting, SR-Wind, ω_H |

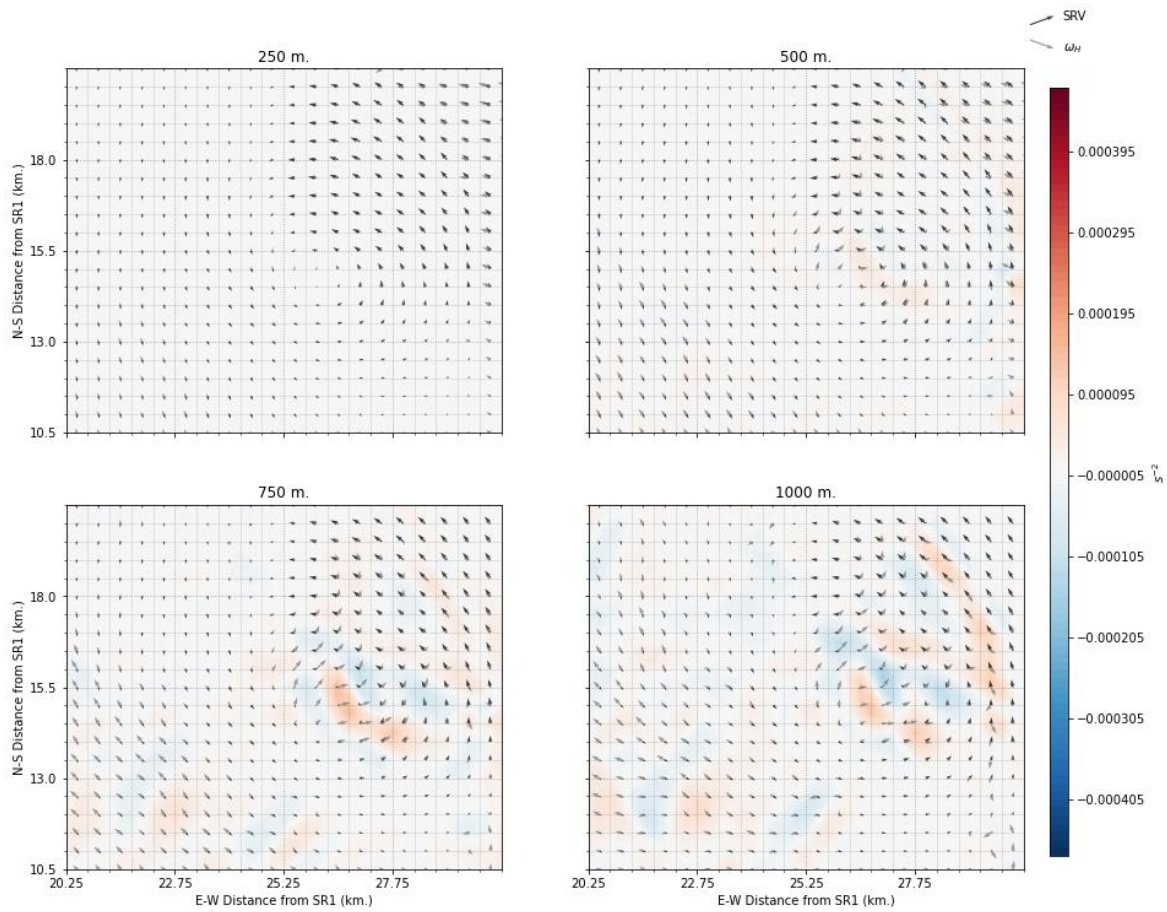


Figure 5.27: The 250 m to 1 km altitude 0538 UTC total vorticity tilting term magnitude (color fill) with storm-relative wind vectors (black arrows), and horizontal vorticity (ω_H) vectors (gray arrows) overlaid.

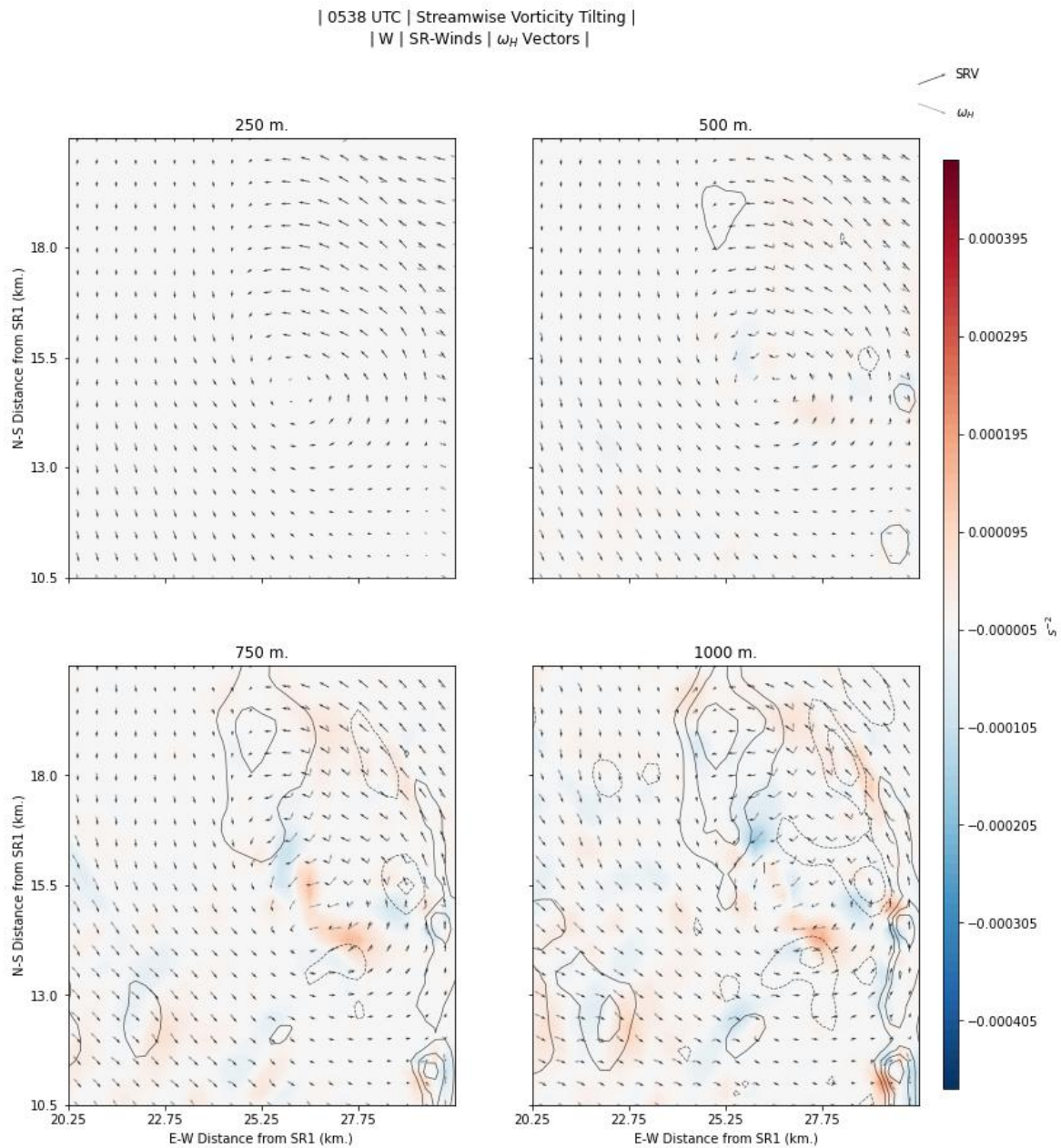


Figure 5.28: The 250 m to 1 km altitude streamwise vorticity tilting component (color fill) with vertical velocity contours in black (solid contours represent upward motion; dashed contours represent downward motion), storm-relative wind vectors (black arrows), and horizontal vorticity (ω_H) vectors (gray arrows) overlaid.

inflow was related to the inflow notch described in *Section 4.2*. The horizontal vorticity of the inflow was initially oriented northeastward. There was an abrupt transition to a more eastward orientation of horizontal vorticity in the narrow zone of positive streamwise tilting on the western flank of the vortex at 750 m. As was the case before, relevant tilting mechanisms likely responsible for intensifying the vortex at low levels is occurring on the horizontal scale of 500 m to 2 km in a shallow layer below 1 km altitude.

In contrast to the modest tilting values, the vorticity stretching term at 0538 UTC was weak. Therefore, the primary intensification mechanism for the low level mesovortex prior to tornadogenesis was the streamwise tilting of horizontal vorticity induced by a downdraft on the southern flank of the vortex.

Additional analyses of the vortex region just before tornadogenesis confirm the role of accelerating rear-inflow enhanced convergence in intensifying the mesovortex. Similar findings were made in mesovortex #1, but were harder to effectively analyze due to the coarse temporal resolution and location of the mesovortex in the dual-Doppler baseline. *Figure 5.29* shows that two discrete regions of enhanced convergence exist at low levels (i.e. 500 m) in the mesovortex region. One of these regions is located more than three kilometers away from the center of vorticity and likely had no effect on the circulation's lifecycle. The second maximum, however, was located between the interface of the updraft, reflectivity maximum, horizontal wind maxima, and the mesovortex circulation (near [X,Y]: [24.75 km, 15.75 km] in (c); [X,Y]: [26.75 km, 17.25 km] in (d)).

It is likely that the enhanced convergence precipitated by the downburst led to the increase in mesovortex strength, inducing/intensifying low level updrafts in vicinity of the circulation just before tornadogenesis (i.e. 0541 UTC) in a manner similar to Schenkman et al. (2012). Increased updraft intensity at low levels would have increased the stretching term in the vorticity tendency equation, intensifying vorticity in the circulation considerably and leading to tornadogenesis shortly thereafter (this intensification of the stretching term

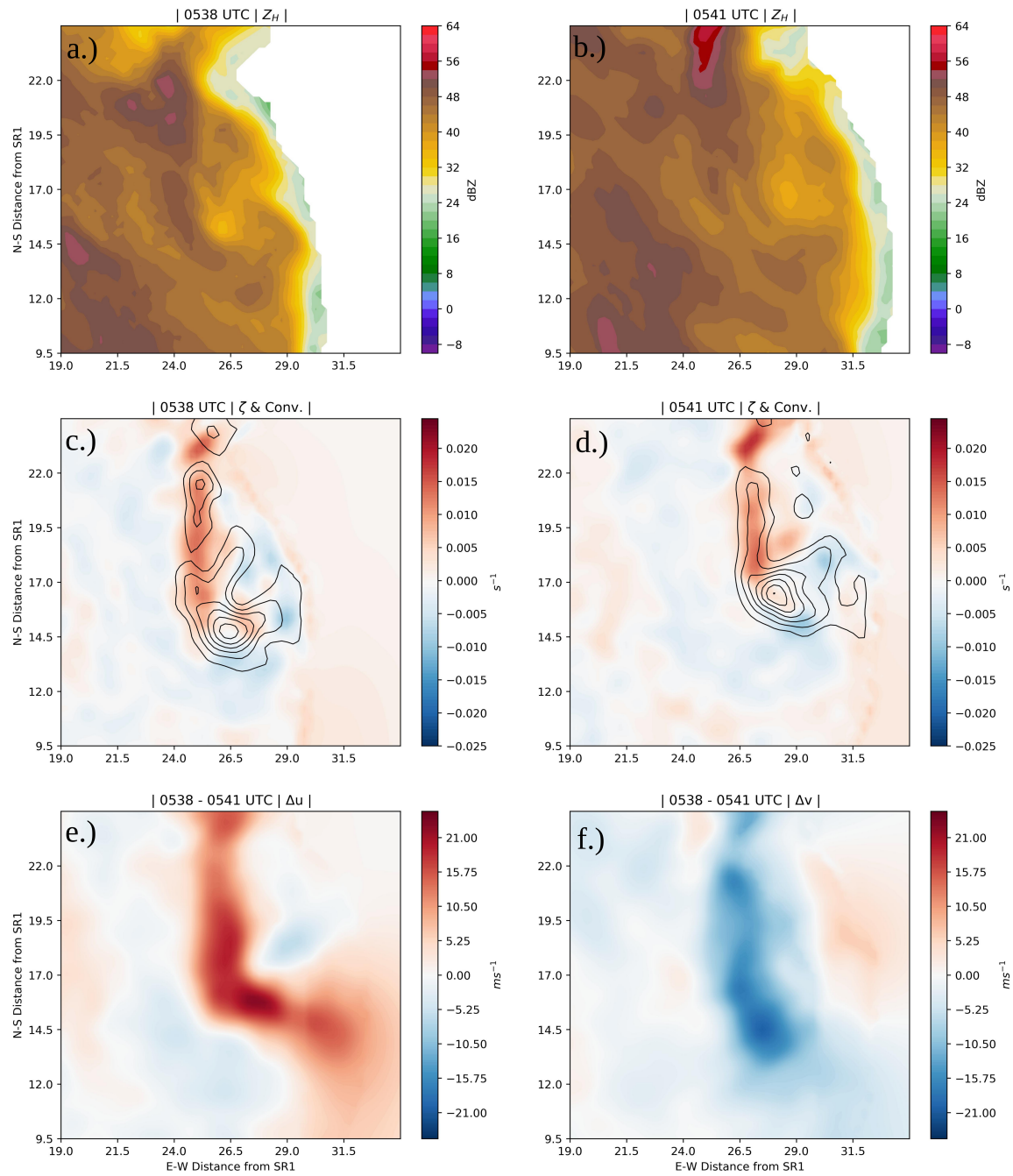


Figure 5.29: Mesovortex region reflectivity (a, b), convergence (color fill) and vertical vorticity (line contours) (c, d), change in zonal wind between 0538 and 0541 UTC (e), and change in meridional wind between 0538 and 0541 UTC (f) at 500 m. In (c) and (d), red colors indicate convergence magnitude and blue colors indicate divergence magnitude.

was indeed observed, and will be discussed in *Section 5.2.2*). Given the timing of the intensification of these features with respect to the mesovortex undergoing tornadogenesis, it is plausible that this type of process could be behind the intensification of mesovortices within the QLCS in this event.

Just after the radar reflectivity peaks at low levels and begins to decrease, values of both Δu and Δv fall considerably, leading to a decrease in convergence as well. Hence, the burst of low-level momentum associated with the reflectivity core reaching the surface was short-lived, but had an important role in the intensification of the low-level vorticity field.

5.2.2 Tornadogenesis Stage

The EF0 tornado associated with mesovortex 2 reportedly formed around 0542 UTC, lasting until approximately 0548 UTC. Given that the actual time of formation could have been off by a minute or two, we consider the 0541 UTC analysis as being representative of the mesovortex structure during tornadogenesis.

By 0541 UTC the vorticity below 500 m had increased by nearly 50 percent, reaching peak values of $3 \times 10^{-2} s^{-1}$ (*Figure 5.30*). Above 500 m altitude, the vorticity actually weakened. In fact, the tornadic mesovortex was less intense at 750 m than another area of vorticity located just 2 to 3 km to the southeast (*Figure 5.31*). Regardless, the tornadic mesovortex was quite vertically oriented through the lowest 1.5 km of the vortex's structure.

The vertical motion field contained two features that were relevant to the low level tornadic mesovortex. The downdraft on the southern flank of the vortex was still present and had grown in size and intensity. However, a new updraft had also formed on the northwest side of the tornadic mesovortex. This updraft increased from $5 m s^{-1}$ at 500 m altitude to more than $15 m s^{-1}$ by 1.5 km. Technically, this newly-formed updraft was just a southern extension of a prior convective band located to the north and west of the mesovortex. The position of this new updraft relative to the mesovortex created strong gradients in vertical motion on the northwest side of the vortex that did not exist prior to tornadogenesis.

The newly-formed updraft introduced complexity to the influence of tilting on intensification of the tornadic mesovortex. Generally, the storm-relative inflow on the northern side of the vortex was dominated by negative tilting due to the updraft vertical motion gradients (*Figure 5.32*). Conversely, the rear-inflow portion of the circulation still contributed positive vertical vorticity tendencies due to the gradients in vertical motions in the vicinity of the downdraft. Hence, vorticity-laden air that was ascending in the environmental inflow branch of the circulation was subjected to some weakening in vorticity before stretching occurred. In contrast, the air descending in the rear-inflow had positive tilting to compensate for any

| 05:41 UTC | ζ & W |

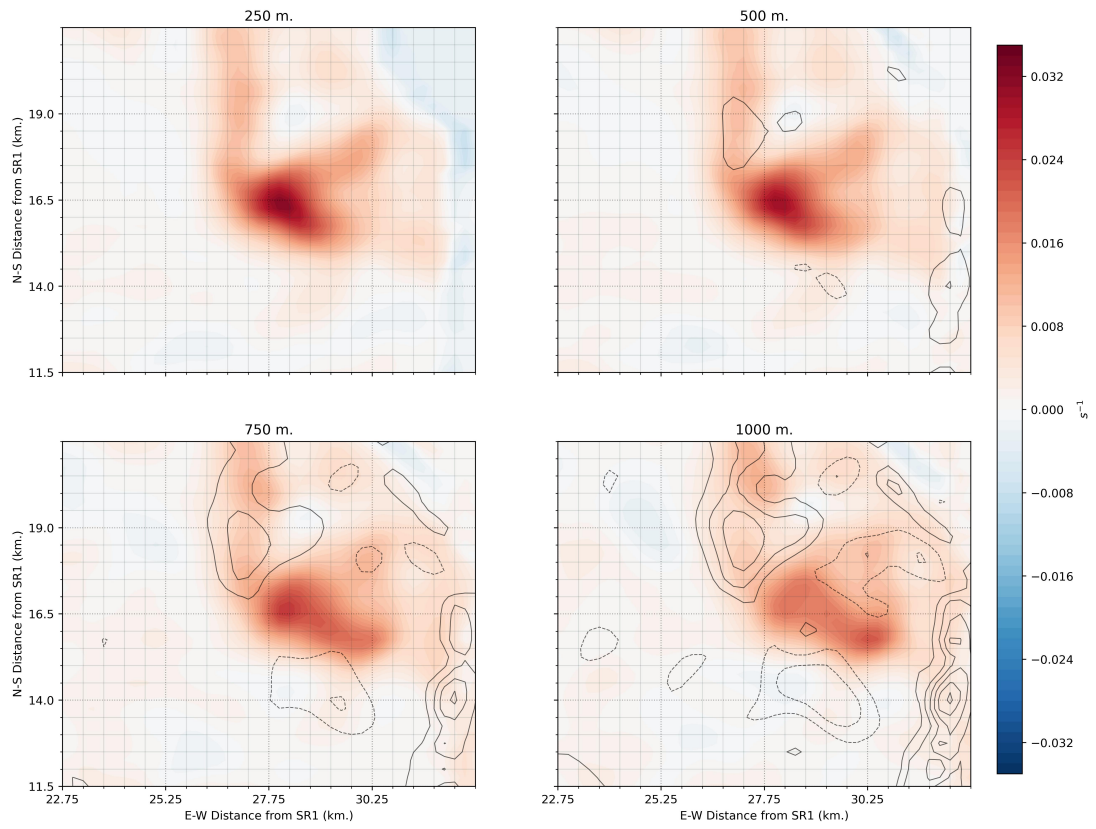


Figure 5.30: As in *Figure 5.25*, but for 0541 UTC.

| 05:41 UTC | ζ & W |

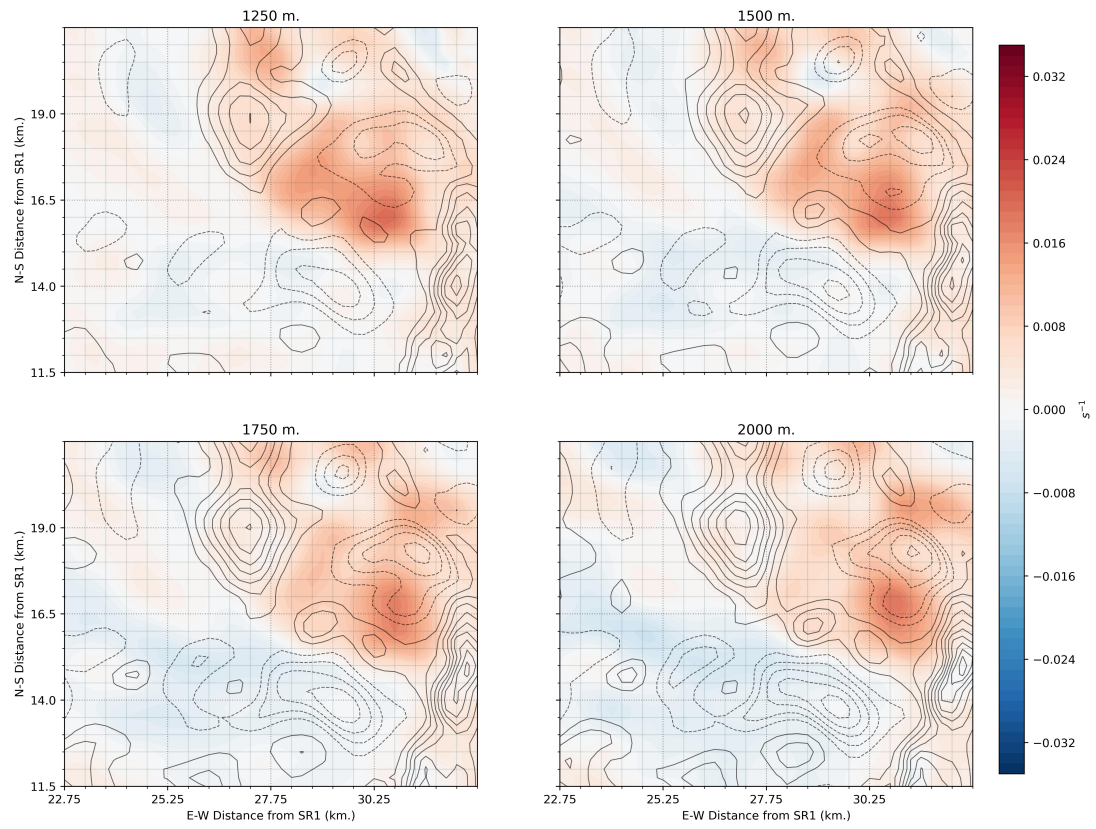


Figure 5.31: As in *Figure 5.26*, but for 0541 UTC.

vorticity losses resulting from negative stretching (*Figure 5.33*). Indeed, the southern portion of the mesovortex was already being subjected to significant negative stretching below 1 km altitude. Positive stretching was confined to two main areas: the northwestern portion of the vortex where the updraft had formed, and in a very small pocket on the southeastern side of the vortex core. This small pocket was likely on the scale of the tornado vortex, which could not be resolved in this analysis. In contrast to the time just before tornadogenesis where tilting was primarily streamwise, the tilting at 0541 UTC was dominated by the crosswise component (*Figure 5.34*). While crosswise tilting was occurring along the forward edge of the updraft, that tilting was mostly negated by collocated negative streamwise tilting (not shown) as the total tilting along the updraft was weak (*Figure 5.32*).

5.2.3 Tornadic Stage

According to reports, tornadogenesis occurred at 0542 UTC. The tornado associated with this mesovortex was short-lived and weak, ending at 0548 UTC and achieving a rating of EF0 on the Enhanced Fujita Scale. There are two wind retrievals during the tornadic stage of the mesovortex (0543 and 0546 UTC). *Figures 5.35* and *5.36* show the low-level vertical vorticity fields from those two dual-Doppler analyses.

While the vortex remained vertically oriented in the lowest 750 m during both analysis times, the magnitude of the vertical vorticity had significantly decreased. Peak values of vorticity at 250 m were ≈ 50 percent less than during tornadogenesis with the maximum being about $1.5 \times 10^{-2} \text{ s}^{-1}$ (*Figure 5.35*). By 0546 UTC, the low-level vorticity field had also become elongated (*Figure 5.36*), with a more intense maximum located about 1.5 km from the previous center of the tornadic mesovortex. It appears that the vortex was beginning to be disrupted by multicellular convection, which may have initiated from the occlusion downdraft (Lemon and Doswell 1979) that was evident in the core of the vortex at 0543

| 05:41 UTC | Tilting, SR-Wind, ω_H |

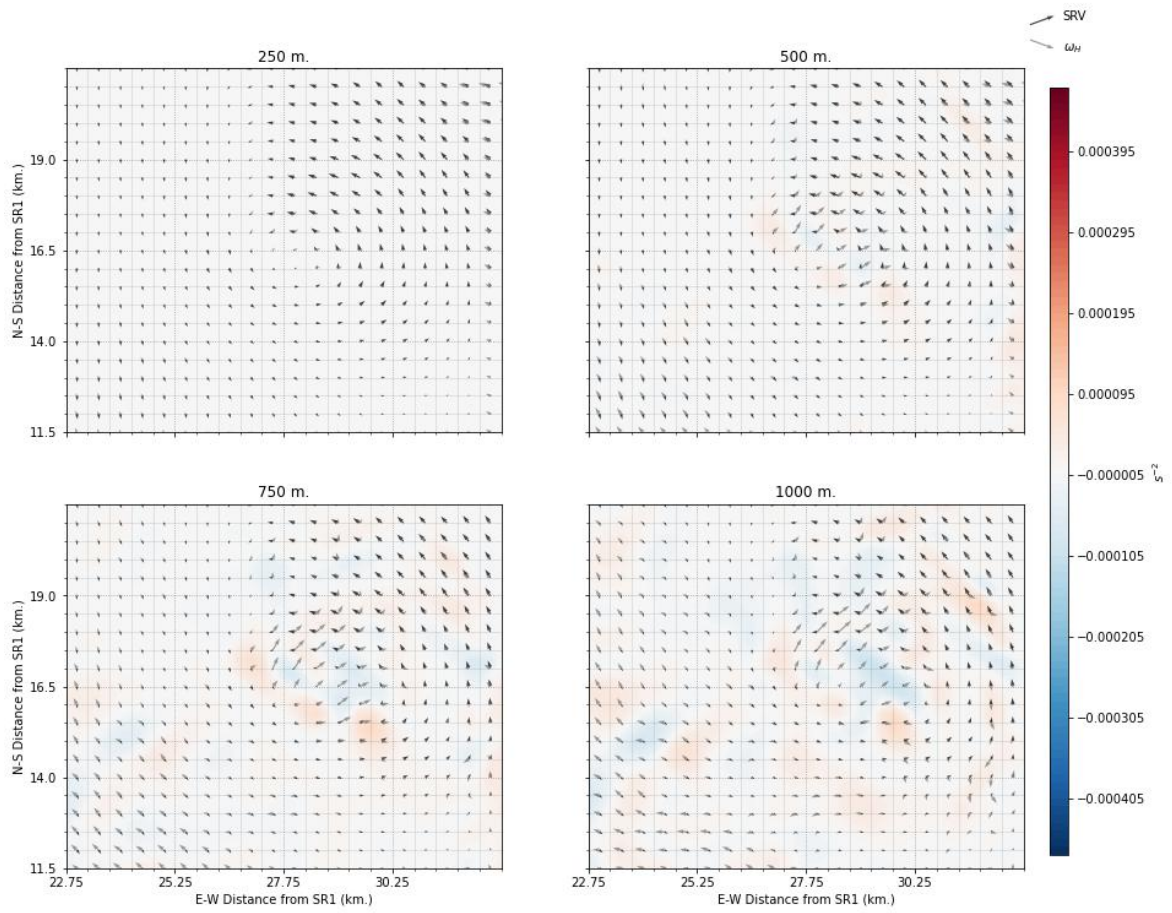


Figure 5.32: As in 5.27, but for 0541 UTC.

| 05:41 UTC | Stretching & ζ |

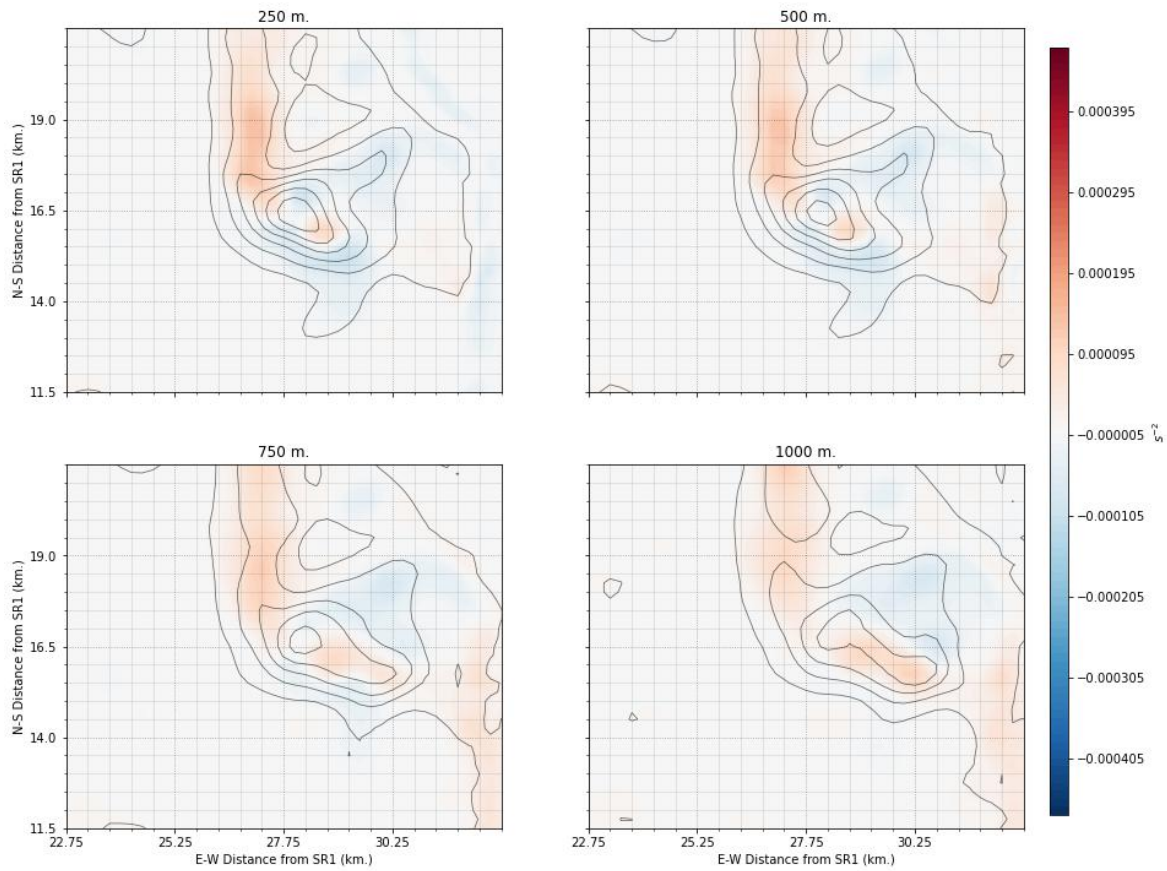


Figure 5.33: As in *Figure 5.16*, but for the second mesovortex at 0541 UTC.

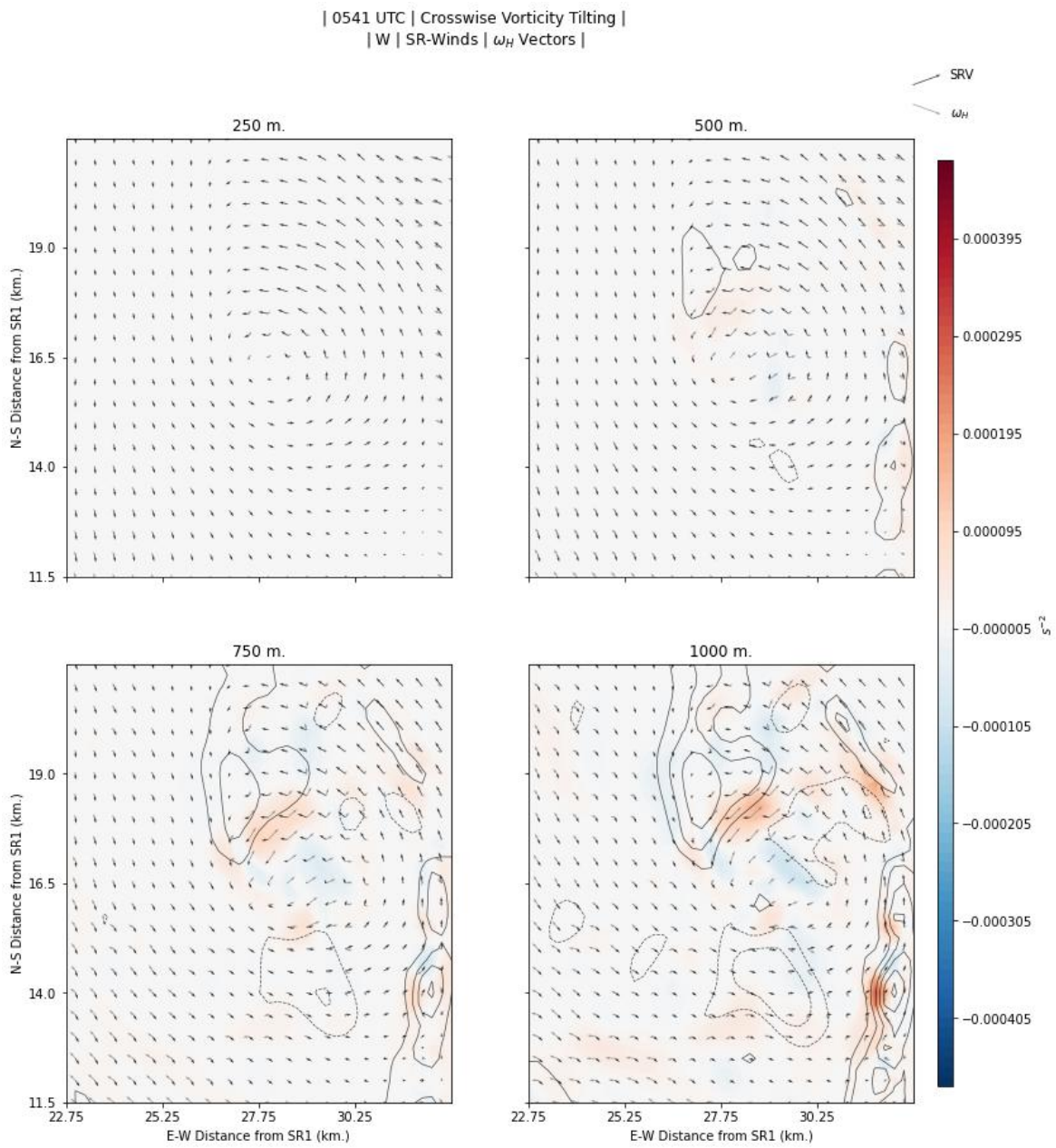


Figure 5.34: As in *Figure 5.28*, except for the crosswise vorticity component at 0541 UTC.

| 05:43 UTC | ζ & ω |

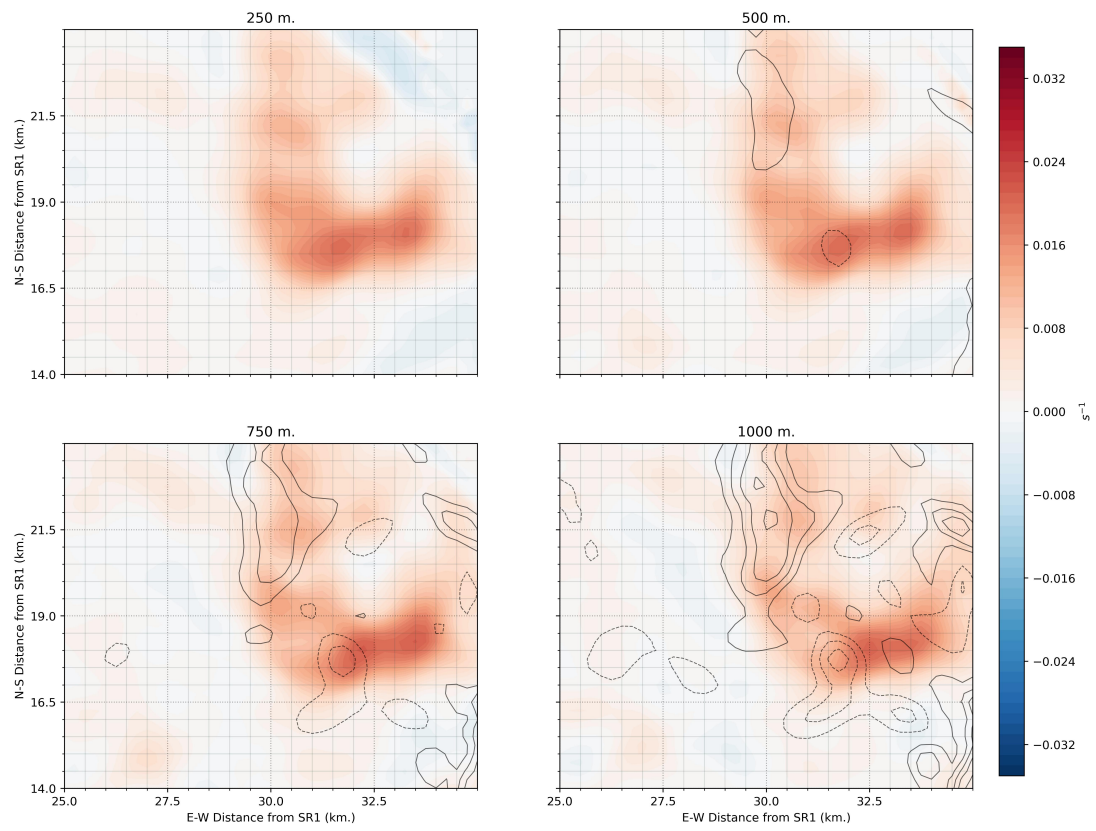


Figure 5.35: As in *Figure 5.30*, but for 0543 UTC.

| 05:46 UTC | ζ & W |

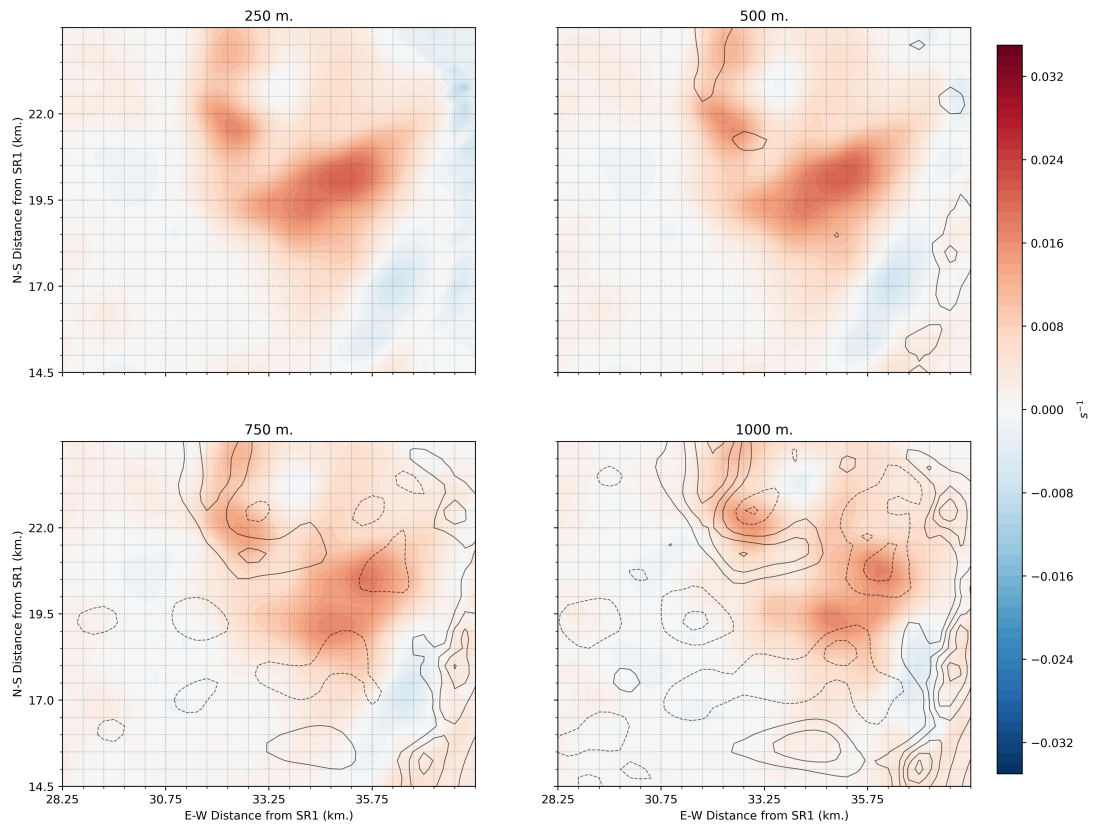


Figure 5.36: As in *Figure 5.35*, but for 0546 UTC.

UTC (*Figure 5.35*). Evidence of the influence of the occlusion downdraft on the breakdown of the vortex can be observed in the stretching field at 0543 UTC (*Figure 5.37*).

The occlusion downdraft in the center of the mesovortex resulted in the development of a distinct region of negative vorticity stretching within the vortex core at 0543 UTC (*Figure 5.37*). In contrast, the eastward extension of the vortex was in an area of positive stretching. That positive stretching acted to increase the vertical vorticity east of the vortex core, giving rise to the elongated nature of the vorticity at 0546 UTC.

Given that the vortex core during its tornadic stage was rapidly diminishing in strength and was becoming broader with time, it may be surprising that a tornado could be effectively sustained so rapidly after the vortex's formation. This apparent paradox may be explained by examining the tilting term at 0543 UTC (*Figure 5.38*).

Between 500 m and 1 km, there is a northwest-southeast oriented swath of positive vertical vorticity tendency centered near (X,Y): (32 km, 18 km). This swath is 4 km in length and around 1 km wide. Examination of this region of positive tilting indicates that it lies along the northeastern edges of the convective and occlusion downdrafts near the vortex center, but in an area that has near zero stretching. More importantly, the storm-relative flow vectors (black arrows) in *Figure 5.38* are nearly non-existent in this swath. Since both the horizontal and vertical motions are quite weak, the air is essentially trapped in an area of deep positive tilting tendency. This positive tilting could aid in maintaining the tornado, assuming that it was located in that particular portion of the larger mesovortex.

Decomposing the tilting into crosswise and streamwise components (*Figures 5.39* and *5.40*) yielded that both components were contributing to the positive tilting region, with the crosswise component being more important at 500 and 750 m and the streamwise vorticity component being more important above 750 m. The occlusion downdraft was essential to establishing the gradients in vertical motion that resulted in the deep layer of positive tilting

| 05:43 UTC | Stretching & ζ |

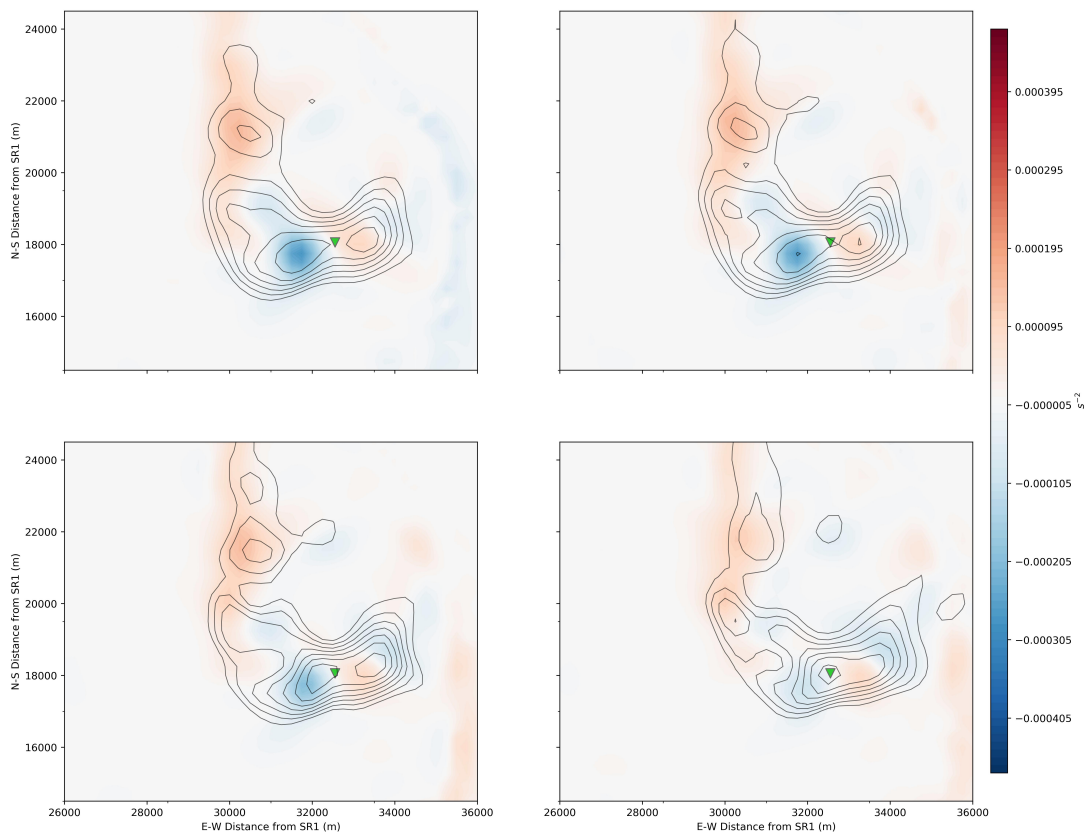


Figure 5.37: The stretching of vorticity term magnitude (color fill) and vorticity contours (in black) at 0543 UTC between 250 m and 1 km AGL. The green triangle indicates the approximate location of the tornado at analysis time.

| 05:43 UTC | Tilting, SR-Wind, ω_H |

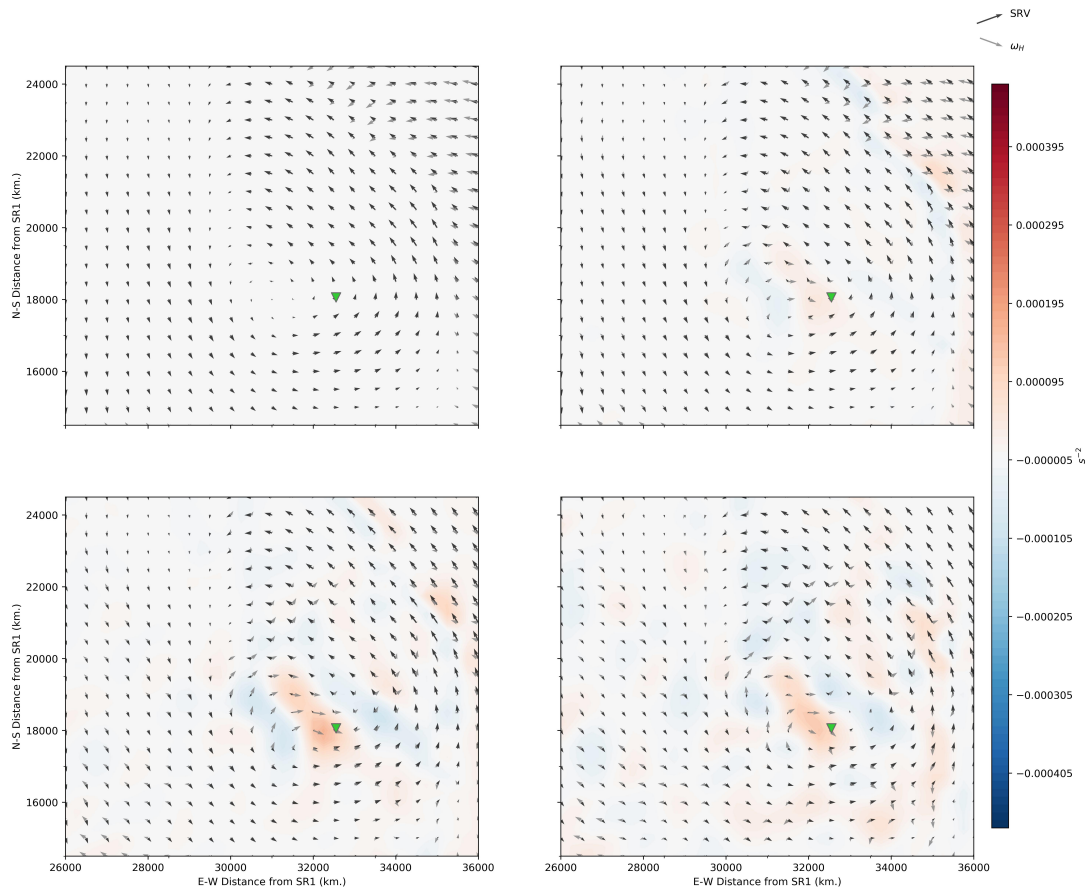


Figure 5.38: The 250 m to 1 km altitude 0543 UTC total vorticity tilting term magnitude (color fill) with storm-relative wind vectors (black arrows), and horizontal vorticity (ω_H) vectors (gray arrows) overlaid. The approximate location of the tornado at 0543 UTC is given by the green triangle.

within the quasi-stagnant flow region of the mesovortex. This sustained positive tilting mechanism likely helped to sustain the vorticity within the mesovortex, aiding it in supporting the smaller-scale tornado.

While tilting may have helped sustain the vorticity within the tornado for a brief period of time, the larger-scale mesovortex continued to weaken. Furthermore, the updraft and downdrafts within the vortex region had begun to decay. The updraft to the northwest of the circulation began to split into two separate entities, with the weaker of the two cores remaining in close proximity to the vorticity maximum, and the strongest core of upward vertical velocities translating away from the vortex to the north. The downdraft associated with the mesovortex began to weaken as well, declining in intensity with height and becoming displaced from the center of circulation by 1 to 2 km.

Vorticity stretching responded to the weakening updraft, as maximum positive stretching values below 1 km became displaced to the north of the vortex, maintaining their their coupling to the stronger updraft core (*Figure 5.41*). The tilting field followed a similar trend, with the term decreasing in magnitude substantially below 1 km (*Figure 5.42*). What positive tilting remained in the vortex region was weak and was confined to the northwestern side of the broad mesovortex. Mostly negative tilting tendencies were found within the stronger part of the mesovortex. Since both stretching and tilting terms were weak and the vertical motions supporting vortex maintenance had begun to drift away from the vortex core, the circulation entered into its dissipation stage.

5.2.4 Dissipating Stage

The low-level vorticity field evolved rapidly as the mesovortex weakened. Not only did the peak magnitudes decrease by another 40 percent in two minutes, but the structure of nearby vorticity centers changed as well (*Figure 5.43*). The strong negative stretching on the northeast side of the tornadic mesovortex rapidly diminished the vorticity center that had

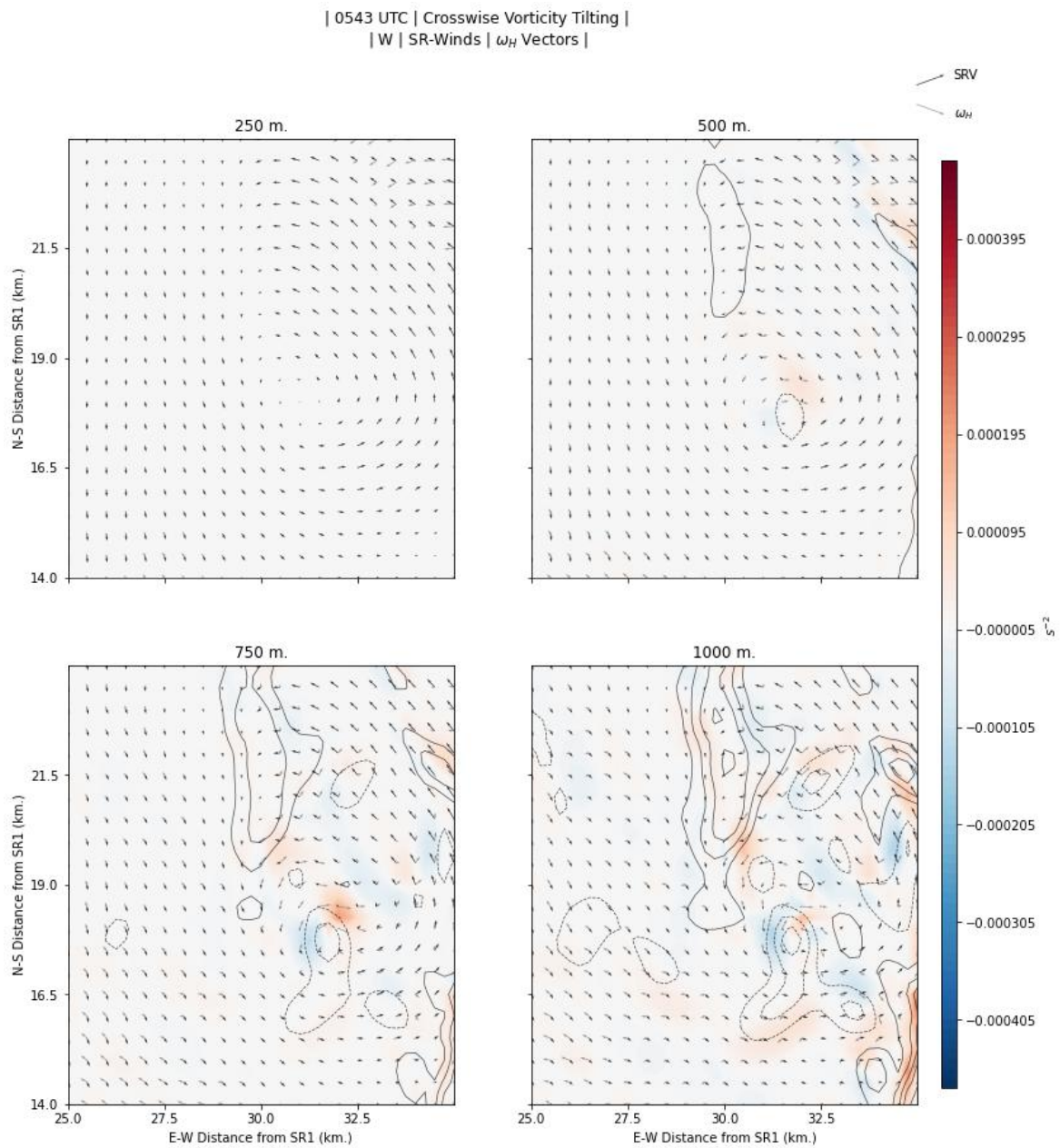


Figure 5.39: As in *Figure 5.34*, but for 0543 UTC.

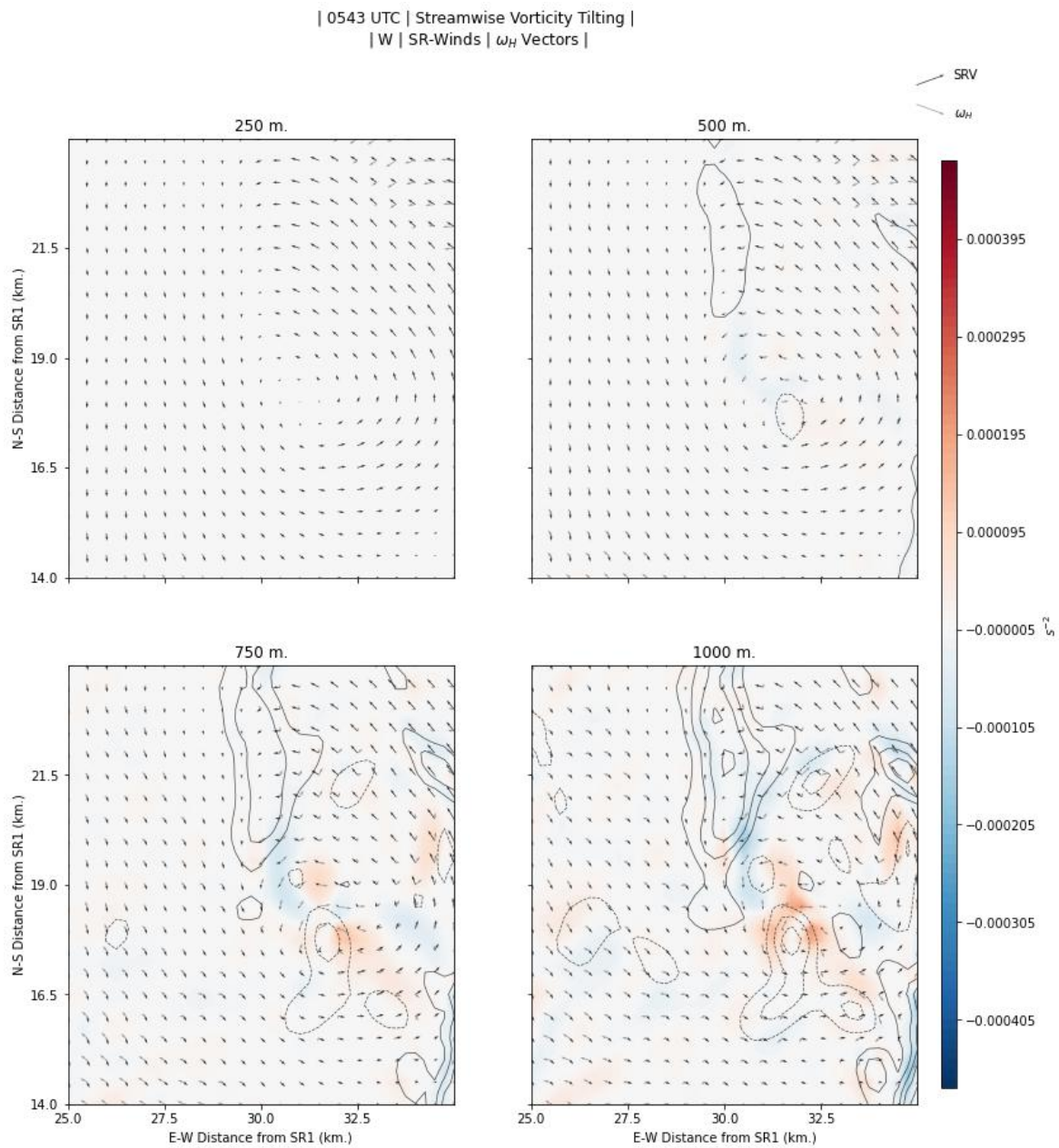


Figure 5.40: As in Figure 5.39, but for the streamwise component of vorticity tilting.

| 05:46 UTC | Stretching & ζ |

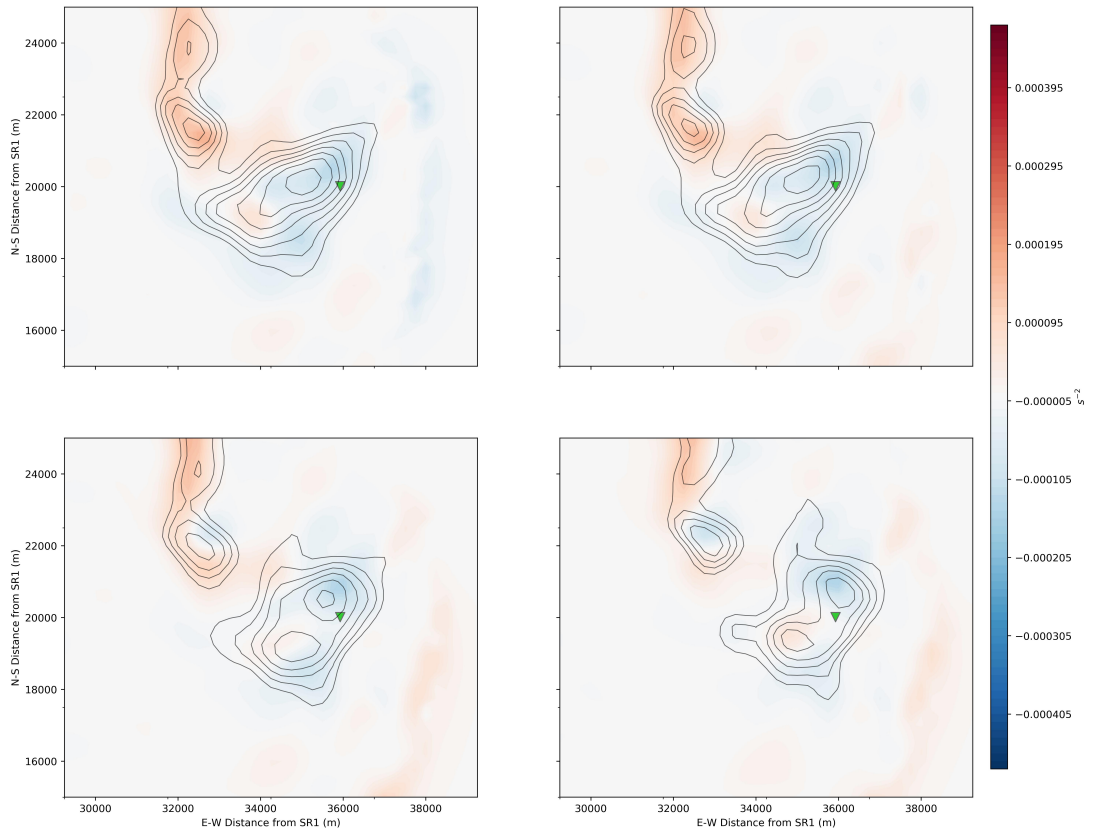


Figure 5.41: As in *Figure 5.37*, but for 0546 UTC.

| 05:46 UTC | Tilting, SR-Wind, ω_{sr} |

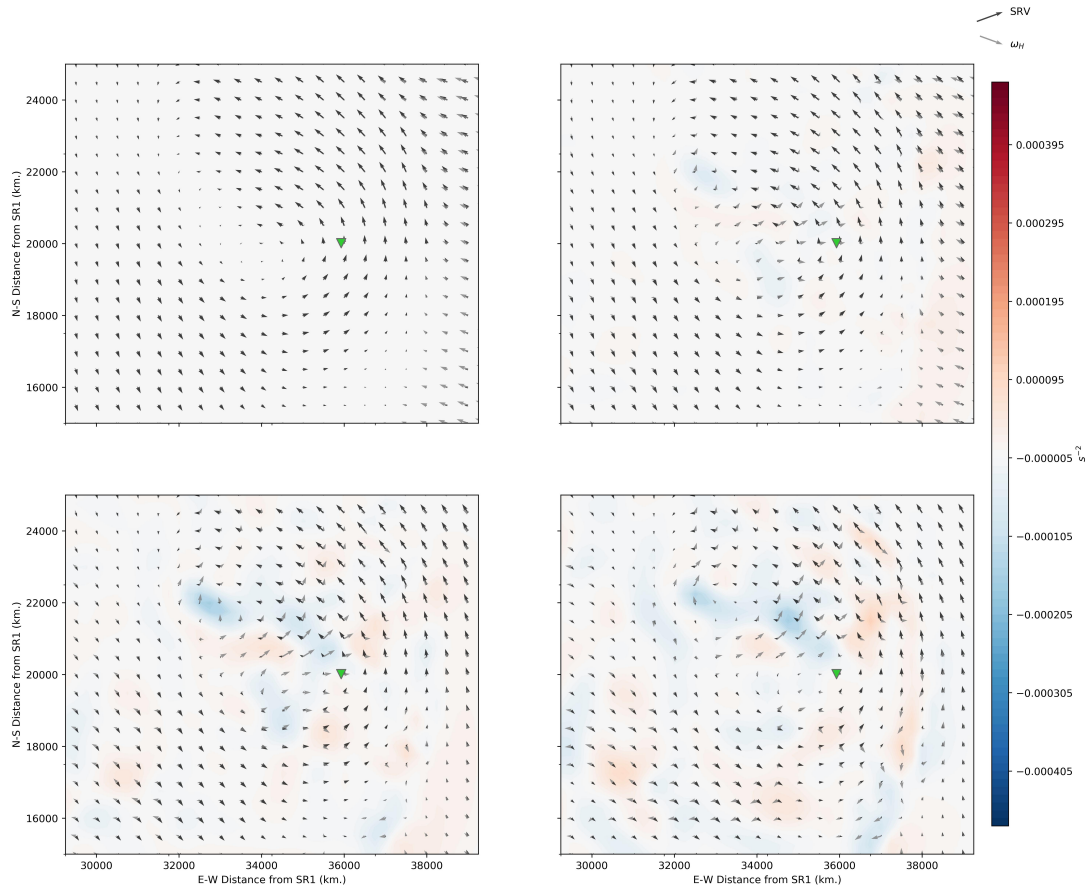


Figure 5.42: As in *Figure 5.38*, but for 0546 UTC.

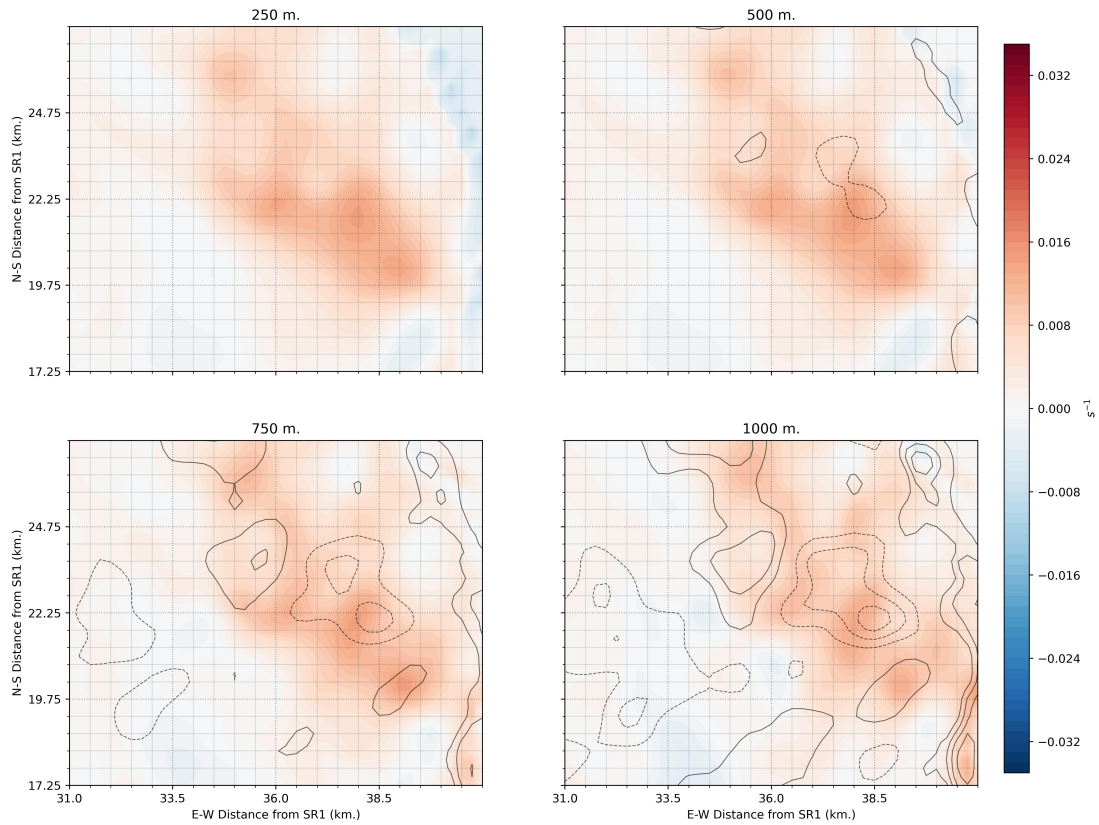


Figure 5.43: As in *Figure 5.36*, but for 0548 UTC.

briefly developed in the region. Instead of the northeast to southwest vorticity band observed at 0546 UTC, the vorticity was arranged from the southeast to the northwest by 0548 UTC.

A new vorticity center was found around 2 km to the southeast of the dissipating previously tornadic circulation, which was now located at (X,Y): (38 km, 21.75 km) at 250 m altitude, and a third distinct vorticity center was located about 2 km to the west-northwest. Another updraft pulse was occurring in the westernmost vorticity center while a downdraft, which increased in magnitude with height, was encroaching upon the previously tornadic vortex. A weaker updraft was found over the southeastern vorticity center.

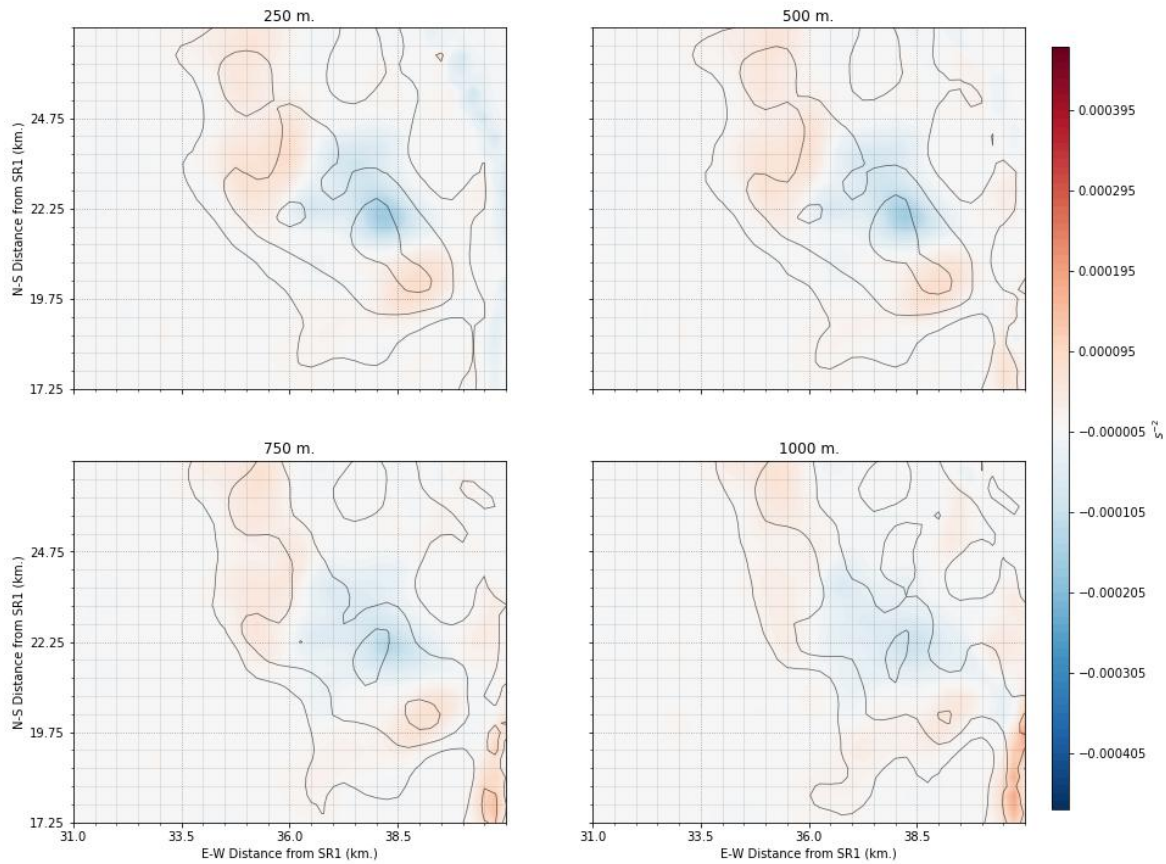


Figure 5.44: As in *Figure 5.41*, but for 0548 UTC.

The vertical motion field supported positive stretching in the two new vorticity centers, but only negative stretching tendencies over the primary vortex were observed (*Figure 5.44*). Hence, while the previously tornadic mesovortex was spun down, new vorticity centers were being created nearby. Tilting within the primary vortex was also negative, though positive tilting occurred in a fairly broad region within the inflow region northeast of the vortex center (*Figure 5.45*). Weak positive tilting at 750 m and 1 km was observed on the western edge of the southeastern-most vorticity center while very weak positive tilting was only observed at 750 m for the northwestern vorticity center.

| 05:48 UTC | Tilting, SR-Wind, ω_H |

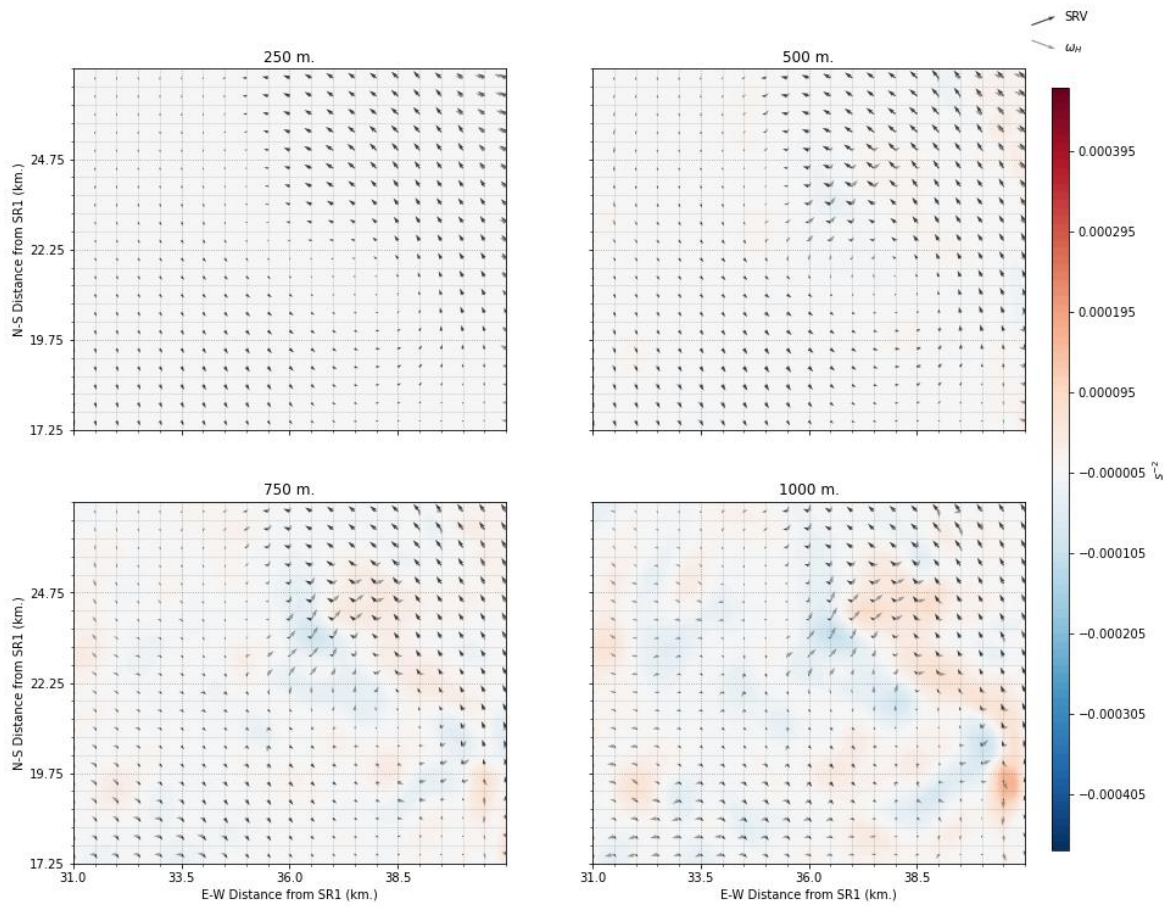


Figure 5.45: As in Figure 5.42, but for 0548 UTC.

Given the vorticity tendencies observed at 0548 UTC, it should be no surprise that the previously tornadic vortex [located at (X,Y): (38 km, 24.25 km) at 250 m in *Figure 5.46*] further diminished in strength by 0551 UTC while two new vorticity centers underwent moderate intensification. Accordingly, as the tornadic mesovortex weakened the vorticity field devolved into multiple, weak vorticity maxima. Vorticity in the vortex region had developed a diffuse, non-concentrated appearance. This decreasing trend in the vorticity magnitude continued until the end of the analysis. Furthermore, the vorticity field gradually acquired an elongated appearance, similar to the first mesovortex, as detailed in *Section 5.1*. Updraft and downdraft intensity had also decreased in the vortex region, as no vertical motions greater than 2.5 m s^{-1} were noted at 500 m. Only weak vertical velocities were observed at 750 m, in stark contrast to the values observed in previous analyses. Tilting and stretching terms (not shown) had become non-existent below 1 km. By 0556 UTC, little remnant vorticity was present in the previously tornadic mesovortex region, indicating that mesovortex 2 had decayed entirely.

| 05:51 UTC | ζ & W |

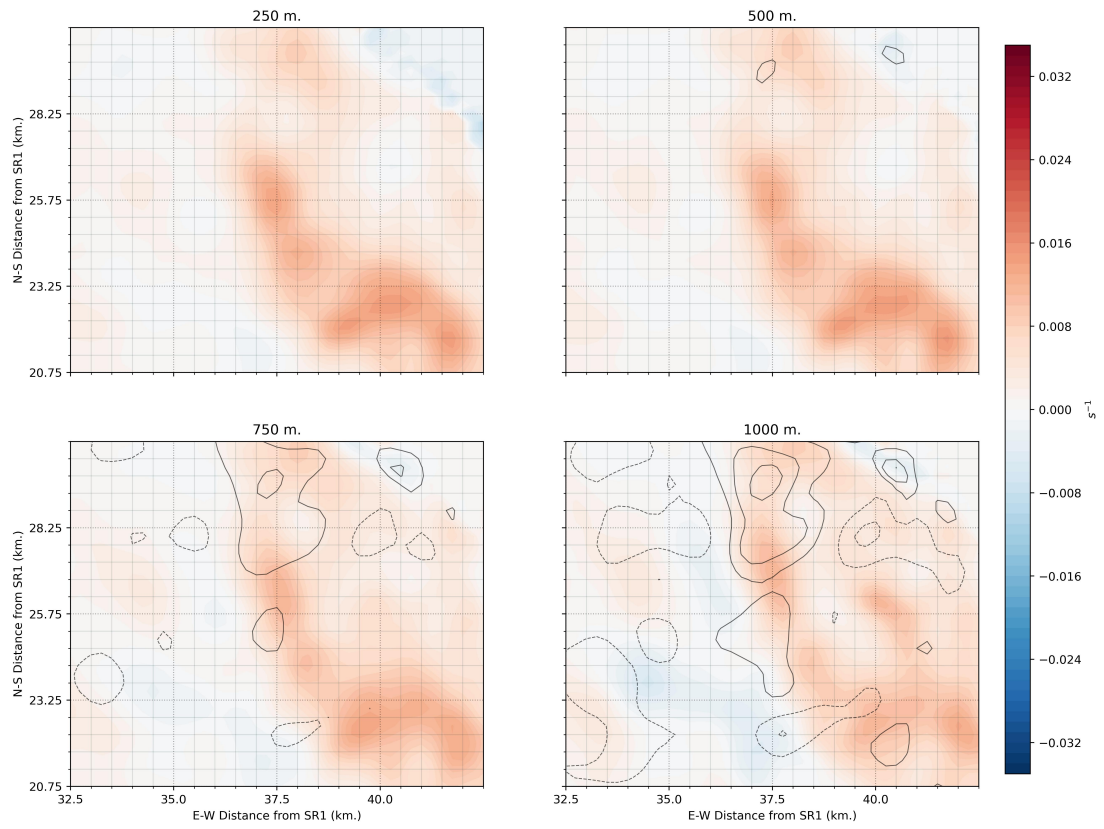


Figure 5.46: As in *Figure 5.43*, but for 0551 UTC.

Chapter 6

Conclusions & Future Work

There are a number of similarities in structure, intensification, and evolution of the two analyzed mesovortices. In both cases, the rear inflow jet played a critical role in establishing the bow-echo convective line pattern that preceded vortex formation. The RIJ associated with both line segments peaked in intensity just as the bow echo reflectivity pattern became evident in SMART-R1 and KSHV volume scans, attaining inbound velocities exceeding 30 m s^{-1} . This strong flow reinforced this bowing structure and induced the formation of strong thunderstorms along the leading edge of the line. Evidence of this process was noted in *Sections 4.1* and *4.2*, as reflectivity values peaked with the development of the convective bow echo structure.

In both cases, as the bow echo reached its maximum extent, mesovortices along the northern edge of the bow became apparent. As highlighted in the dual-Doppler analyses (i.e. *Figures 5.3, 5.23, 5.24, 5.25* and *5.26*) vorticity values at low levels were elevated, showing that rotation was present just above the surface. Strong updrafts were located to the north of the vortex in both QLCS regions, leading to the observed strong convection around 1-2 km to the northwest of the vortex. This enhanced convection in the vortex region eventually produced the reflectivity burst discussed in the single Doppler analysis sections.

The aforementioned convective bursts yielded downbursts in the vicinity of the mesovortices as the vortices propagated eastward with the convective line. *Figure 5.30* in *Section 5.2* details the presence of accelerating flow in the vortex region of the second mesovortex. The wind acceleration to the west and far southern portions of the plot is not associated with

the surge due to the mesovortex; rather, it is indicative of a surge occurring just to the south and east of the circulation. Similar accelerations were observed in one analysis time of the first vortex, but could not be effectively analyzed because of the location of the vortex along the KSHV/SMART-R1 baseline. The resulting enhancement of low level convergence in the vortex region precipitates the formation of a low level updraft to the north of the circulation at the area of locally high convergence (i.e. at 500 m, as in *Figure 5.29c,d*), increasing vertical vorticity stretching, which in turn drove further intensification of the vortex at low levels.

In the single Doppler data from both mesovortices, this intensification was marked by a sudden surge in the observed radial velocities observed behind/to the south southwest of the vortex and along the edge of the bow echo feature. The enhancement of convergence in the second vortex was followed soon thereafter by intensifying vorticity in the lowest 750 m of the dual-Doppler analysis from 0538 to 0541 UTC, and was noted as increasing gate-to-gate shear in single Doppler data across the same time frame. As the intensification continues, the rapidly maturing circulation would have induced a low pressure perturbation at its core (Markowski and Richardson 2010), resulting in the formation of an occlusion downdraft near the vortex core. The appearance of this feature marks the final intensification stage of the vortex, and tornadogenesis follows soon thereafter.

As the occlusion downdraft formed and tornadogenesis occurred, increased horizontal vorticity tilting began to occur with it. This tilted vorticity became trapped in the area of stagnant flow within the vortex and may have acted to briefly sustain the tornadic circulation when it appeared, if only briefly in the case of the second vortex. This brief intensification period leading up to, and just after tornadogenesis was well captured by the velocity field recorded by SMART-R1; additionally, vorticity tilting tendency was also well captured.

Elevations in the single Doppler data corresponding to the 750-1000 m AGL tilting maximum depict gate-to-gate velocities of the vortex of at least 30 m s^{-1} , showing that the vortex

was the most intense where tilting was maximized. The strength of the observed rotation also corresponded well to the observed dual-Doppler vorticity tendency forcing. Indeed, rotation was maximized at low levels where the stretching and tilting terms were maximized together and generated strong vertical vorticity tendency as a result. Conversely, in the middle levels of the circulation, the rotation was much less intense, corresponding with vertical levels where vorticity generation processes stagnated.

As the circulations progressed through their lifecycles, convection within the vortex regions of the QLCS became much more multicellular in nature. This multicellular storm initiation decreased the gradients in vertical motion necessary to induce positive vorticity stretching and disrupted the established updrafts and downdrafts in the vortex regions as new, weaker convective motions predominated. Within the single Doppler radar data, this increase in multicell convection was most easily noted in the reflectivity field as new convective cells began to appear ahead of, and in extremely close proximity to the mature mesovortex. After the appearance of multicellular convection in both vortex cases, the dual-Doppler data showed that the vortices began to broaden, weaken, and effectively cut off the support of the associated tornadic circulations. This process was further accelerated as downdrafts appeared near the vortex center in both cases, inducing negative vorticity stretching and decreasing vertical vorticity within the vortex itself.

SMART-R1 observations of the weakening phases of the vortices show the greatest weakening where this aforementioned negative vorticity stretching was present, at and above 1.3 deg. At subsequent times, the rotation decreased further, losing intensity as tilting processes at lower levels neared zero. As the vortices vanished from both single and dual-Doppler analyses, they became elongated and rotation broadened considerably, effectively marking the end of a vortex's lifecycle.

Future work should focus on building a robust number of cases of QLCS tornadogenesis, both confirm findings from this thesis and broaden understanding of QLCS tornadogenesis

as a whole. As convergence plays a pivotal role in the tornadogenesis process of QLCS tornadoes, verification of this processes enhancing convergence should be of high importance to future studies. Additional inquiries should also delve into cold pool intensity, convective downdraft-induced surges, mesoscale rear-to-front flow, and the RIJ as possible modulators of QLCS tornado production. Additionally, the appearance of the occlusion downdraft was notable and its role in vortex maintenance/intensification processes should investigated, especially given its pivotal role in generating the tilting necessary to sustain both mesovortices in this case study. Finally, dual-pole signifiers of increasing updraft intensity, presence of rainy downdrafts, and other information should be studied to attempt to provide meteorologists with all the tools necessary to understand the complex ways QLCSs generate tornadoes. Further in-depth studies of QLCS tornadoes should shed further light on processes influencing tornadic potential, gleaning valuable insight into a uniquely dangerous and mysterious type of natural hazard, saving lives and protecting property in the future.

Reference List

- Ashley, W. S., A. M. Haberlie, and J. Strohm, 2019: A climatology of quasi-linear convective systems and their hazards in the united states. *Weather and Forecasting*, **34** (6), 1605–1631, doi:10.1175/WAF-D-19-0014.1, URL <https://journals.ametsoc.org/doi/10.1175/WAF-D-19-0014.1>.
- Atkins, N. T., J. M. Arnott, R. W. Przybylinski, R. A. Wolf, and B. D. Ketcham, 2004: Vortex structure and evolution within bow echoes. part i: Single-doppler and damage analysis of the 29 june 1998 derecho. *Monthly Weather Review*, **132** (9), 2224–2242, doi:10.1175/1520-0493(2004)132<2224:VSAEWB>2.0.CO;2, URL [http://journals.ametsoc.org/doi/10.1175/1520-0493\(2004\)132<2224:VSAEWB>2.0.CO;2](http://journals.ametsoc.org/doi/10.1175/1520-0493(2004)132<2224:VSAEWB>2.0.CO;2).
- Atkins, N. T., C. S. Bouchard, R. W. Przybylinski, R. J. Trapp, and G. Schmocker, 2005: Damaging surface wind mechanisms within the 10 june 2003 saint louis bow echo during BAMEX. *Monthly Weather Review*, **133** (8), 2275–2296, doi:10.1175/MWR2973.1, URL <http://journals.ametsoc.org/doi/10.1175/MWR2973.1>.
- Atkins, N. T., and M. St. Laurent, 2009a: Bow echo mesovortices. part i: Processes that influence their damaging potential. *Monthly Weather Review*, **137** (5), 1497–1513, doi:10.1175/2008MWR2649.1, URL <http://journals.ametsoc.org/doi/10.1175/2008MWR2649.1>.
- Atkins, N. T., and M. St. Laurent, 2009b: Bow echo mesovortices. part II: Their genesis. *Monthly Weather Review*, **137** (5), 1514–1532, doi:10.1175/2008MWR2650.1, URL <http://journals.ametsoc.org/doi/10.1175/2008MWR2650.1>.

- Betten, D. P., M. I. Biggerstaff, and C. L. Ziegler, 2018: Three-dimensional storm structure and low-level boundaries at different stages of cyclic mesocyclone evolution in a high-precipitation tornadic supercell. *Advances in Meteorology*, **2018**, 1–24, doi:10.1155/2018/9432670, URL <https://doi.org/10.1155/2018/9432670>.
- Biggerstaff, M. I., and R. A. Houze, 1991: Midlevel vorticity structure of the 10–11 june 1985 squall line. *Monthly Weather Review*, **119** (3), 3066–3079, URL https://atmos.uw.edu/~beth/MG/PDFs/MWR91_bigg_midlevel.pdf.
- Biggerstaff, M. I., and Coauthors, 2005: The shared mobile atmospheric research and teaching radar: A collaboration to enhance research and teaching. *Bulletin of the American Meteorological Society*, **86** (9), 1263–1274, doi:10.1175/BAMS-86-9-1263, URL <https://journals.ametsoc.org/doi/10.1175/BAMS-86-9-1263>.
- Crum, T. D., and R. L. Alberty, 1993: The wsr-88d and the wsr-88d operational support facility. *Bulletin of the American Meteorological Society*, **74** (9), 1669–1687, doi:10.1175/1520-0477(1993)074<1669:TWATWO>2.0.CO;2, URL [http://journals.ametsoc.org/doi/10.1175/1520-0477\(1993\)074<1669:TWATWO>2.0.CO;2](http://journals.ametsoc.org/doi/10.1175/1520-0477(1993)074<1669:TWATWO>2.0.CO;2).
- Davis, C. A., and M. L. Weisman, 1994: Balanced dynamics of mesoscale vortices produced in simulated convective systems. *Journal of the Atmospheric Sciences*, **51** (14), 2005–2030, doi:10.1175/1520-0469(1994)051<2005:BDOMVP>2.0.CO;2, URL https://journals.ametsoc.org/view/journals/atsc/51/14/1520-0469_1994_051_2005_bdomvp_2_0_co_2.xml?tab_body=pdf.
- Flournoy, M. D., and M. C. Coniglio, 2019: Origins of vorticity in a simulated tornadic mesovortex observed during PECAN on 6 july 2015. *Monthly Weather Review*, **147** (1), 107–134, doi:10.1175/MWR-D-18-0221.1, URL <https://journals.ametsoc.org/doi/10.1175/MWR-D-18-0221.1>.

- Forbes, G. S., and R. M. Wakimoto, 1983: A concentrated outbreak of tornadoes, downbursts and microbursts, and implications regarding vortex classification. *Monthly Weather Review*, **111** (1), 220–236, doi:10.1175/1520-0493(1983)111<0220:ACOOTD>2.0.CO;2, URL [http://journals.ametsoc.org/doi/10.1175/1520-0493\(1983\)111<0220:ACOOTD>2.0.CO;2](http://journals.ametsoc.org/doi/10.1175/1520-0493(1983)111<0220:ACOOTD>2.0.CO;2).
- Fujita, T., 1955: Results of detailed synoptic studies of squall lines. *Tellus*, **7** (4), 405–436, doi:10.3402/tellusa.v7i4.8920, URL <https://www.tandfonline.com/doi/abs/10.3402/tellusa.v7i4.8920>.
- Fujita, T. T., 1981: Tornadoes and downbursts in the context of generalized planetary scales. *Journal of the Atmospheric Sciences*, **38** (8), 1511–1534, doi:10.1175/1520-0469(1981)038<1511:TADITC>2.0.CO;2, URL [http://journals.ametsoc.org/doi/10.1175/1520-0469\(1981\)038<1511:TADITC>2.0.CO;2](http://journals.ametsoc.org/doi/10.1175/1520-0469(1981)038<1511:TADITC>2.0.CO;2).
- Funk, T. W., K. E. Darmofal, J. D. Kirkpatrick, V. L. DeWald, R. W. Przybylinski, G. K. Schmocker, and Y.-J. Lin, 1999: Storm reflectivity and mesocyclone evolution associated with the 15 april 1994 squall line over kentucky and southern indiana. *Weather and Forecasting*, **14** (6), 976–993, doi:10.1175/1520-0434(1999)014<0976:SRAMEA>2.0.CO;2, URL [http://journals.ametsoc.org/doi/10.1175/1520-0434\(1999\)014<0976:SRAMEA>2.0.CO;2](http://journals.ametsoc.org/doi/10.1175/1520-0434(1999)014<0976:SRAMEA>2.0.CO;2).
- Gamache, J. F., and R. A. Houze, 1982: Mesoscale air motions associated with a tropical squall line. *Monthly Weather Review*, **110** (2), 118–135, doi:10.1175/1520-0493(1982)110<0118:MAMAWA>2.0.CO;2, URL https://journals.ametsoc.org/view/journals/mwre/110/2/1520-0493_1982_110_0118_mamawa_2_0_co_2.xml?tab_body=pdf.
- Helmus, J. J., and S. M. Collis, 2016: The python ARM radar toolkit (py-ART), a library for working with weather radar data in the python programming language. *Journal of*

- Open Research Software*, **4**, e25, doi:10.5334/jors.119, URL <http://openresearchsoftware.metajnl.com/articles/10.5334/jors.119/>.
- Houser, J. L., H. B. Bluestein, and J. C. Snyder, 2015: Rapid-scan, polarimetric, doppler radar observations of tornadogenesis and tornado dissipation in a tornadic supercell: The "el reno, oklahoma" storm of 24 may 2011. *Monthly Weather Review*, **143**, 2685–2710, doi:10.1175/MWR-D-14-00253.1, URL journals.ametsoc.org/journalsmwremwr-d-14-00253.1.pdf.
- Houze, R. A., 1981: Cloud clusters and large-scale vertical motions in the tropics. *Journal of the Meteorological Society of Japan*, **60** (1), 396–410, doi:10.2151/jmsj1965.60.1_396, URL https://www.jstage.jst.go.jp/article/jmsj1965/60/1/60.1_396/_article.
- Houze, R. A., M. I. Biggerstaff, S. A. Rutledge, and B. F. Smull, 1989: Interpretation of doppler weather radar displays of midlatitude mesoscale convective systems. *Bulletin of the American Meteorological Society*, **70** (6), 608–619, doi:10.1175/1520-0477(1989)070<0608:IODWRD>2.0.CO;2, URL [http://journals.ametsoc.org/doi/10.1175/1520-0477\(1989\)070<0608:IODWRD>2.0.CO;2](http://journals.ametsoc.org/doi/10.1175/1520-0477(1989)070<0608:IODWRD>2.0.CO;2).
- Houze, R. A., and P. V. Hobbs, 1982: Organization and structure of precipitating cloud systems. *Advances in Geophysics*, Vol. 24, Elsevier, 225–315, doi:10.1016/S0065-2687(08)60521-X, URL <https://linkinghub.elsevier.com/retrieve/pii/S006526870860521X>.
- Isaminger, M. A., 1988: A preliminary study of precursors to huntsville microbursts. **ADA200914 (ATC-153)**, URL <https://apps.dtic.mil/sti/citations/ADA200914>.
- Jorgensen, D. P., and B. F. Smull, 1993: Mesovortex circulations seen by airborne doppler radar within a bow-echo mesoscale convective system. *Bulletin of the American Meteorological Society*, **74** (11), 2146–2157, doi:10.1175/

1520-0477(1993)074<2146:MCSBAD>2.0.CO;2, URL [http://journals.ametsoc.org/doi/10.1175/1520-0477\(1993\)074<2146:MCSBAD>2.0.CO;2](http://journals.ametsoc.org/doi/10.1175/1520-0477(1993)074<2146:MCSBAD>2.0.CO;2).

Kessinger, C. J., P. S. Ray, and C. E. Hane, 1987: The oklahoma squall line of 19 may 1977. part i: A multiple doppler analysis of convective and stratiform structure. *Journal of the Atmospheric Sciences*, **44** (19), 2840–2865, doi:10.1175/1520-0469(1987)044<2840:TOSLOM>2.0.CO;2, URL [http://journals.ametsoc.org/doi/10.1175/1520-0469\(1987\)044<2840:TOSLOM>2.0.CO;2](http://journals.ametsoc.org/doi/10.1175/1520-0469(1987)044<2840:TOSLOM>2.0.CO;2).

Klemp, J. B., and R. Rotunno, 1983: A study of the tornadic region within a supercell thunderstorm. *Journal of the Atmospheric Sciences*, **40** (2), 359–377, doi:10.1175/1520-0469(1983)040<0359:ASOTTR>2.0.CO;2, URL https://journals.ametsoc.org/view/journals/atsc/40/2/1520-0469_1983_040_0359_asottr_2_0_co_2.xml?tab_body=fulltext-display.

Kuster, C. M., P. L. Heinselman, and T. J. Schuur, 2016: Rapid-update radar observations of downbursts occurring within an intense multicell thunderstorm on 14 june 2011. *Weather and Forecasting*, **31** (3), 827–851, doi:10.1175/WAF-D-15-0081.1, URL https://journals.ametsoc.org/view/journals/wefo/31/3/waf-d-15-0081_1.xml.

Lemon, L. R., and C. A. Doswell, 1979: Severe thunderstorm evolution and mesocyclone structure as related to tornadogenesis. *Monthly Weather Review*, **107** (9), 1184–1197, doi:10.1175/1520-0493(1979)107<1184:STEAMS>2.0.CO;2, URL https://journals.ametsoc.org/view/journals/mwre/107/9/1520-0493_1979_107_1184_steams_2_0_co_2.xml?tab_body=fulltext-display.

Markowski, P., and Y. Richardson, 2010: *Mesoscale Meteorology in Midlatitudes*. Advancing weather and climate science, Wiley-Blackwell, OCLC: ocn461269379.

Markowski, P. M., and Y. P. Richardson, 2009: Tornadogenesis: Our current understanding, forecasting considerations, and questions to guide future research. *Atmospheric Research*, **93** (1–3), doi:10.1016/j.atmosres.2008.09.015, URL <https://www.sciencedirect.com/science/article/pii/S016980950800255X?via%3Dihub>.

National Centers for Environmental Information, 2018: Storm data, and unusual weather phenomena with late reports and corrections. Tech. Rep. 6, National Centers for Environmental Information, 591 pp. URL <https://www.ncei.noaa.gov/pub/orders/IPS/IPS-B45AAD1B-766A-4D60-8946-A41AA89F4B9F.pdf>.

Newman, J. F., and P. L. Heinselman, 2012: Evolution of a quasi-linear convective system sampled by phased array radar. *Monthly Weather Review*, **140** (11), 3467–3486, doi:10.1175/MWR-D-12-00003.1, URL <http://journals.ametsoc.org/doi/10.1175/MWR-D-12-00003.1>.

Newton, C., 1960: Structure and mechanism of the prefrontal squall line. *Journal of the Atmospheric Sciences*, **7** (3), 210–222, doi:10.1175/1520-0469(1950)007<0210:SAMOTP>2.0.CO;2, URL https://journals.ametsoc.org/view/journals/atsc/7/3/1520-0469_1950_007_0210_samotp_2_0_co_2.xml?tab_body=pdf.

Nolen, R. H., 1959: A radar pattern associated with tornadoes. *Bulletin of the American Meteorological Society*, **40** (6), 277–279, doi:<https://doi.org/10.1175/1520-0477-40.6.277>, URL https://journals.ametsoc.org/view/journals/bams/40/6/1520-0477-40_6_277.xml.

NWS Shreveport, LA, 2018: April 13-14, 2018: Tornado outbreak. Tech. rep., National Weather Service. URL https://weather.gov/shv/event_2018-4-13_tornadoes.

Ogura, Y., and Y.-L. Chen, 1977: A life history of an intense mesoscale convective storm in oklahoma. *Journal of the Atmospheric Sciences*, **34** (9), 1458–1476, doi:10.1175/

- 1520-0469(1977)034<1458:ALHOAI>2.0.CO;2, URL https://journals.ametsoc.org/view/journals/atsc/34/9/1520-0469_1977_034_1458_alhoai_2_0_co_2.xml?tab_body=pdf.
- Ogura, Y., and M.-T. Liou, 1980: The structure of a midlatitude squall line: A case study. *Journal of the Atmospheric Sciences*, **37** (3), 553–567, doi:10.1175/1520-0469(1980)037<0553:Tsoams>2.0.CO;2, URL https://journals.ametsoc.org/view/journals/atsc/37/3/1520-0469_1980_037_0553_tsoams_2_0_co_2.xml?tab_body=pdf.
- Orlanski, I., 1975: correspondence. *Bulletin of the American Meteorological Society*, **56** (5), 527–534, doi:10.1175/1520-0477-56.5.527, URL <https://journals.ametsoc.org/doi/10.1175/1520-0477-56.5.527>.
- Oye, R. C., C. Mueller, and S. Smith, 1995: Software for radar translation, visualization, editing, and interpolation. *27th Conference on Radar Meteorology*, American Meteorological Society, pp. 359–361.
- Potvin, C. K., D. Betten, L. J. Wicker, K. L. Elmore, and M. I. Biggerstaff, 2012a: 3dvar versus traditional dual-doppler wind retrievals of a simulated supercell thunderstorm. *Monthly Weather Review*, **140** (11), 3487–3494, doi:10.1175/MWR-D-12-00063.1, URL <http://journals.ametsoc.org/doi/10.1175/MWR-D-12-00063.1>.
- Potvin, C. K., L. J. Wicker, and A. Shapiro, 2012b: Assessing errors in variational dual-doppler wind syntheses of supercell thunderstorms observed by storm-scale mobile radars. *Journal of Atmospheric and Oceanic Technology*, **29** (8), 1009–1025, doi:10.1175/JTECH-D-11-00177.1, URL https://journals.ametsoc.org/view/journals/atot/29/8/jtech-d-11-00177_1.xml?tab_body=pdf.
- Przybylinski, R. W., 1995: The bow echo: Observations, numerical simulations, and severe weather detection methods. *Weather and Forecasting*, **10** (2), 203–218, doi:10.1175/

1520-0434(1995)010<0203:TBEONS>2.0.CO;2, URL [http://journals.ametsoc.org/doi/10.1175/1520-0434\(1995\)010<0203:TBEONS>2.0.CO;2](http://journals.ametsoc.org/doi/10.1175/1520-0434(1995)010<0203:TBEONS>2.0.CO;2).

Rotunno, R., J. B. Klemp, and M. L. Weisman, 1988: A theory for strong, long-lived squall lines. *Journal of the Atmospheric Sciences*, **45** (3), 463–485, doi:10.1175/1520-0469(1988)045<0463:ATFSSL>2.0.CO;2, URL [http://journals.ametsoc.org/doi/10.1175/1520-0469\(1988\)045<0463:ATFSSL>2.0.CO;2](http://journals.ametsoc.org/doi/10.1175/1520-0469(1988)045<0463:ATFSSL>2.0.CO;2).

Schaumann, J. S., and R. W. Przybylinski, 2012: Operational application of 0-3 km bulk shear vectors in assessing quasi linear convective system mesovortex and tornado potential. American Meteorological Society, Vol. 142, URL <https://ams.confex.com/ams/26SLS/webprogram/Paper212008.html>.

Schenkman, A. D., M. Xue, and A. Shapiro, 2012: Tornadogenesis in a simulated mesovortex within a mesoscale convective system. *Journal of the Atmospheric Sciences*, **69** (11), 3372–3390, doi:10.1175/JAS-D-12-038.1, URL <https://journals.ametsoc.org/doi/10.1175/JAS-D-12-038.1>.

Shapiro, A., C. K. Potvin, and J. Gao, 2009: Use of a vertical vorticity equation in variational dual-doppler wind analysis. *Journal of Atmospheric and Oceanic Technology*, **26** (10), 2089–2106, doi:10.1175/2009JTECHA1256.1, URL <http://journals.ametsoc.org/doi/10.1175/2009JTECHA1256.1>.

Sibson, R., 1981: *Interpreting Multivariate Data*, 21–36.

Skamarock, W. C., M. L. Weisman, and J. B. Klemp, 1994: Three-dimensional evolution of simulated long-lived squall lines. *Journal of the Atmospheric Sciences*, **51** (17), 2563–2584, doi:10.1175/1520-0469(1994)051<2563:TDEOSL>2.0.CO;2, URL https://journals.ametsoc.org/view/journals/atsc/51/17/1520-0469_1994_051_2563_tdeosl_2_0_co_2.xml?tab_body=pdf.

Smull, B. F., and R. A. Houze, 1985: A midlatitude squall line with a trailing region of stratiform rain: Radar and satellite observations. *Monthly Weather Review*, **113** (1), 117–133, doi:[https://doi.org/10.1175/1520-0493\(1985\)113\(0117:AMSLWA\)2.0.CO;2](https://doi.org/10.1175/1520-0493(1985)113(0117:AMSLWA)2.0.CO;2), URL https://journals.ametsoc.org/view/journals/mwre/113/1/1520-0493_1985_113_0117_amslwa_2_0_co_2.xml?tab_body=pdf.

Smull, B. F., and R. A. Houze, 1987: Rear inflow in squall lines with trailing stratiform precipitation. *Monthly Weather Review*, **115**, 2869–2889, URL https://atmos.washington.edu/~beth/MG/PDFs/MWR87_smul_rear.pdf.

Storm Prediction Center, 2018: Surface and upper air maps. Tech. rep., National Weather Service Storm Prediction Center. URL <https://www.spc.noaa.gov/cgi-bin/spc/getuadata.pl?MyDate1=180413&Time1=12&MyDate2=180414&Time2=00&align=V&Levels=All>.

Trapp, R. J., S. A. Tessendorf, E. S. Godfrey, and H. E. Brooks, 2005: Tornadoes from squall lines and bow echoes. part i: Climatological distribution. *Weather and Forecasting*, **20** (1), 23–34, doi:10.1175/WAF-835.1, URL <https://journals.ametsoc.org/doi/10.1175/WAF-835.1>.

Trapp, R. J., and M. L. Weisman, 2003: Low-level mesovortices within squall lines and bow echoes. part II: Their genesis and implications. *Monthly Weather Review*, **131** (11), 2804–2823, doi:10.1175/1520-0493(2003)131(2804:LMWSLA)2.0.CO;2, URL [http://journals.ametsoc.org/doi/10.1175/1520-0493\(2003\)131\(2804:LMWSLA\)2.0.CO;2](http://journals.ametsoc.org/doi/10.1175/1520-0493(2003)131(2804:LMWSLA)2.0.CO;2).

Wakimoto, R. M., 1983: The west bend, wisconsin storm of 4 april 1981:a problem in operational meteorology. *Journal of Climate and Applied Meteorology*, **22** (1), 181–189, doi:10.1175/1520-0450(1983)022(0181:TWBWSO)2.0.CO;2, URL [http://journals.ametsoc.org/doi/10.1175/1520-0450\(1983\)022\(0181:TWBWSO\)2.0.CO;2](http://journals.ametsoc.org/doi/10.1175/1520-0450(1983)022(0181:TWBWSO)2.0.CO;2).

- Wakimoto, R. M., and V. N. Bringi, 1988: Dual-polarization observations of microbursts associated with intense convection: The 20 July storm during the mist project. *Monthly Weather Review*, **116** (8), 1521–1539, doi:10.1175/1520-0493(1988)116<1521:DPOOMA>2.0.CO;2, URL https://journals.ametsoc.org/view/journals/mwre/116/8/1520-0493_1988_116_1521_dpooma_2_0_co_2.xml?tab_body=pdf.
- Wakimoto, R. M., H. V. Murphey, A. Nester, D. P. Jorgensen, and N. T. Atkins, 2006: High winds generated by bow echoes. part i: Overview of the omaha bow echo 5 July 2003 storm during bamex. *Monthly Weather Review*, **134** (10), 2793–2812, doi:10.1175/MWR3215.1, URL <https://journals.ametsoc.org/view/journals/mwre/134/10/mwr3215.1.xml#i1520-0493-134-10-2793-Wakimoto4>.
- Wakimoto, R. M., P. Stauffer, and W.-C. Lee, 2015: The vertical vorticity structure within a squall line observed during bamex: banded vorticity features and the evolution of a bowing segment. *Monthly Weather Review*, **143**, 341–362, doi:10.1175/MWR-D-14-00246.1.
- Weisman, M. L., 1992: The role of convectively generated rear-inflow jets in the evolution of long-lived mesoconvective systems. *Journal of the Atmospheric Sciences*, **49** (19), 1826–1847, doi:10.1175/1520-0469(1992)049<1826:TROCGR>2.0.CO;2, URL [http://journals.ametsoc.org/doi/10.1175/1520-0469\(1992\)049<1826:TROCGR>2.0.CO;2](http://journals.ametsoc.org/doi/10.1175/1520-0469(1992)049<1826:TROCGR>2.0.CO;2).
- Weisman, M. L., and C. A. Davis, 1998: Mechanisms for the generation of mesoscale vortices within quasi-linear convective systems. *Journal of the Atmospheric Sciences*, **55** (16), 2603–2622, doi:10.1175/1520-0469(1998)055<2603:MFTGOM>2.0.CO;2, URL [http://journals.ametsoc.org/doi/10.1175/1520-0469\(1998\)055<2603:MFTGOM>2.0.CO;2](http://journals.ametsoc.org/doi/10.1175/1520-0469(1998)055<2603:MFTGOM>2.0.CO;2).
- Xu, X., M. Xue, and Y. Wang, 2015: The genesis of mesovortices within a real-data simulation of a bow echo system. *Journal of the Atmospheric Sciences*, **72** (5),

1963–1986, doi:10.1175/JAS-D-14-0209.1, URL <https://journals.ametsoc.org/doi/10.1175/JAS-D-14-0209.1>.